FORSCHUNGSZENTRUM JÜLICH GmbH

Institut für Festkörperforschung

Dimensional changes of ceramic materials under proton irradiation

Zhiyong Zhu

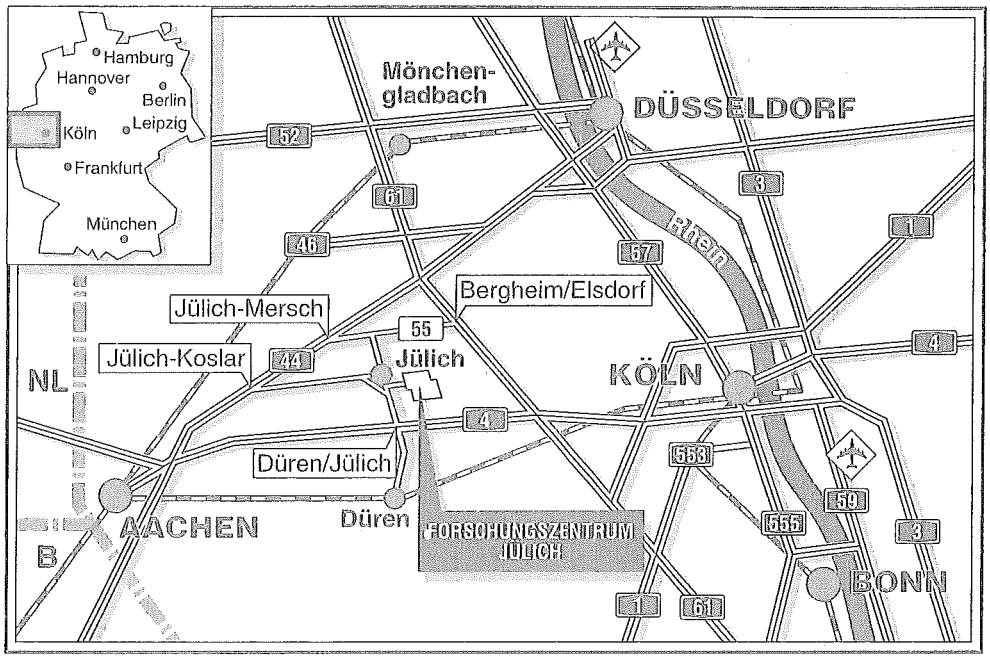

Berichte des Forschungszentrums Jülich ; 3109
ISSN 0944-2952
Institut für Festkörperforschung Jül-3109
D 82 (Diss. RWTH Aachen)

Zu beziehen durch: Forschungszentrum Jülich GmbH · Zentralbibliothek
D-52425 Jülich · Bundesrepublik Deutschland
Telefon: 02461/61-6102 · Telefax: 02461/61-6103 · Telex: 833556-70 kfa d

Dimensional changes of ceramic materials under proton irradiation

Zhiyong Zhu

Abstract

Ceramic materials including Al_2O_3, SiC, AlN, Si_3N_4, MgO, $MgAl_2O_4$, Si and SiO_2 as well as the refractory metal tungsten are irradiated with protons in the 10 MeV energy range at temperatures from 75°C to 630°C under uniaxial tensile stresses from 6 to 330 MPa to dose levels up to about 0.1 dpa. Changes in length and electrical resistivity are monitored after each irradiation or during beam-off periods. TEM and optical absorption technique are applied to extract information on the radiation induced microstructural changes. For materials with crystalline structure a modified rate theory is used to discuss the measurements whereas for SiO_2 glass a model is developed to describe the radiation induced deformation(compaction) and viscous flow. Alternatively a recently developed visco–elastic model based on thermal spike formation is also applied to explain the observed viscous flow in SiO_2 glass.

It is found that crystalline materials irradiated in the intermediate temperature range ($0.2T_m < T_{irr} < 0.4T_m$) deform in four different stages: (1) At very low doses mainly point defects or small defect clusters(loops) are formed, the strain increases linearly with dose. (2) After the nucleation of interstitial–type loops has finished and they become the dominating sinks, the strain follows a 2/3 power law dose dependence. (3) The growth and intersection of loops resulting in the formation of dislocation networks leads to a 1/2 dose dependence of the strain. (4) Finally, the strain saturates when the vacancy concentration becomes so high that spontaneous recombination dominates.

Thermal spike formation can account for at most 10% of the observed viscous flow of vitreous SiO_2 under 9.2 MeV proton irradiation. It is therefore proposed that energy deposition through electronic processes must also contribute to the viscous flow in glassy materials through processes of bond–breaking and re-bonding during irradiation. Formation of new bonds results in deformation while rearrangements of atoms with respect to the direction of an external stress during re-bonding causes viscous flow.

Furthermore, the present study demonstrates indirectly that the so–called RIED effect(radiation induced electrical degradation) in Al_2O_3 could be due to surface contamination which is enhanced by the applied electrical field.

Synopsis

Die keramischen Werkstoffe Al_2O_3, SiC, AlN, Si_3N_4, MgO, $MgAl_2O_4$, Silizium, SiO_2(im kristallinen und glasigem Zustand) und das hochschmelzende Metall Wolfram wurden mit Protonen im 10 MeV Energiebereich bei verschiedenen Temperaturen (75 bis 630°C) und Zugspannungen (6 bis 330 MPa) zu Dosen bis zu 0.1 dpa bestrahlt. Änderungen in der Länge und im elektrischen Widerstand der Proben wurden nach jeder Bestrahlung oder in Bestrahlungspausen gemessen. Änderungen der Mikrostruktur wurden durch TEM oder optische Absorptionsspektroskopie verfolgt.

Zur Beschreibung der Resultate in den kristallinen Materialien wurde eine modifizierte Ratentheorie verwendet. Zur Diskussion der gemessenen Verdichtung und des erhöhten viskosen Fließens von SiO_2 Glas wurden 2 Modelle herangezogen: Das erste basiert auf viscoelastische Vorgänge in thermischen Spikes, das zweite auf dem Aufbrechen und Rearrangement von atomaren Bindungen.

Die Messungen ergaben, daß im Tempuraturbereich zwischen 20 und 40% der Schmelztemperatur die bestrahlungsinduzierte Deformation in den kristallinen Materialien in 4 aufeinanderfolgenden Stufen erfolgt: (1) Zu Beginn der Bestrahlung wurden hauptsächlich einzelne Punktdefecte oder kleine Defectcluster erzeugt und die Dehnung nimmt linear mit der Dosis zu. (2) Nach Beendigung der Keimbildung von Versetzungsringen des Zwischengitteratom–Typs werden diese zu den dominierenden Defektsenken und die Dosisabhängigkeit der Dehnung folgt einem Potenzgesetzt mit dem Exponenten 2/3. (3) Wachstum und Durchdringung der Versetzungsringe führt zur Bildung von Versetzungsnetzwerken, was den Exponenten auf 1/2 reduziert. (4) Schließlich sättigt die Dehnung wenn die Leerstellenkonzentration so hoch geworden ist, daß alle neu erzeugten Defekte spontan rekombinieren.

In SiO_2 Glas kann das thermische Spike–Modell höchstens 10% der beobachteten viskosen Fließrate erklären. Es wird deshalb vorgeschlagen, daß hauptsächlich elektronische Energieverluste, die zum Aufbrechen von Atombindungen führen, für die beobachtete Verdichtung und die hohe Fließrate verantwortlich sind.

Schließlich konnte, sozusagen als Nebenprodukt der elektrischen Leitfähigkeitsmessungen, gezeigt werden, daß der derzeit kontrovers diskustierte RIED(radiation induced electrical degradation) Effekt in Al_2O_3 wahrscheinlich kein Volumeneffekt ist, sondern durch Leckströme in Oberflächenkontaminationsschichten vorgetäuscht wird.

Contents

Chapter 1

Introduction

Energetic particle irradiation of materials (e.g., in fission or fusion reactors, space vehicles, accelerator components, ion beam applications etc) causes significant changes in their microstructure [1] through the production of various defects by nuclear collisions and/or through electronic processes [2, 3]. This is the main reason for radiation induced changes of macroscopic properties such as mechanical properties [4], thermal and electrical properties and dimensional stability [5] which are among the most important technical considerations in use of structural and functional materials in a radiation environment. A comprehensive understanding of radiation damage effects is therefore essential.

Extensive studies have been conducted during the last decades including experimental measurements, theoretical modelling and computer simulation. In experimental studies charged particle irradiation [6] has often been used because of its flexibility in controlling irradiation conditions. Damage is monitored by direct microscopical observation through transmission electron microscopy(TEM) or by macroscopic measurements of properties like thermal conductivity, lattice parameter, optical absorption and material density which provide data for practical use as well as giving information in an indirect way about the radiation induced microstructural changes.

Refractory materials (ceramics and refractory metals) are proposed to be used in various radiation environments. In future fusion devices tungsten is proposed to be used as divertors and ceramic materials [7] are anticipated to serve both as structural components and as electrical insulators. Structural applications include first-wall armors and divertors, and electrical uses include, e.g. RF windows. The widespread use of microelectronics in space and military applications also require ceramic materials to serve as, for example, coverslips on solar cells, substrates for devices, dielectric and insulating layers, and optical communication media.

During production and/or operation ceramics are subject to both particle and electromagnetic radiation at temperatures up to half the melting temperature or more and to displacement doses up to 100 displacements per atoms(dpa). This situation requires a deep understanding of radiation damage in refractories which is actually quite limited compared to metals. A survey of literature shows that the knowledge of radiation induced dimensional stability of refractories, especially ceramics, is far from satisfactory and investigations of stress effects are completely missing.

In this work ceramic materials including Al_2O_3, SiC, Si_3N_4, AlN and MgO, $MgAl_2O_4$, Si, SiO_2 as well as polycrystalline tungsten are irradiated by protons under various temperatures and tensile stresses. During the irradiation the radiation induced dimensional changes and partially resistivity changes are measured. Complementary to the macroscopic measurements, TEM or optical absorption measurements are conducted to monitor the corresponding microstructural changes. In chapter 2 the earlier studies of radiation induced microstructural and dimensional changes are reviewed for both crystalline and glassy materials. Chapter 3 describes the details of the experimental measurements with the experimental results listed in chapter 4. Chapter 5 presents theoretical models for both crystalline and glassy materials to describe the radiation induced dimensional changes. They are used in chapter 6 to discuss the present measurements. Conclusions are given in chapter 7.

Chapter 2

Background of radiation damage studies in crystalline and glassy materials

It is well established that all macroscopically observed radiation effects are caused by one or more of the following elementary interactions between the radiation and the atoms of the solids: elastic collisions, electronic excitations and nuclear reactions [3](Fig.2.1). Nuclear

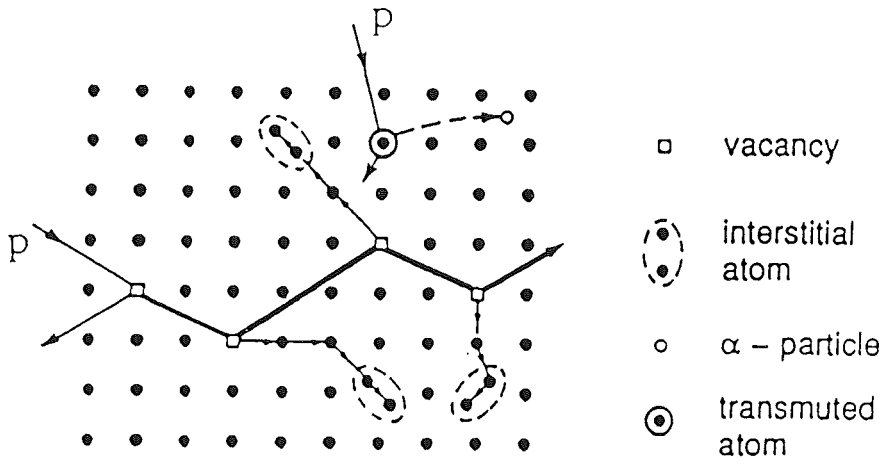

Figure 2.1: Schematic view of the interactions of high energy particles (P) with solid atoms, leading to vacancy–interstitial pairs (Frenkel defects) and to foreign atoms.

reactions which introduce foreign atoms inside the target material do not play a role under the irradiation conditions of this work and are thus not discussed further. For our case of bombardment with light ions in the 10 MeV energy range, the energy losses(and therefore the range of the particles) are dominated by electronic excitations and ionisations, as illustrated in Fig.2.2 which gives the stopping power due to electronic processes and elastic collisions, respectively, as a function of the proton energy. However, although being very high, the

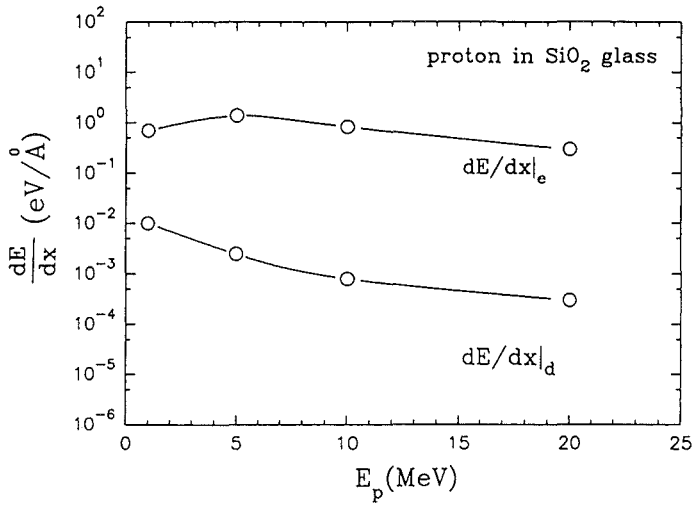

Figure 2.2: Electronic stopping power $dE/dx|_e$ and nuclear stopping power $dE/dx|_d$ as a function of particle energies E_p for protons in SiO_2 glass (calculated by using the TRIM–program [8]).

energy losses through electronic processes do not induce structural modifications in metals except where high local electronic excitation(coulomb explosion spike) occurs. The deposited energy is mainly transformed into heat. In insulators electronic processes can under certain circumstances indirectly transfer energy to a target atom and thereby induce displacement damage or lead to structural rearrangements, especially in glassy materials.

Through elastic collisions the bombarding particle transfers a recoil energy T to a target atom which leaves its original site if the recoil energy exceeds a material–dependent threshold, T_d. This recoil atom is called primary knock–on atom(PKA). The production of PKAs is characterized by the differential cross–section $d\sigma(T,E)/dT$, defined as the probability per unit irradiation dose and per energy interval, dT, that an irradiation particle of energy E transfers a recoil energy T to a target atom. The requirement of minimum energy for

producing displacement damage reveals the fact that a stable interstitial atom should be far enough from a vacancy to avoid spontaneous recombination. The volume of instability, called the spontaneous recombination volume v_s(Fig.2.3), is defined by all the lattice sites around an interstitial which, if occupied by a vacancy, would lead to an unstable Frenkel pair. Computer simulations suggest that for metals the recombination volume v_s is of the order of 100 atomic volumes(Ω). It is also found that the threshold energy for displacement depends on

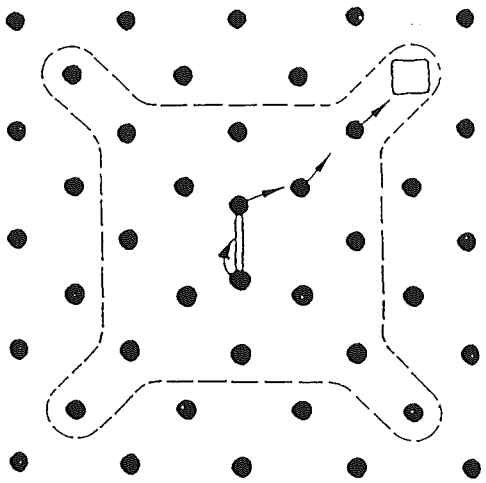

Figure 2.3: Static spontaneous recombination volume for Cu. The arrows indicate the recombination path of the instable Frenkel defect shown.

crystal orientation. T_d is generally smallest($= T_{d,min}$) around close packed lattice directions as in these directions replacement collision sequences are most efficient in separating the interstitial from its vacancy. Experimental determination of T_d in metals is usually carried out by monitoring the increase in electrical resistivity induced by the point defects. Another technique to measure the threshold energy is to observe the growth of preexisting interstitial clusters in situ in a TEM. In this case, the irradiation temperature must be high enough for the interstitial to be mobile. This technique is especially useful in multi-elements materials where displacement threshold energies for different interstitial species could be determined. In some materials like Al_2O_3, MgO single crystals, optical absorption technique is used to determine the displacement threshold energy.

If the recoil energy of a PKA is much high than T_d, the PKA can displace additional atoms during its slowing down in the solid. The result is a displacement cascade which is characterized by the number of defects $N_d(T)$ created in this cascade as well as the defect distribution. The number $N_d(T)$ of atoms which are displaced per primary knock–on event

is given by the so called NRT approximation named after Norgett, Robinson and Torrens [9]:

$$N_d(T) = \begin{cases} 0 & T_{dam} < T_d \\ 1 & T_d < T_{dam} < 2.5T_d \\ \frac{0.8T_{dam}}{2T_d} & T_{dam} > 2.5T_d \end{cases} \tag{2.1}$$

where T_{dam} is the energy contributing to defect productions. In metals $T_{dam} = T - Q$ with Q being the energy deposited in electronic processes.

Knowing $N_d(T)$ and the differential cross section $d\sigma(T, E)$, the total displacement rate K can be calculated as follows

$$K = \int_{E_{min}}^{E_{max}} \int_{T_d}^{T_{max}} N_d(T) \frac{d\sigma(T,E)}{dT} \frac{d\Phi(E)}{dE} dT dE = \sigma_d \cdot \phi \tag{2.2}$$

where $d\Phi(E)$ is the flux of irradiating particles with energies between E and $E + dE$, and E_{min} and E_{max} are the minium and maximum values, respectively, of the energy spectrum of the irradiation particles. T_{max} is the maximum transferable energy from the incident particle to the target atoms. For elastic collisions of nonrelativistic particles it is given by

$$T_{max} = \frac{4mM}{(m+M)^2} E \tag{2.3}$$

whereas for relativistic electrons it is

$$T_{max} = \frac{2m_e}{M} (\frac{E}{m_e c^2} + 2) E \tag{2.4}$$

with M and m the masses of the target atom and the bombarding particle, respectively, and m_e is the electron mass. The quantity σ_d is the so–called displacement cross section and ϕ is the total particle flux. K has a unit of dpa/second where dpa is a dose unit defined as displacement per atom.

In order to illustrate the differences in the primary defects structure produced by different particles, the quantity:

$$W(T') = \frac{1}{K} \int_{E_{min}}^{E_{max}} \int_{T_d}^{T'} N_d(T) \frac{d\sigma(T,E)}{dT} \frac{d\Phi(E)}{dE} dT dE \tag{2.5}$$

is introduced. It is the relative portion of displacements produced by recoils with energies below a given value T'. Fig.2.4 shows recoil spectra for SiO_2 irradiated by 3 MeV electrons and 9 MeV protons, respectively, calculated for three different displacement threshold energies by considering elastic collisions only. As can be seen, almost all the electron–irradiation induced recoils have energies below ~1 keV whereas by proton irradiation about 30% of the recoils have energies above 1 keV.

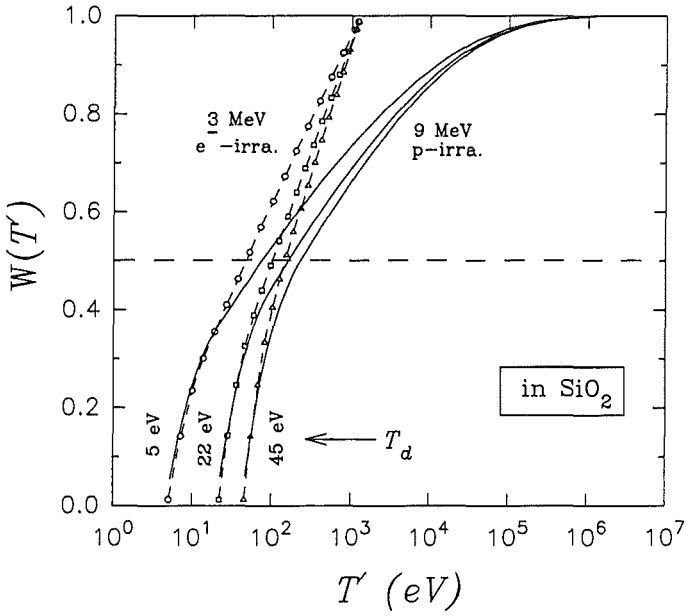

Figure 2.4: The function $W(T')$ calculated for SiO_2 for 3 MeV electrons and 9 MeV protons. The intersections between the horizontal line at $W(T') = 0.5$ and the curves determine the median recoil energy, $T_{1/2}$, which is the energy up to which half of the displacements are produced.

The displacement processes in the cascade terminate after about 10^{-13} seconds when the kinetic energy of all atoms in the cascade has fallen below T_d and no further displacements occur. The remaining energy is then dissipated into the surrounding lattice by focusons and later by phonons. This results in thermal spikes which could have temperatures several times higher than melting temperature(T_m). Computer simulations show that thermal spikes cool down in times of the order of 10 ps. During this time the core of the spike is a liquidlike droplet whereas at the periphery a shock–front builds up. The volume of thermal spikes V_{sp} is found to be linear in energy deposited in cascade collisions, i.e.

$$V_{sp} \approx \frac{T_{dam}}{14 k_B T_m} \tag{2.6}$$

where k_B is the Boltzmann constant and V_{sp} is in units of atomic volume. Very high energy PKAs induce subcascades with the subcascade number increasing with damage energy. The thermal spike period modifies greatly the final damage structures such as defect structures and distribution. This is not considered by the NRT approximation and therefore the final average number of Frenkel pair defects produced by a PKA of energy T is usually smaller than $N_d(T)$ given in eq.(2.1). This is accounted for by the damage efficiency ξ^0 which is

defined as the ratio of measured and evaluated defect numbers. As shown in Fig.2.5 the damage efficiency decreases with increasing median recoil energy. Furthermore, the final damage structures vary with irradiation temperature which modifies the damage structure through thermally activated processes like mutual annihilation of interstitials and vacancies, interstitial clustering at the spike periphery, etc.

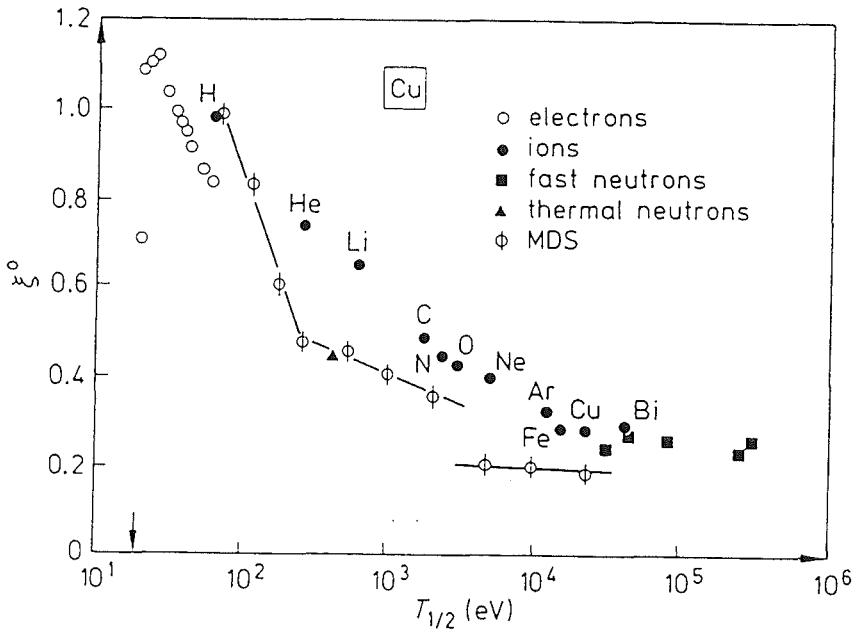

Figure 2.5: Damage efficiency ξ^0 as a function of the median energy $T_{1/2}$ in copper compiled by Averback et al. [10] and Kinney et al. [11]. Included are results from MDSs by Foreman et al. [12] and by Diaz de la Rubia and Guinan [13].

The changes of macroscopic properties of irradiated material are determined by the final damage structure. For example, the atoms around defects relax in the strain field around the defects and thus induce a volume change. The relative volume contribution of each defect species depends on the structure of the material and on the defect structure for which two examples are shown in Fig.2.6 and Fig.2.7. Similarly, the radiation defects cause extra scattering of conduction electrons and therefore a reduction in electrical conductivity which depends on defect concentration and structure.

As the damage mechanisms vary with materials, the radiation response of different materials can be largely different. In the following sections the radiation damage studies for crystals and glasses are reviewed seperately, with emphasis on radiation induced dimensional changes.

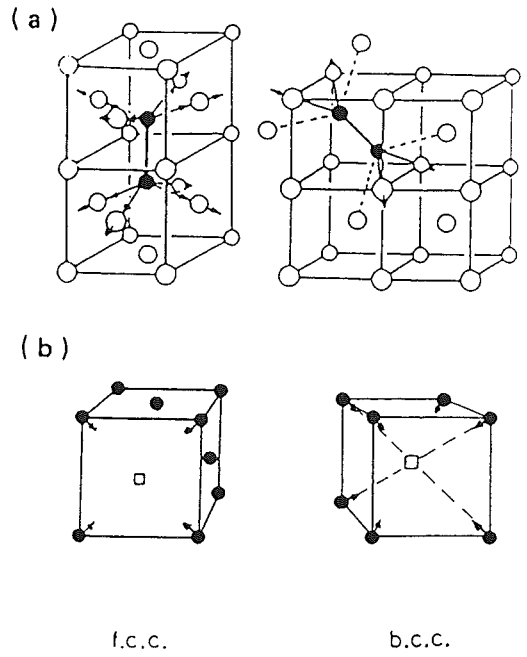

Figure 2.6: Schematic view of lattice distortions around single interstitials(a) and vacancies(b).

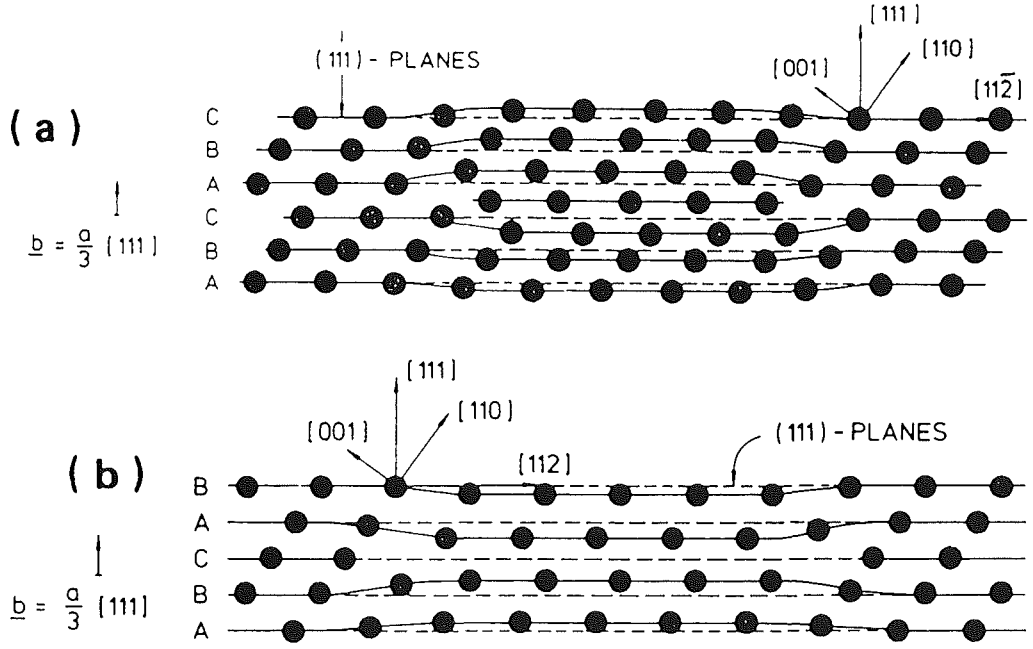

Figure 2.7: Atomic arrangement around dislocation loops formed by planar agglomeration of (a) interstitial atoms and (b) vacancies.

2.1 Crystalline materials

For radiation induced dimensional changes in crystalline materials three temperature ranges can be distinguished: (1) A low temperature range where the radiation–produced interstitials and vacancies are immobile, (2) An intermediate temperature range where only one defect type (normally interstitials) is mobile, (3) A high temperature range where both types of defects are mobile. Roughly speaking, for most metals low temperature means below 0.2 T_m and high temperature means above 0.4 T_m. Considering the materials and temperatures used in the earlier studies, very little is known about the dimensional stability of materials subjected to the intermediate temperature irradiation. The main reason for this is that the operation regimes for the most widespread structural materials(such as stainless steels) in modern fission reactors fall within the high temperature range. Recently low and intermediate temperature radiation studies attract more and more interest as it is proposed that ITER and future fusion reactors will use refractory metals as well as ceramic materials in places where the temperature is relatively low (e.g. ITER, shield: $\approx$150°C) [14]. On the other hand, it is well known that with special treatments strong vacancy trapping centres are formed in some materials and therefore the temperature increases at which the vacancies become mobile [15]. These kinds of materials could behave like being irradiated in the intermediate temperature range even if they are not high melting materials and the irradiation temperatures are not low.

As in the present study the materials used are mostly high-melting materials and the irradiations are carried out below ~600°C, the low and intermediate temperature radiation effects will be the main topic. In the following two sections experimental and theoretical studies of radiation induced microstructural and dimensional changes in the low and intermediate temperature ranges are reviewed.

2.1.1 Experimental aspects

2.1.1.1 Low temperature irradiation

Radiation damage in the low temperature range [16] is dominated by point defect accumulation. The changes in macroscopical properties are directly connected to the point defect concentration. It is found that the volume change calculated from the lattice parameter measurement equals that from the measurement of the macroscopic dimensions which implies that the produced defects are single point defects or small defect clusters. At high doses the radiation induced changes in macroscopical properties, like volume, resistivity etc, show

clear saturation behaviour. In some of the materials amorphization happens depending on irradiation particles and atomic bondings.

2.1.1.2 Intermediate temperature irradiation

The radiation induced microstructure in the intermediate temperature range shows the following common features [17–23]: At the beginning of the irradiation very small defect clusters ("black spot damage") are formed with a structure not resolvable in TEM. With increasing dose these clusters grow in size and become resolvable as interstitial loops which are located on special crystallographical planes. The continuous growth and intersection of loops result eventually in the formation of a dense dislocation network. Amorphization occurs in some of the materials at high doses. Quantitative measurements [24–26] show that for most materials the loop density saturates very quickly after the start of the irradiation while the loop size increases with dose with an exponent of 1/2 or 1/3.

Macroscopic studies [27, 28] show that the radiation induced deformation is linear in dose at very low doses and later on changes to a power law dependence with an exponent of 2/3. At low doses the macroscopic volume change equals that from lattice parameter measurements while at high doses the lattice parameter measurement gives a much lower value due to the formation of dislocation networks. With increasing temperature the radiation induced strain is reduced. Saturation in the radiation induced changes in properties like volume, thermal conductivity, electrical resistivity etc shows up in some of the materials.

2.1.1.3 Evidences of irradiation creep in the low and intermediate temperature range

Low and intermediate temperature irradiation creep has been known to occur for almost 40 years [5] and is classified as "low temperature irradiation creep". Here "low temperature" means that at the irradiation temperature no thermal creep occurs. A common feature of the "low temperature irradiation creep" is that the creep rate under irradiation shows, in contrast to thermal creep, a very weak temperature dependence(Fig.2.8). Recently Grossbeck and Mansur [30] (c.f. also the references therein) found that in n-irradiated austenitic and ferritic/martensitic alloys the creep rate at 60°C is even higher than that at 330 and 400°C (Fig.2.9).

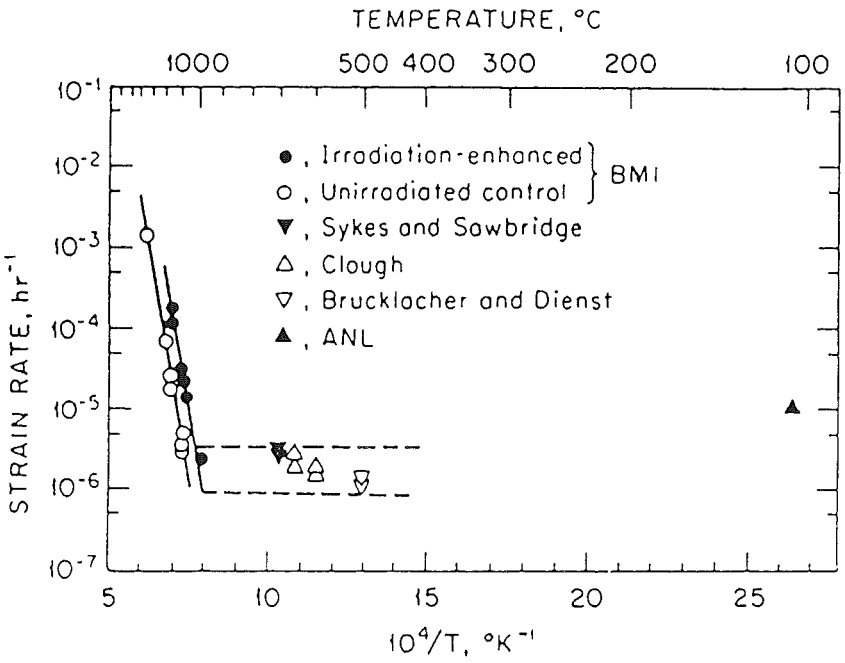

Figure 2.8: Irradiation creep in UO_2(from Ref. [29]). All data are normalized to a stress of ~24.2 MPa and a fission rate of 1.2×10^{19} fissions/m^3/s.

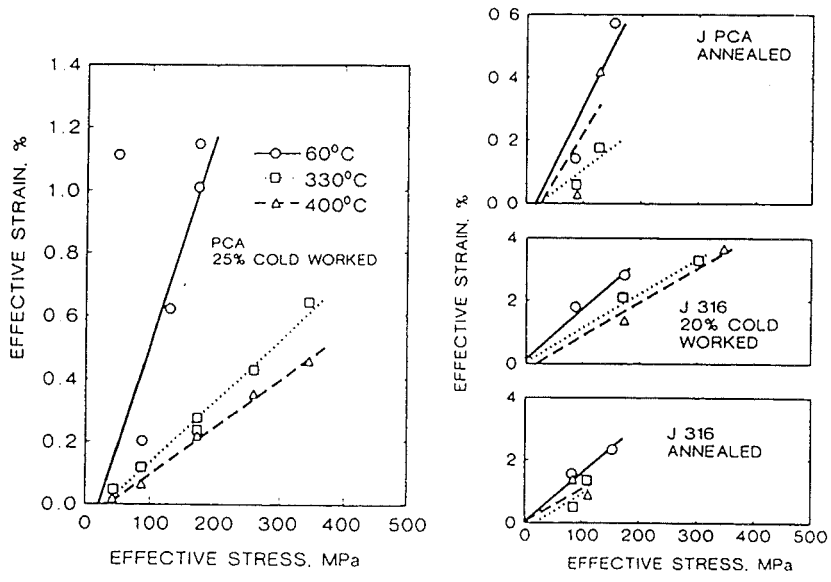

Figure 2.9: Total irradiation creep deformation of austenitic alloys under n-irradiation to a dose level of 8 dpa (from Ref. [30]).

2.1.2 Theoretical aspects

The radiation induced interstitials and vacancies can survive as single point defects or form clusters (loops, voids) or be absorbed by already exisiting sinks such as dislocations or grain boundaries. If the volume changes induced by a defect in different states are known and the material does not undergo phase changes or significant structural transformation during irradiation, the total amount of relative volume change S_t induced by the irradiation could be evaluated from the following equation:

$$S_t = C_i \cdot e_i + (C_v - C_{v0}) \cdot e_v + C_{iL} \cdot e_{iL} + C_{vL} \cdot e_{vL} + C_{iC} \cdot e_{iC} + C_{vC} \cdot e_{vC} + C_{iD} \cdot e_{iD} + C_{vD} \cdot e_{vD} \quad (2.7)$$

where C_{v0} is the thermal vacancy concentration. C_i, C_v are the concentrations of defects surviving as single interstitials(i) and vacancies(v), C_{iL}, C_{vL} are the concentrations of defects which form loops, C_{iC}, C_{vC} are the concentrations of defects which form three-dimensional clusters and C_{iD}, C_{vD} are the concentrations of defects absorbed by dislocations. The e_i, e_v, e_{iL}, e_{vL}, e_{iC}, e_{vC}, e_{iD}, e_{vD} are the relaxation volumes of the interstitials (i) and vacancies (v) in the corresponding states. Their approximate values are listed in Table 2.1 in units of atomic volume.

Table 2.1: Relaxation volume of defects in different states in units of atomic volume

Defect state	Interstitial	Vacancy
point defect	e_i=1.1∼2.0	e_v=−(0.1∼0.2)
at dislocation	e_{iD} ≈1.0	e_{vD} ≈−1.0
in large loops	e_{iL} ≈1.0	e_{vL} ≈−1.0
in clusters	e_{iC} <1.0	e_{vC} <1.0

2.1.2.1 Low temperature irradiation induced swelling

Irradiation with electrons and low energy light ions induces mainly single point defects(Fig.2.4), i.e. interstitials and vacancies, in equal number:

$$C = C_i = C_v - C_{v0} \quad (2.8)$$

At low temperature both the interstitials and vacancies are immobile and no clustering reactions occur. With $C_{v0} = 0$, eq.(2.7) then reduces to

$$S_t = C_i \cdot e_i + C_v \cdot e_v = V_F \cdot C_v \tag{2.9}$$

where

$$V_F = e_i + e_v \tag{2.10}$$

is the volume dilatation caused by one Frenkel pair. The defect concentration is at low temperature governed by spontaneous recombination and given by the following equation [31]:

$$\frac{dC}{dt} = K^*(1 - v_s C)^2 \simeq K(1 - v_s C)^2 \tag{2.11}$$

with v_s the spontaneous recombination volume (Fig.2.3) and t the irradiation time. $K^* = K\xi^0$ is the effective production rate of defects given by the displacement rate K (eq.2.2) times the efficiency factor ξ^0. Since for the present irradiation conditions $\xi^0 \approx 1$ (Fig.2.5), K^* is set equal to K in the following.

2.1.2.2 Intermediate temperature irradiation induced swelling

In the intermediate temperature range the radiation induced vacancies are immobile while interstitials can migrate to form loops or to be absorbed by dislocations. The swelling induced by irradiation is therefore given by

$$S_t = C_i \cdot e_i + (C_v - C_{v0}) \cdot e_v + C_{iL} \cdot e_{iL} + C_{iD} \cdot e_{iD} \tag{2.12}$$

Taking into account that initially the same amount of interstitials and vacancies are produced by the irradiation, i.e.,

$$C_v - C_{v0} = C_i + C_{iL} + C_{iD} \tag{2.13}$$

as well as the fact that $e_{iL} = e_{iD} \approx 1$ (see Table 2.1), eq.(2.12) becomes

$$S_t = C_i \cdot (e_i - 1) + (C_v - C_{v0}) \cdot (e_v + 1) \tag{2.14}$$

and since $C_i \ll C_v$,

$$S_t \approx V_F' \cdot (C_v - C_{v0}) \tag{2.15}$$

where

$$V_F' = e_v + 1 \tag{2.16}$$

is the volume dilatation caused by a single vacancy and an interstitial trapped in loops or in dislocations. The point defect concentrations can be calculated by applying rate theory.

Following are two attempts of calculation of point defect concentrations by using such an approach.

In 1970's Brimhall et al. [32] studied the radiation induced swelling observed in neutron irradiated Mo in the temperature range from 40–450°C by using the rate theory. The application of their model is limited due to the neglect of loop formation which is a common feature in the intermediate temperature range. Furthermore, the model does not predict the saturation in vacancy concentration which is clearly reflected by the length measurement in the temperature range where $D_v \approx 0$.

About 20 years later the rate theory was applied to deal with the neutron irradiated SiC ceramics by Borodin et al. [33]. This time the radiation induced loops were included and the rate equations were written as follows:

$$\frac{dC_v}{dt} = K - q(D_i + D_v)C_iC_v - Z_vD_v(C_v - C_{v0})(\rho_d + \rho_l) \tag{2.17}$$

$$\frac{dC_i}{dt} = K - q(D_i + D_v)C_iC_v - Z_iD_iC_i(\rho_d + \rho_l) \tag{2.18}$$

$$\frac{dR_L}{dt} = \frac{1}{b}[Z_iD_iC_i - Z_vD_v(C_v - C_{v0})] \tag{2.19}$$

where D_i, D_v are the diffusion coefficients of interstitial and vacancy, respectively, R_L is the loop radius, b the Burger's vector, Z_i and Z_v are the dislocation bias factors for interstitial and vacancy, respectively, ρ_d is the dislocation density, and C_L is the loop volume density. ρ_l is the loop line density which is given by

$$\rho_l = 2\pi R_L C_L, \tag{2.20}$$

and q is the recombination coefficient which is given by

$$q = \frac{q_0}{a^2} \tag{2.21}$$

with a the lattice parameter and q_0 a numerical factor($q_0 \approx 5$).

By assuming that the steady state concentration of free interstitials is quickly established due to the rapid diffusion of interstitials in the temperature range where $D_v \ll D_i$ and taking into account conservation of matter, i.e.,

$$C_i + b\rho_d R_L + \pi C_L b R_L^2 = C_v - C_{v0}, \tag{2.22}$$

they found the following analytical results:

- in sink dominating regime with dislocations as the dominating sinks, $R_L \propto (Kt)^{1/2}$ and $S_t \propto (Kt)^{1/2}$

- while in the regime where loops are the dominating sinks, $R_L \propto (Kt)^{1/3}$ and $S_t \propto (Kt)^{2/3}$.

Here S_t is taken as $(e_v + 1)(C_v - C_{v0})$ as the interstitial concentration C_i falls quickly far below C_v after a short time of irradiation (see eq.2.15). The saturation swelling (for C_{v0}=0) is given by

$$S_t^{\infty} = (1 + e_v)\sqrt{\frac{Z_i}{Z_v q a^2}}\sqrt{\frac{Kb^2}{D_v}}. \tag{2.23}$$

The model fits to the experimentally observed dose dependence of swelling and loop radius (see Section 2.1.1.2) in this temperature range. But the application of eq.2.23 to SiC ceramic shows that it can only be used in a very narrow temperature range, i.e. in the range where vacancy begin to move. Below this temperature range the theory fails since it predicts an infinite swelling for $D_v = 0$. Above this range the swelling is characterized by void formation which is not included in the model.

2.1.2.3 Creep studies in the low and intermediate temperature range

The experimental studies of the radiation creep in the low and intermediate temperature range are quite limited, but this did not hinder theoretical consideration. In a 1971 review given by Gilbert [34] it is shown that the following mechanisms could play a role during the intermediate temperature irradiation:

(a) Loop orientation
   - Radiation induced loops form preferentially on certain crystallographic planes under the influence of applied stress.

(b) Volume creep (stress-assisted swelling)
   - At low temperature vacancies are not mobile, but they cause swelling due to the dilations from single vacancies and small vacancy clusters. Applied stress increases the effective capture radius of a dislocation for interstitials and thereby reduces the number of interstitials that annihilate vacancies.

(c) Yielding creep
   - Radiation induced grain growth will cause internal stresses building up between grains. When this stress reaches the yield stress, the polycrystalline specimen gives way plastically to an externally applied stress.

(d) Dislocation glide
   - External stress guides the dislocation climb induced by absorption of diffusing point defects.

(e) Transient dislocation climb

- Dislocation segments bow out between pinned points through absorption of point defects until an equilibrium is reached between line tension, applied stress and chemical stress from the supersaturation of point defects.

About ten years later the large amount of models was classified into 3 groups [35–38] according to whether the creep is caused by stress induced preferential absorption of point defects (SIPA mechanism) or by preferred nucleation of point defect aggregates (SIPN mechanism) or by stress induced climb and glide (SICG mechanism). Accordingly the mechanisms (b), (d), (e) are included in the SIPA and mechanism (a) is in SIPN while mechanism (c) forms the basis of SICG.

Although great progress has been achieved in developing models for radiation induced creep, their applicability to experiments is still not satisfactory. This is e.g. shown by an American group who studied the radiation creep in the n-irradiated austenitic alloys [30]. They found that the SIPA as well as SICG mechanism cannot explain the high creep rate observed at low temperature for all the alloys. The problem is that in the two models the defect production is assumed to be in steady state. However, it can be shown that at low temperatures the steady state cannot be established in the time of the experiments. Therefore the time–dependent differential equations describing the defect production should be solved to give the defect concentration and this is then used in the creep models to calculate the creep induced by the corresponding irradiation.

2.2 Glassy materials

Glassy material is different from crystalline material in that it has no long range order. As shown in Fig.2.10, a single-phase crystalline material reaches its final crystal structure immediately after cooling down below melting temperature while glassy material shows a smooth transition from liquid state to glass state. The final microstructure of glassy material is quite open compared to that of the corresponding crystalline material with density varying with cooling rate. High cooling rate gives lower density. Due to the large difference in structure, the radiation responses of glassy and crystalline materials are quite different. In the following three sections the main radiation effects in oxide glasses observed earlier are summarized.

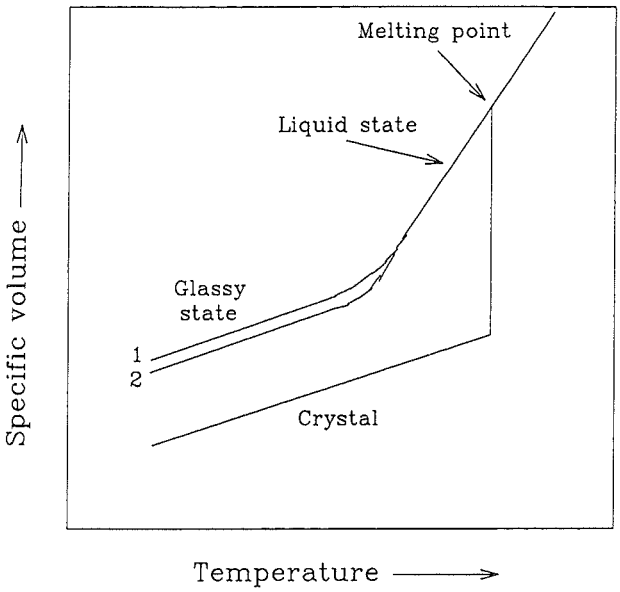

Figure 2.10: Specific volume of glass-forming and non-glass-forming materials as a function of temperature(schematic). The two curves for the glassy state indicate that the volume and other properties depend on the cooling rate (1—fast cooling, 2—slow cooling).

2.2.1 Radiation induced defects in oxide glasses

In comparison to crystalline materials, defects in glassy materials are more complex [39–42]. Techniques like ESR [43, 44], luminecence and optical absorption [39, 45] are used to identify the defects induced by irradiation. Fig.2.11 and Fig.2.12 show absorption spectra of vitreous SiO_2 irradiated at room temperature with 1 MeV electrons and 46.5 MeV Ni^{+6} ions, respectively. Table 2.2 gives a summary of the radiation induced optical absorption bands found in SiO_2 glass (most of which are from the compilations in Ref. [46] and [47]). The last column of the table shows the possible defect structure corresponding to the absorption band. As can be seen, the radiation induced defect character strongly depends upon the type of irradiation. The E centre is thought to be a peroxy radical in which an unpaired electron is connected to two unequivalent oxygens and to a single silicon. It is produced both by neutron and γ-ray irradiation, but the production rate under neutron irradiation is much higher than in the case of γ-irradiation. The D centre is found after heavy ion irradiation as well as X-ray irradiation and the corresponding defect microstructure is not yet clear. The band around 6.5 eV is reported by E. J. Friebele et al. [47] and M. Guzzi et al [48],

Table 2.2: Summary of radiation induced optical absorption bands in SiO_2 glass

Label	Peak energy(eV)	Occurrence	Defect
	8.2	γ-irra.	?
	8.0	γ-irra.	?
E	7.6-7.7	n-irra.	peroxy radical
		γ-irra.	
D	7.15-7.2	heavy ion-irra.	?
		X-ray irra.	
	6.5	e^--irra.	?
E_1'	5.78-5.85	n-irra.	one e^- trapped
		γ-irra.	in O vacancy
E_2'	5.5	e^--irra.	E_1'+proton
B_2	5.0-5.1	heavy ion-irra.	neutral O vacancy
		n-irra.	or peroxy radical
D_0	4.7-4.8	e^--irra.	?
		heavy ion-irra.	

but no interpretation is given by the authors. E_1' centre and E_2' centre are well identified defects in crystalline SiO_2 (c-SiO_2) with E_1' centre defined as an unpaired electron situated on a Si dangling orbital, pointing towards an oxygen vacancy. In irradiated amorphous SiO_2 (v-SiO_2) the two centres can not be separated from each other in ESR measurements. The band at 5.0 eV(B_2 centre) concerns a defect unidentified by ESR. It is practically unobservable under e^--irradiation, weak under proton irradiation and strong under heavy ion irradiation. It is therefore believed that the band originates from defects created by nuclear collisions, possibly a neutral oxygen vacancy which could serve as precursor of the E′ centre. The D_0 centre at 4.7–4.8 eV is not yet identified. It is produced by e^- as well as heavy ion irradiation. Especially in the case of electron irradiation where the B_2 centre is absent, the D_0 centre shows up clearly and forms a shoulder on the E′ peak(Fig.2.11).

Although the study of defects in SiO_2 has been conducted for almost 40 years, the detailed structures of various defects are still ambiguous. This situation greatly impeded the theoretical work to develop models for the radiation induced macroscopical changes, inspite of the large amount of observations reviewed in the next two sections.

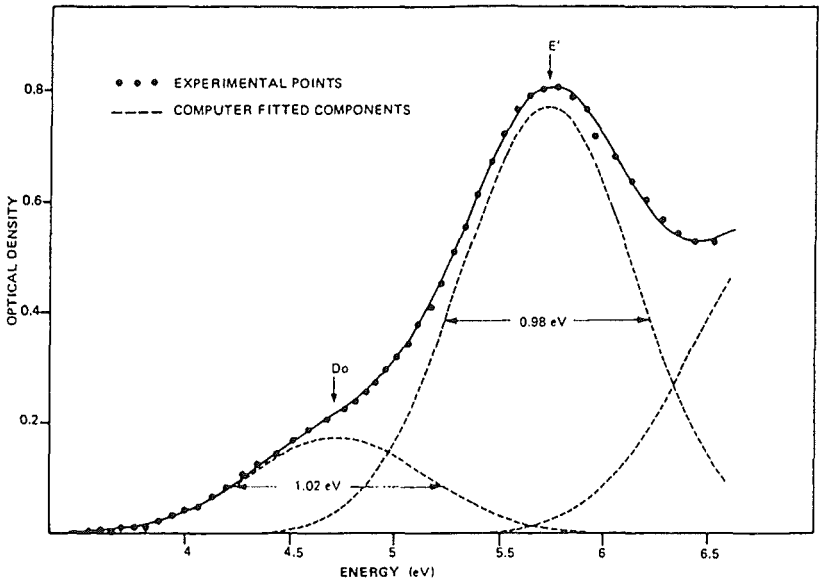

Figure 2.11: Absorption spectrum of v-SiO_2 after room temperature irradiation with 1 MeV electrons to $\sim 8 \times 10^{20} e^-/m^2$ (from Ref. [45]).

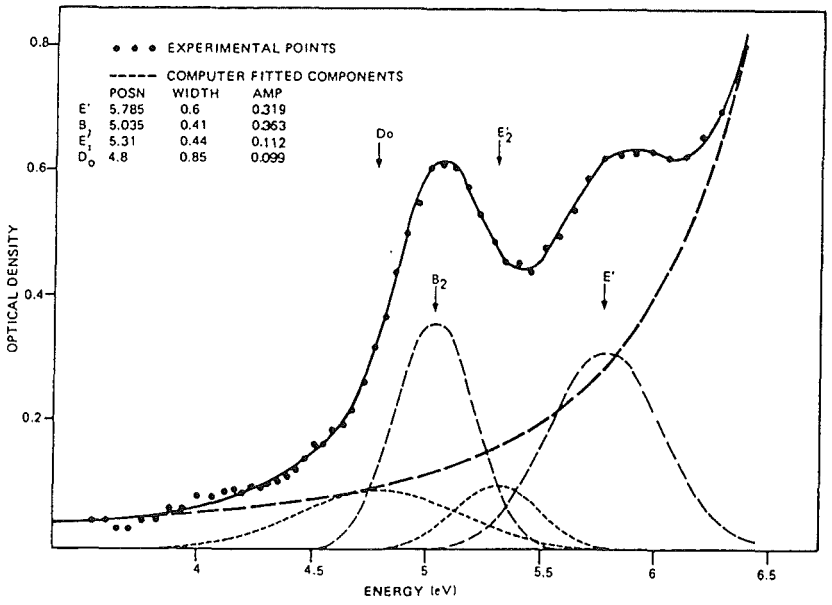

Figure 2.12: Absorption spectrum of v-SiO_2 after room temperature irradiation with 46.5 MeV Ni^{+6} ions to $\sim 10^{18} Ni^+/m^2$(from Ref. [45]).

2.2.2 Radiation induced deformation in oxide glasses

SiO_2 glass shows compaction under irradiation by different particles, including neutrons [48, 49], electrons [49, 50], ions [49–51] as well as γ-rays [50] and X-rays [49]. The compaction saturates around 3% reduction in volume with small if any variation with irradiation particles. No energy threshold has been observed for producing the compaction. Studies conducted on different silicas show that the compaction is rather insensitive to the impurity content [51] and has no temperature dependence at least below 100°C [50]. Annealing of heavily irradiated SiO_2-glass shows clear recovery of the radiation induced compaction around 500°C [52]. Although there is no difference in the radiation induced saturation density, the compaction before saturation shows different dose dependence for different particles [50]. By neutron, He^+ and D^+ irradiation the compaction is linear in dose while by e^-, H^+ and γ-ray irradiation the compaction depends on the 0.5-0.7 power of dose. This behaviour indicates that elastic collisions are more efficient in producing compaction as compared to ionization alone.

Contrary to the SiO_2 glass, the crystalline SiO_2 expands under n-irradiation with maximum volume changes going up to about 15% [53, 54]. The final state induced by high dose irradiation shows exactly the same properties(density, thermal expansion, elastic constant etc) as that found in heavily irradiated amorphous silica (see Fig.6.9).

Other glasses show complex behaviour under irradiation in that the radiation induced changes in density depend upon the glass composition. In some silicates and borosilicates irradiated with ions it is found that the materials show first expansion and then contract with further irradiation [55].

All the observations cited above are from irradiations conducted above room temperature. At low temperatures another type of deformation is induced by irradiation. It is found that vitreous silica shows transitory expansion by pulsed electron irradiation at low temperature [56]. On the other hand, swift heavy ion irradiation at low temperatures cause glassy material to expand in the direction perpendicular to the ion beam while contracting in the beam direction without volume change [57]. The requirement for producing the phenomenon is that the electronic stopping power of the irradiation is above about 2 keV/nm.

2.2.3 Radiation induced viscous flow in oxide glasses

Radiation induced plastic flow in glassy materials has been realized for more than 30 years. Qualitatively it has been observed in different glasses irradiated by neutrons [49], ions [51, 58, 59] and electrons [60] even with energies that could not induce damage through

elastic collisions. Probably the first quantitative study was conducted by G. Mayer and M. Leconte [62] who found in neutron irradiated fused silica that the viscosity under a flux of 2×10^{16} n/m^2/s at 60°C is the same as at 600°C without irradiation. The same phenomenon is observed in neutron irradiated aluminium-silicate glass [63]. In this case the viscosity induced by 1.3×10^{17} n/m^2/s irradiation at 60°C equals the thermal viscosity at 180°C below which the viscosity remains constant and depends only on the fast neutron flux. Systematical studies have been conducted on B_2O_3 glass by a French group [61, 64]. Reduction in viscosity is observed under heavy ion (Ar^+, 1.66GeV) irradiation as well as under electron irradiation over a wide range of energies (60keV to 2.5MeV). The lower electron energies are far below the threshold for producing atomic displacement by elastic collisions. At temperatures where thermal viscous flow is negligible, the radiation induced viscosity shows no temperature influence but is inversely proportional to flux. At high enough temperatures the viscous behaviour of the material under radiation is governed by the thermally activated process.

Chapter 3

Experimental Details

3.1 Material characterization and specimen preparation

The materials used in this study can be divided into four groups. The first group are ceramic (that means: polycrystalline) materials which include Al_2O_3, AlN, SiC(high density, denominated as SiC-HD), SiC-30%C(a composite containing 30%C in SiC matrix, denominated as SiC/C) and Si_3N_4. Single crystalline Al_2O_3, MgO, Si and SiO_2 as well as polycrystalline $MgAl_2O_4$ form the second group. The third group contains vitreous SiO_2 and the fourth group metallic polycrystalline tungsten. The materials of group I to III are plates of thicknesses varying from 250 μm to 350 μm while tungsten is in the form of 50 μm thick foils with a purity of about 99.95%. SEM and X-ray diffraction technique are used to determine grain size or crystal orientation of the materials, respectively. In Table 3.1 the measured material parameters are listed together with that provided by the producer (For further information cf. Ref. [65]). Fig.3.1 to Fig.3.6 show the material morphologies taken by SEM. It can be seen that the grain size of Al_2O_3 ceramics is doubled by 3 hrs. heating at 1680°C (Fig.3.1 and 3.2).

Table 3.1: Material parameters

Materials	density $[g/cm^3]$	specimen thickness $[\mu m]$	grain size $[\mu m]$	Weibull modulus	thermal conductivity $[Wm^{-1}K^{-1}]$	thermal shock resistance $[kWm^{-1}]$
c – Al_2O_3[1]	3.9	240	1.6	2.5	~ 31	$2.2 - 3.7$
SiC – HD	3.2	$330 - 360$	~ 2	~ 5	$30 - 200$	~ 20
SiC/C	2.647	315	$10 - 50$	~ 5	$30 - 200$	~ 15
Si_3N_4	3.204	365	~ 0.5	?	$30 - 40$	$11 - 17$
AlN	3.262	270	2.5	?	$140 - 170$	~ 20
s – Al_2O_3	3.96	250	–	?	~ 42	~ 4.9
MgO	3.676	260	–	?	$25 - 50$	$0.9 - 1.4$
$MgAl_2O_4$	3.608	277		6.5	~ 16	~ 1.7
Si	2.375	$280 - 330$	–	2.7	~ 130	~ 16.5
s – SiO_2	2.649	300	–	?	~ 10	~ 0.6
v – SiO_2	2.27	$270 - 320$	–	2.1	1.3	2.16
W	19.3	50		?	163	71

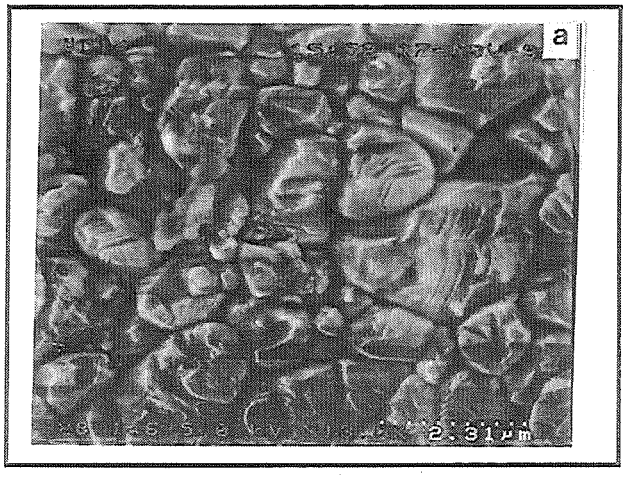

Figure 3.1: Morphology of Al_2O_3 ceramic(as received).

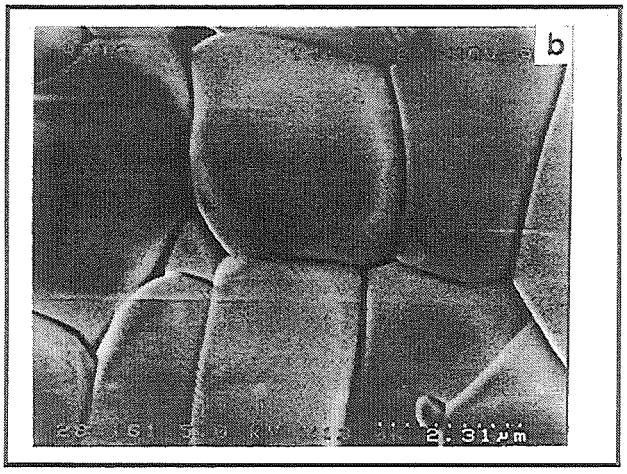

Figure 3.2: Morphology of Al_2O_3 ceramic (after 3 hrs. heating at 1680°C).

[1]c— ceramics, s— single crystalline, v— vitreous

Figure 3.3: Morphology of SiC-HD ceramic.

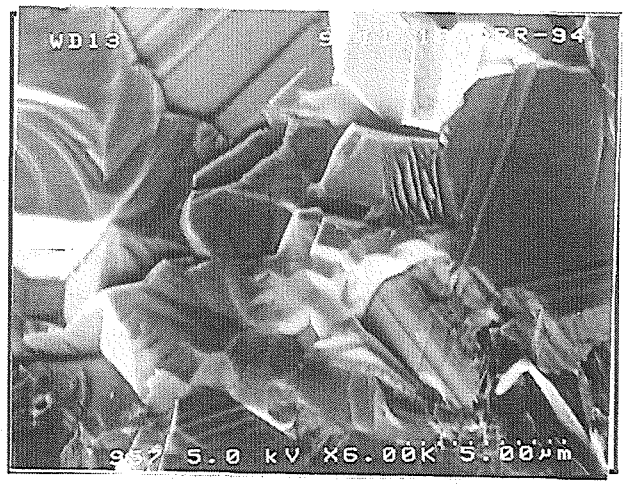

Figure 3.4: Morphology of SiC/C composite.

Figure 3.5: Morphology of AlN ceramic.

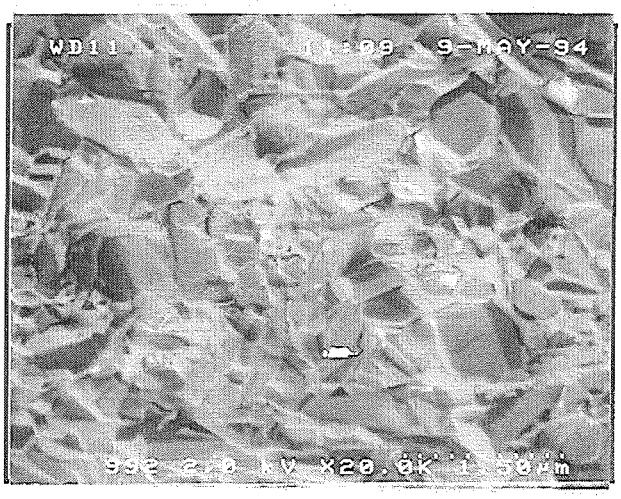

Figure 3.6: Morphology of Si_3N_4 ceramic.

Ultrasonic technique is used to cut the materials of the first three groups into dog-bone shape. As shown in Fig.3.7 three shapes with different dimensions are used in order to increase the maximum applicable tensile stress. The 3 mm diameter holes at the end pieces of the specimen are used to suspend the specimen and to apply a tensile stress with pins that tightly fit into the holes. The width at the gage section is in most cases around 3 mm and the irradiated length (hatched area) is fixed at 7 mm. Tungsten is cut by electrical spark erosion technique to the form shown in Fig.3.8 which can also be used for measurement of electrical resistivity. Tensile stress is applied by clamping the tungsten specimen at the end pieces. The irradiated area is centered in the middle of the gage section with the irradiated length fixed at 7 mm. The width of the gage section is chosen to be 2 mm or 3 mm according to the requirement. As the specimen temperature under irradiation is monitored by an infrared-

pyrometer which requires the specimen to be opague to the working light of the pyrometer as well as to have a surface of known emissivity, the specimen surfaces (except tungsten) are covered by sputtering 1.5μm platinum films onto the gage section. For some materials like SiO_2 glass, MgO etc, the specimen surfaces are first sputtered with 0.1μm titanium and then platinum. This process greatly improved the adhesion of the sputtered film to the specimen surface. The sputtered metal film is also used as electrodes to apply an electrical field across the specimen thickness and to measure the electrical resistivity(see section 3.5 and Appendix).

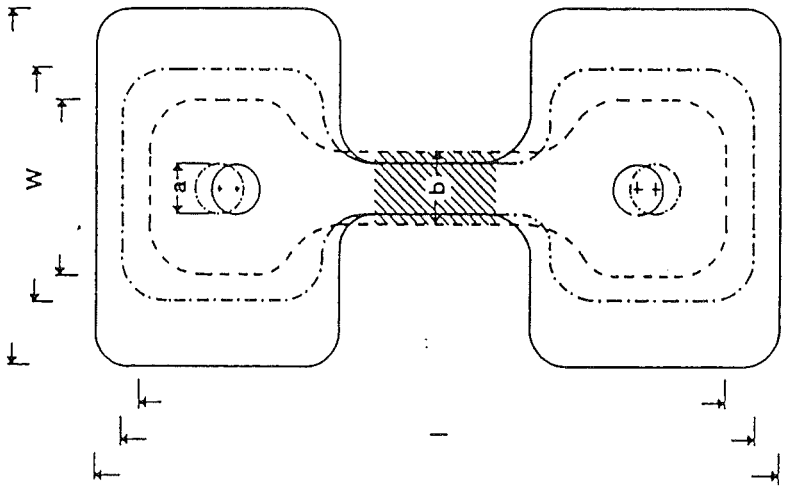

Figure 3.7: Geometry of ceramic specimens. The width of the grip regions(w), width of the gauge section(b) and length(l) for three different cutting are 10/4/32, 13/3/36 and 20/3/38 mm, respectively.

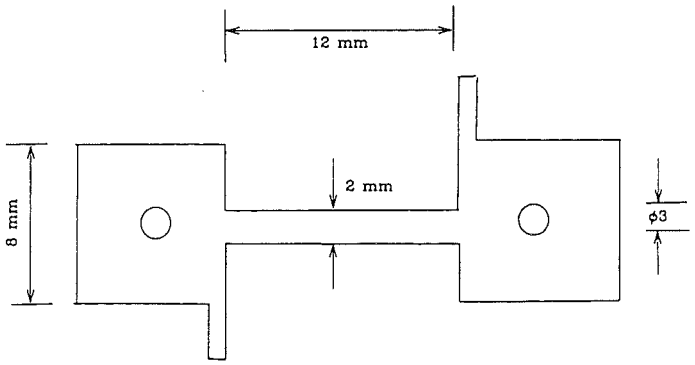

Figure 3.8: Geometry of tungsten specimens.

3.2 Specimen irradiation and length measurement

Specimens are irradiated by protons provided by the Jülich compact cyclotron in an apparatus [66] which is modified for the ceramic specimens. Table 3.2 gives a summary of the irradiation parameters. In order to have an homogeneous damage distribution across the specimen thickness, the energy of the proton beams is chosen according to materials to limit the energy loss inside the specimen to be less than 30% of the incident energy. As shown in Fig.3.9 the focussed proton beam from the cyclotron is scanned horizontally and vertically so that the irradiation across the specimen surface is homogeneous.

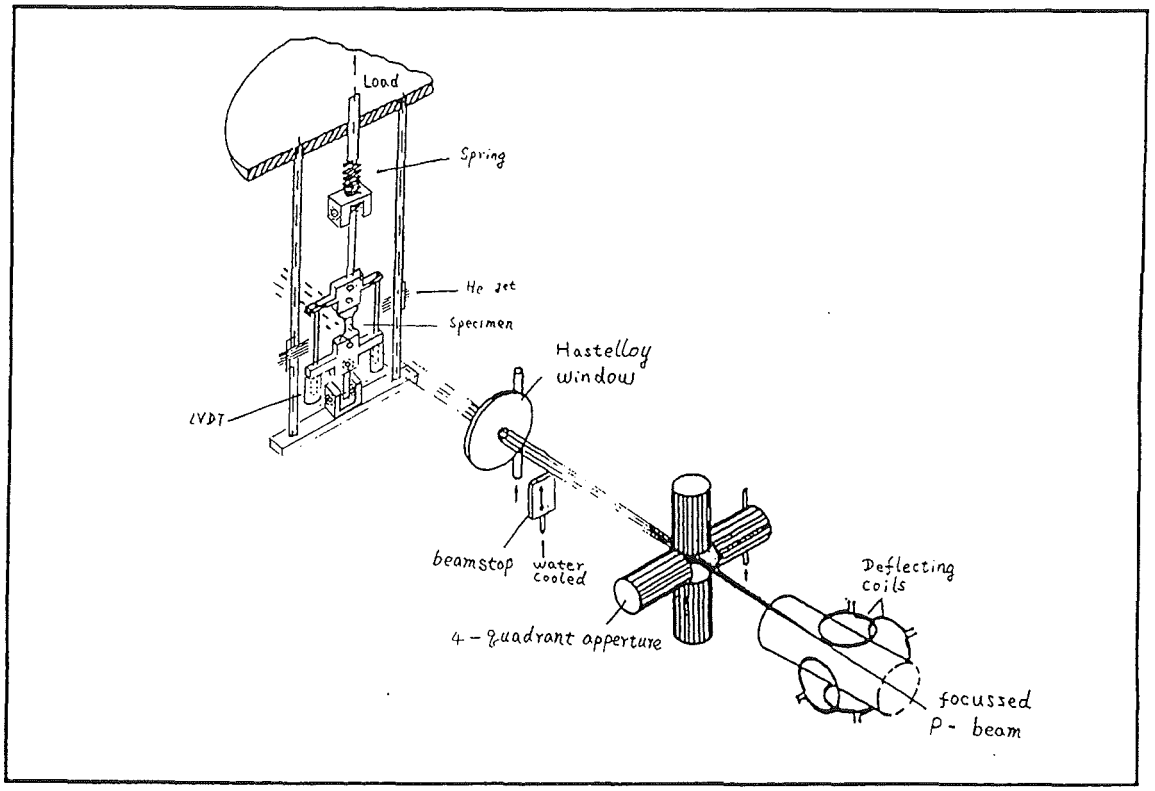

Figure 3.9: Schematic view of the specimen irradiation and length measurement system.

A 25μm Hastelloy window is used to separate the specimen chamber from the vacuum system of the cyclotron. Helium gas, which is cooled and purified outside the specimen chamber by passing through a liquid nitrogen bath as well as a temperature-adjustable water bath (see Fig.3.10), is directed to the specimen surface through five jets arranged along the specimen length on each side of the specimen. By controlling the He fluence of each He-jet in accordance with the proton flux, the specimen temperature as well as the

Table 3.2: Irradiation parameters

Materials	E_p $[MeV]$	T_{irr} $[°C]$	σ $[MPa]$	irradiation surface and tensile direction	dose exponent of strain/ resistivity	dose range for the exponent(in dpa)
$c-Al_2O_3$	10.7	235	$20-40$	–	0.56	$2\times10^{-3}-10^{-2}$
		445	$20-100$	–	0.46	$2\times10^{-3}-10^{-2}$
		630	40	–	–	–
SiC – HD	10.7	265	30	–	0.78	<0.011
		505	30	–	0.69	$0.0047-0.015$
		475	100	–	–	–
SiC/C	10.7	235	30	–	0.86	<0.011
Si_3N_4	10.7	230	40	–	0.6	$10^{-3}-2\times10^{-2}$
AlN	10.7	230	40	–	0.68	$10^{-3}-10^{-2}$
		420	40	–	0.73	$10^{-3}-6\times10^{-3}$
$s-Al_2O_3$	10.7	225	40	$(11\bar{2}0)<0001>$	0.93	$<7\times10^{-3}$
		225	40		0.73	>0.01
MgO	10.7	220	20	$(100)<110>$	0.69	$4\times10^{-4}-6\times10^{-3}$
		220	40		0.78	$5\times10^{-4}-6\times10^{-3}$
		220	60		0.66	$4\times10^{-4}-1\times10^{-3}$
$MgAl_2O_4$	10.7	225	40	–	0.6	$10^{-3}-2\times10^{-3}$
Si	9.2	295	51.7	$(111)<211>$	–	–
		565	17.2		–	–
		565	43		–	–
$s-SiO_2$	9.2	75	11	36° from c – axis	0.63	<0.007
		220	$11-40$		0.5	<0.016
$v-SiO_2$	9.2	220	$6-30$	–	–	–
		400	$6-29$	–	–	–
		600	$11,20$	–	–	–
W	9.2	160	$170,330$	–	0.48	$2\times10^{-3}-0.04$
		320	$110,170,250,320$	–	0.49	$3\times10^{-3}-0.04$
		520	330	–	–	–

temperature distribution along the specimen length can be adjusted. The specimen holder is designed in the way that the specimen aligns itself during stressing so that the bending stress suffered by the specimen is minimized. The tensile stress is determined by the length measurement of a spring of known spring constant. The particle flux is simply taken as the proton current going through an aperture divided by the aperture area. This introduces an uncertainty of up to about 20%.

The specimen length is monitored by two linear variable displacement transducers(LVDTs) located at the sides of the specimen. By measuring the specimen length before and after irradiation at room temperature as well as during beam-off period, the length change induced by each irradiation can be evaluated. Length measurement during irradiation is in most cases useless due to the large fluctuation in beam flux except where great

changes in length could be induced by short time irradiation, like for SiO_2 glass. The data acquisition in the present study is conducted automatically through a computer controlled system(Fig.3.11). The precision in the length measurement made at room temperature is better than 10^{-5}.

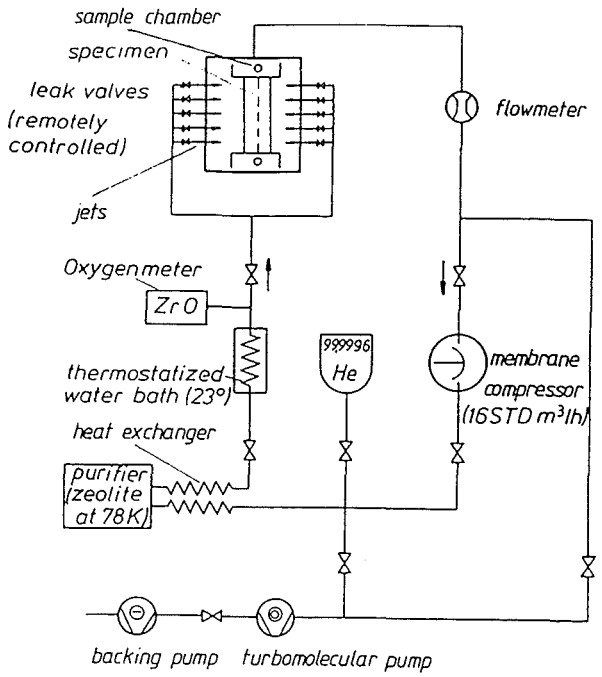

Figure 3.10: Schematic view of the specimen cooling system.

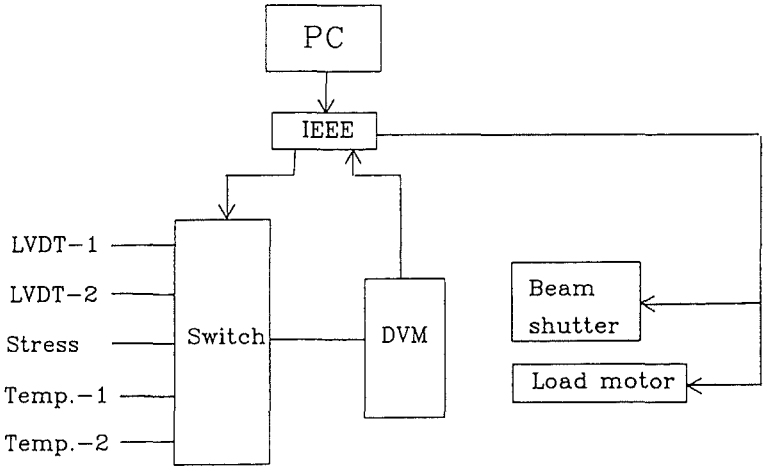

Figure 3.11: Data acquisition system.

3.3 TEM observation

Different procedures depending on the material are used in preparing TEM specimens. Al_2O_3 and SiC ceramics as well as crystalline MgO, $MgAl_2O_4$ and Si are cut into 3 mm diameter discs by using an ultrasonical technique. They are then thinned mechanically to a thickness of about 150 μm and then dimpled and ion-thinned into the final form. Polycrystalline tungsten specimens are cut into 3 mm diameter discs by punching. They are then thinned electrochemically by a double jet thinning system called "TENUPOL". The chemical solution used is 2% NaOH. During thinning the electric current is about 400mA which gives a voltage drop of about 12-15V. The working temperature is controlled to be around 10°C. TEM observation is conducted through a Philips TEM430 system with the electron energy adjusted at 300 keV. Specimen thickness which is needed in the calculation of defect density, is measured by contamination of both surfaces of the specimen and measuring the distance by tilting. The precision of the thickness measurement is around $\pm 10\%$.

3.4 Optical absorption measurement

A commercial optical spectrometer(SD 90 system, Jobin Yvon, Instruments S. A.) is used to study the radiation induced optical absorption in SiO_2 glass in the ultraviolet(UV) range. As shown schematically in Fig. 3.12 the spectrometer is mainly composed of a light source, a monochromator, a detector and a control system. The main specifications of the system

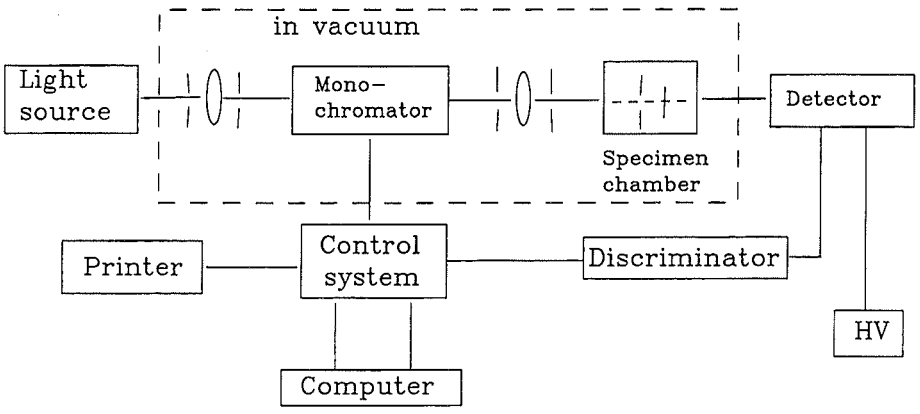

Figure 3.12: Schematic view of optical absorption spectrometer.

are listed as follows:

- light source—— water cooled 200W deuterium lamp of L 1835 type, Hamamatsu company, with a MgF_2 window. Wavelength ranges from 115 nm to 400 nm.
- monochromator—— toroidal holographic grating monochromator of LHT 30 type, Jobin Yvon, Instruments S. A., with a resolution of 0.4 nm at a slit width of 0.2 mm. Grating material is $CrAlMgF_2$.
- detector—— photocounting multiplier of type R943-02 from Instruments S. A. Company, together with Peltier–cooling chamber and sodium salicylate–converter for transformation of UV–photon into visible light for the multiplier.

During measurement the specimen is held inside a light-sealed chamber which is kept at low vacuum ($\sim 10^{-3}$mbar). An area of about 2 mm in diameter around the specimen centre is subject to the UV-light which is controlled to change wavelength from 150 nm to 300 nm with the light staying at each wavelength for 10 seconds. The UV-light penetrates perpendicularly across the specimen thickness and is received by the detector. This gives the transmitted spectrum ($I_t(\lambda)$) which is related to the absorption coefficient (α) of the material through the Lambert-Beer law:

$$I_t(\lambda) = I_0(\lambda)e^{-\alpha x} \tag{3.1}$$

where $I_0(\lambda)$ is the light intensity before absorption and x is the specimen thickness. By measuring the transmitted spectrum of the irradiated specimen ($I_s(\lambda)$) as well as that of the reference specimen (unirradiated, $I_b(\lambda)$), the radiation induced absorption coefficient $\alpha_{irr}(\lambda)$ can be evaluated as follows:

$$\alpha_{irr}(\lambda) = \frac{1}{x_s} ln \frac{I_0(\lambda)}{I_s(\lambda)} - \frac{1}{x_b} ln \frac{I_0(\lambda)}{I_b(\lambda)} \tag{3.2}$$

where x_s and x_b are the thicknesses of the irradiated and unirradiated specimens, respectively. The spectrum of $\alpha_{irr}(\lambda)$ as a function of light energy $E(E = hc/\lambda$, c–light velocity) is then fitted with a sum of several Gaussian distributions to give information about the absorption centres inside the specimen. The total number of fitting peaks could go up to seven, four of which could be fixed in absorption energy. By the way, it is found that fitting with Lorenz distributions gives less agreements. To study the annealing behaviour of the radiation induced optical absorption, the irradiated specimens are isochronally annealed at temperatures from 100°C to 800°C with the annealing time kept at 30 min. A reference

specimen is annealed in the same way to monitor any extra changes induced by the treatment. After each time of annealing the transmitting spectrum is measured and evaluated as described above.

3.5 Electrical conductivity measurements

The electrical conductivity measurements for Al_2O_3 ceramic specimens are carried out after each irradiation at about 800 K with 10.7 MeV protons of about 7.7×10^{-8}dpa/s dose rate. For some of the specimens an electrical field of about 320 kV/m is applied across the specimen thickness during irradiation in order to duplicate the conditions for the so-called RIED effect (see Appendix). The electrical conductivity is monitored through a commercial capacitance bridge of model 2500A the Andeen-Hagerling, Inc. Fig.3.13 shows the basic bridge circuit of the instrument. A sine wave generator supplies a 1 kHz ac signal to the precision ratio

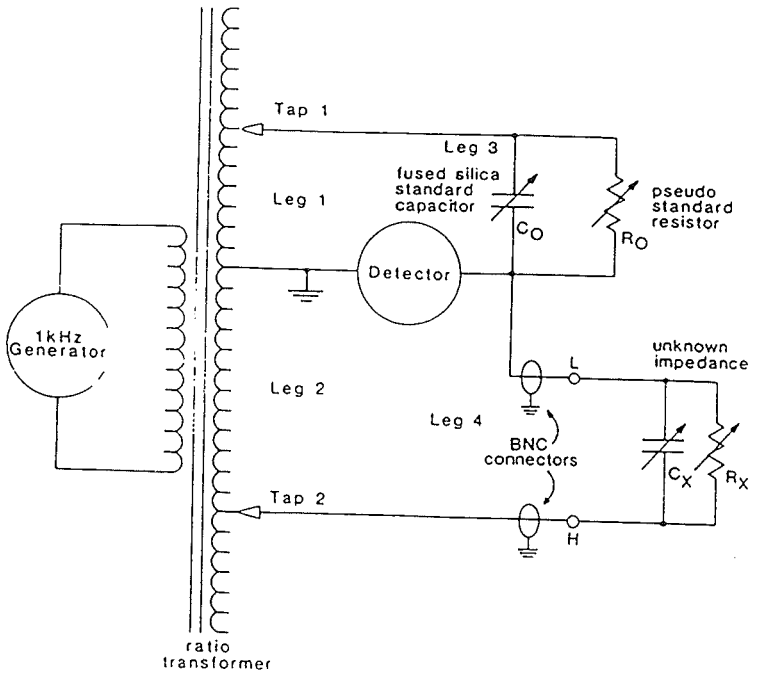

Figure 3.13: The basic bridge circuit of capacitance bridge 2500A.

transformer which forms legs 1 and 2 of the bridge. These two legs have many taps which could be selected to supply defined voltages to drive leg 3 and leg 4. Leg 3 is composed of the standard adjustable capacitor and resistor while leg 4 consists only the impedance of the specimen which is measured through the platinum films sputtered onto the surfaces (see Section 3.1). During measurement a microprocessor is used to adjust the driving voltages

given by leg 1 (V_1) and leg 2 (V_2) as well as to set the standard capacitor (C_0) and resistor (R_0) so that no voltage is measured by the detector. The specimen capacitance (C_s) and resistance (R_s) are then given by the ratio of the driving voltages (V_2/V_1) through the following equations:

$$C_s = C_0 \frac{V_2}{V_1} \tag{3.3}$$

$$R_s = R_0 \frac{V_2}{V_1} \tag{3.4}$$

The electrical conductivity measurement results for Al_2O_3 ceramics are given and discussed in the appendix.

The resistivity of tungsten is monitored by applying a known electrical current to the specimen and measuring the voltage drop across the gauge length during beam–off periods. In order to avoid specimen heating during resistance measurement which could cause influence in the specimen length measurement, the electrical current (I) is limited to a small value ($\leq$0.5 A).

Chapter 4

Experimental results

Results under irradiation will be presented on the basis of displacement doses to allow a direct comparison to other irradiation environments, e.g. in reactors. For tungsten the displacement cross section is found from interpolation of electron and neutron [67] damage rates. For ceramic materials the modified Kinchin-Pease or NRT model [9] is used to calculate the displacement cross section. Displacement doses in unit of average displacement per atom,"dpa", are obtained by multiplying the displacement cross section σ_d by the particle fluences ϕt. Table 4.1 summarizes the parameters in the dose calculation for different materials (For details cf. Ref. [68–70]) where the total energy loss ΔE inside the specimens and the minimum displacement energies for different element species $T_{d,min}$ are given. Most

Table 4.1: Parameters for displacement dose calculation.

Materials	Proton irradiation				Neutron irradiation
	$E_p(MeV)$	$\Delta E(MeV)$	$T_{d,min}(eV)$	$\sigma_d(\times 10^{-26} m^2)$	$\sigma_d(\times 10^{-26} m^2)$
c – Al_2O_3	10.7	3.65	18/76	11	3.85
s – Al_2O_3	10.7	3.7	18/76	11	3.85
SiC – HD	10.7	4.3	40/10	16.5	7.3
SiC/C	10.7	3.1	40/10	15.5	7.3
Si_3N_4	10.7	4.7	60/60	16	4.1
AlN	10.7	3.2	60/60	11	3.85
MgO	10.7	3.7	60/60	5.2	2.5
$MgAl_2O_4$	10.7	3.8	–/130	5.3	2.5
Si	9.2	2.49	22	23.3	–
s – SiO_2	9.2	3.3	25	15.3	–
v – SiO_2	9.2	2.83	25	14.8	–
W	9.2	1.91	42	54	1.55

of the materials in the present study the radiation induced changes in length or resistivity show roughly a power law dose dependence with exponents varying with temperature and/or dose range. The dose exponents are given in Table 3.2(see the last two columes) for different materials irradiated under different conditions.

4.1 Al_2O_3, SiC-HD, SiC/C, Si_3N_4 and AlN ceramics

4.1.1 Length measurements

4.1.1.1 Al_2O_3 ceramics

Relative length changes($\epsilon = \Delta l/l$) of Al_2O_3 ceramics after irradiations at different temperatures and stresses are given in Fig.4.1. Strain increases with a 0.5-0.6 power law dose dependence (Table 3.2, Fig.4.3). No stress dependence is observed at least at stresses less than 100 MPa, but a significant decrease occurs with increasing temperature. At 630°C an irradiation to about 2.9×10^{-3} dpa under a stress of 40 MPa induces actually no deformation. Modification of grain structure by sintering (cf. section 3.1) has no significant effect on the radiation induced straining.

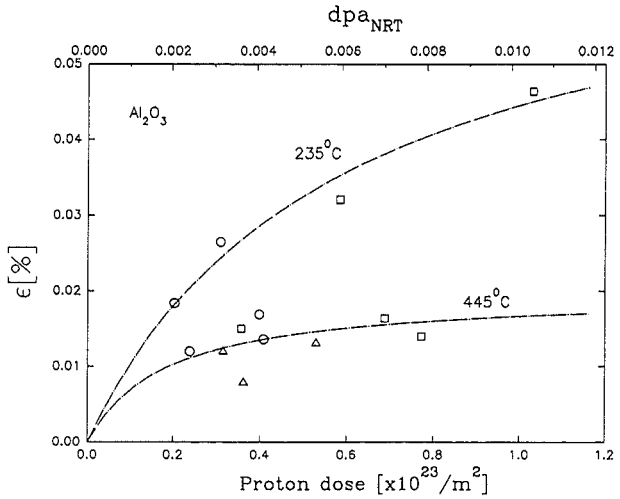

Figure 4.1: Strain of Al_2O_3 ceramics at tensile stresses of 20(□),40(○) and 100(△)MPa under 10.7 MeV proton irradiation at temperatures as indicated.

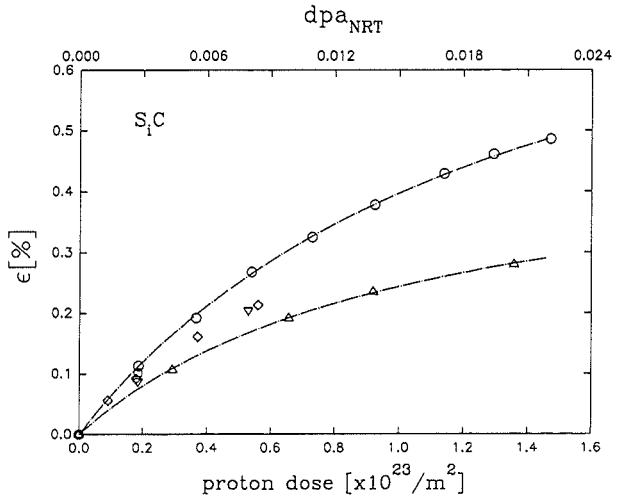

Figure 4.2: Strain of SiC-HD at tensile stresses(MPa) and temperatures(°C) of 30, 265(○); 40, 305(□); 40, 420(▽); 100, 475(◇) and 30, 505(△) under 10.7 MeV proton irradiation.

4.1.1.2 SiC-HD and SiC/C ceramics

The radiation induced strain in SiC ceramics (Fig.4.2) shows also a less than linear dose dependence(exponent 0.7 at 505°C and 0.8 at 265°C in the range before saturation), almost no stress dependence up to 100 MPa and a decrease with increasing temperature. Compared to Al_2O_3 ceramics, the strain in SiC is about one order of magnitude higher and shows strong tendency to saturation. No significant difference in straining between the two grades of materials (SiC-HD and SiC/C composite) could be seen (Fig.4.3).

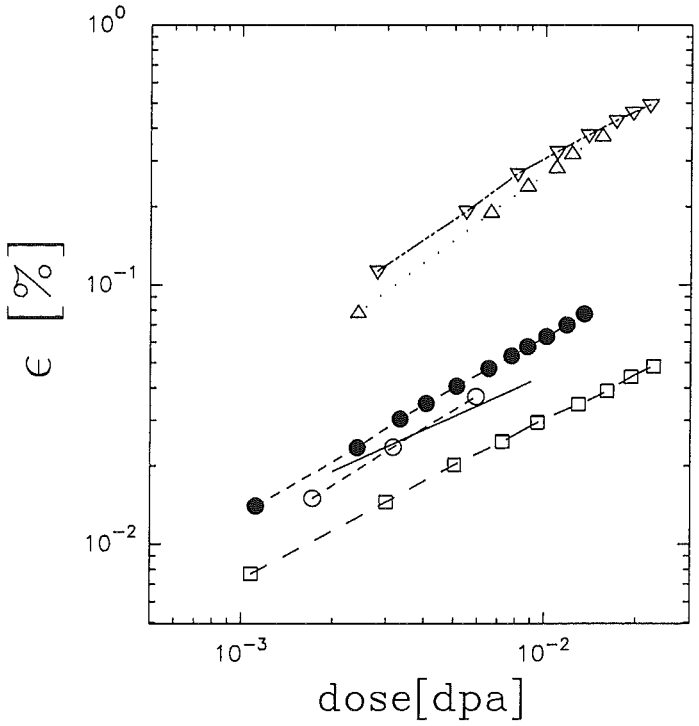

Figure 4.3: Comparison of strains induced by 10.7 MeV proton irradiation in Al_2O_3(— 235°C, 20-40 MPa), AlN(• 230°C, 40 MPa; ○ 420°C, 40 MPa), Si_3N_4(□ 230°C, 40 MPa) and SiC-HD(▽ 265°C, 30 MPa) as well as SiC/C(△ 235°C, 30 MPa).

4.1.1.3 AlN and Si_3N_4 ceramics

As shown in Fig.4.3, both AlN and Si_3N_4 ceramics deform under irradiation with strain of about the same magnitude as that of Al_2O_3 ceramics. The strain of both materials follows roughly the 2/3 power law dose dependence (Table 3.2) in the present dose range and for AlN, the radiation induced strain slightly decreases with increasing temperature. Effect of stress is not tested for these materials.

4.1.2 TEM observation

For the present maximum doses of about 0.02 dpa neither Al_2O_3 nor SiC show any detectable features under TEM.

4.2 Crystalline Al_2O_3, MgO, $MgAl_2O_4$, Si and SiO_2

4.2.1 Length measurements

4.2.1.1 Al_2O_3, MgO and $MgAl_2O_4$ crystals

Length measurement of single crystalline Al_2O_3 (s-Al_2O_3) under irradiation is only made along the c-axis and at a temperature of 220°C under a stress of 40 MPa. The radiation induced strain (Fig.4.4) is a little smaller than that of Al_2O_3 ceramics(c-Al_2O_3) irradiated at the same temperature to the same dose, and shows a transition in the dose dependence. Below 7×10^{-3} dpa the strain is almost linear to dose while above 10^{-2} dpa it changes gradually to a 0.7 power law dose dependence(Table 3.2). Stress effects are not measured.

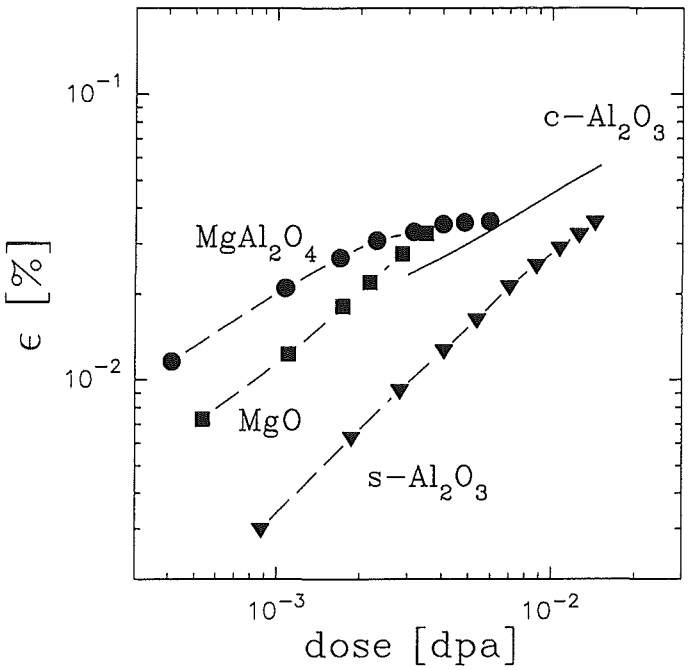

Figure 4.4: Strains of crystalline Al_2O_3, MgO and $MgAl_2O_4$ under 10.7 MeV proton irradiation at a stress of 40 MPa and temperature of 220°C. Included are results of Al_2O_3 ceramics(c-Al_2O_3) for comparison.

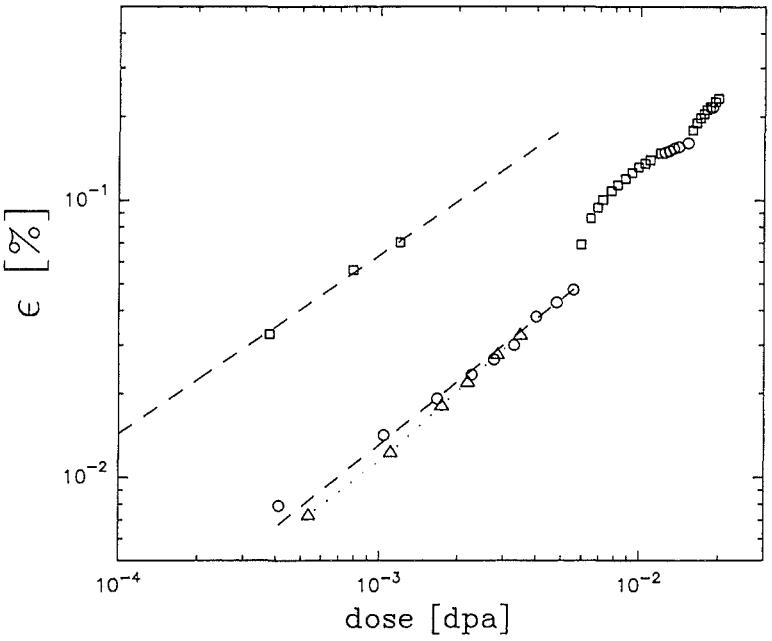

Figure 4.5: Double-log plot of uniaxial tensile strain as a function of dose of MgO during proton irradiation at 220°C under stresses of 20(o), 40(△) and 60(□) MPa,respectively.

The length change along the <110> direction of single crystalline MgO (Fig.4.4) irradiated at 220°C shows no stress dependence at stresses up to 40 MPa. The strain is of about the same magnitude as that of Al_2O_3 ceramics and follows roughly a 2/3 power law dose dependence (Table 3.2). The specimen irradiated at 60 MPa shows great enhancement in radiation induced strain(Fig.4.5), but still the strain follows the 2/3 power law dose dependence. This stress effect is confirmed by irradiating specimen first at lower stress and then at 60 MPa. The strain shows a sharp increase after change of stress and comes gradually to the 2/3 power law dose dependence. While reducing stress from 60 MPa to lower value does not show much reduction in strain, the increase in stress to 60 MPa always gives extra deformation.

The radiation induced strain in polycrystalline $MgAl_2O_4$ (Fig.4.4) at 220°C under 40 MPa tensile stress is different from that of Al_2O_3 and MgO crystals. It shows a sharp increase at beginning and then bends quite earlier ($\sim 10^{-2}$ dpa) to a saturation value of about 4×10^{-4}. The strain before saturation follows a power law dose dependence with an exponential of about 0.6 (Table 3.2). As the material fails quite often at relatively low stresses, stress effects could not be investigated. Also high temperature irradiation of the material is not possible

due to its weak thermal shock resistance (see Table 3.1).

4.2.1.2 Single crystalline Si

The strain measurements for silicon single crystals are made along the <211> direction under stresses up to 53 MPa. As shown in Fig.4.6, the strain under irradiation shows a transient at beginning and then, after about 0.02 dpa, becomes almost linear in dose dependence. Strain rate increases slightly with increasing temperature and is much higher than the extrapolated thermal creep rates [71] below about 800°C (Fig.4.7). A square root stress dependence (Fig.4.6, dashed line for 565°C) would match the data within experimental error, but alternatively the stress dependence could also be fitted by a linear stress dependence of creep rate ($\sim 5\times10^{-11}$/dpa/MPa) with an additional stress independent strain rate($\sim$0.5%/dpa) which could be ascribed to swelling.

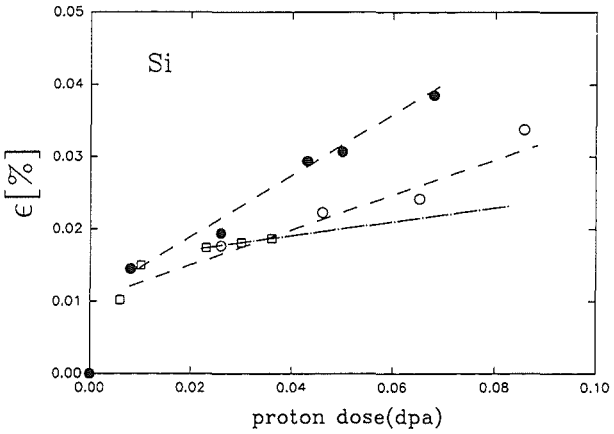

Figure 4.6: Strain of silicon under tensile stresses(MPa) and temperatures(°C) of 18, 565(o); 43, 565(•) and 53, 295(□) under 9.2 MeV proton irradiation as a function of dose.

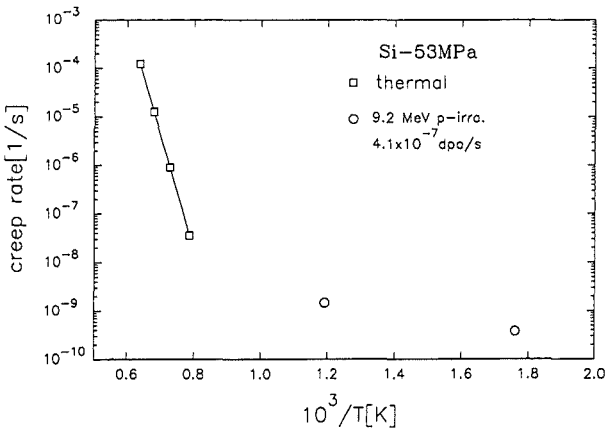

Figure 4.7: Strain rates of silicon(o) during 9.2 MeV proton irradiation of $\approx 4.1\times 10^{-7}$ dpa/s dose rate under 53 MPa tensile stress as a function of reciprocal temperature. Included are thermal creep rates(□) derived from a compilation in ref. [71].

4.2.1.3 Single crystalline SiO_2

Two single crystalline SiO_2 specimens are irradiated at 75°C and 220°C, respectively, with tensile stresses applied along the direction 36° away from the c-axis. For achieving the lower irradiation temperature the dose rate is kept at a smaller value (about 1/4 of that at 220°C).

As shown in Fig.4.8, the radiation induced strain at 220°C shows no stress effects at stresses as high as about 40 MPa. Strains follow a power law dose dependence with exponentials of 0.63 at 75°C and 0.5 at 220°C. The lower temperature irradiation induces a higher strain, but up to 0.007 dpa the strain measurement does not show any signs of radiation induced amorphization which would otherwise cause a rapid volume change up to 15% [54].

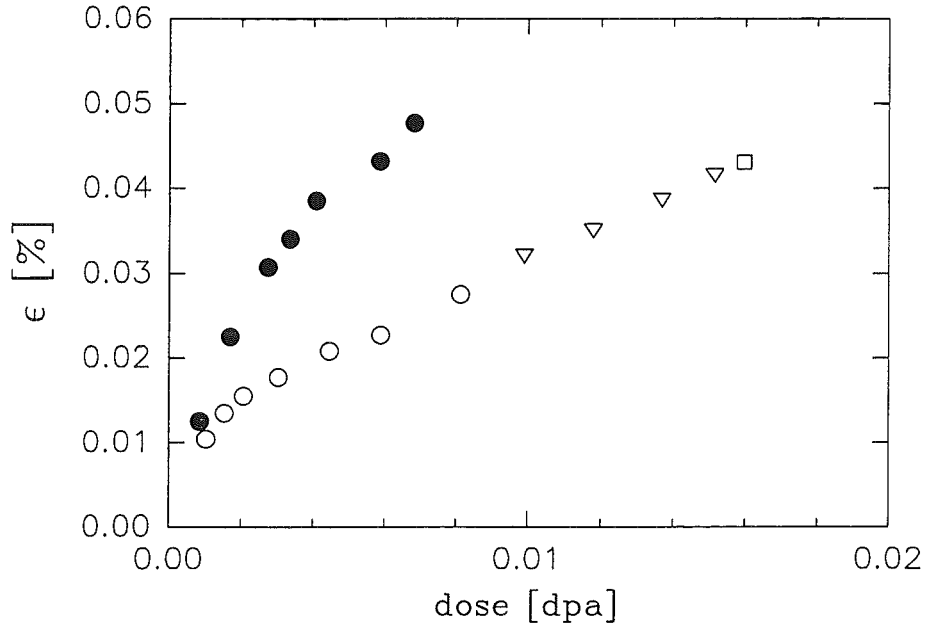

Figure 4.8: Strains induced by 9.2 MeV proton irradiation in single crystalline SiO_2 at stresses(MPa) and temperatures(°C) of 11, 75(•) and 11, 220(○); 21, 220(▽); 39, 220(□), respectively.

4.2.2 TEM observation

4.2.2.1 MgO and $MgAl_2O_4$

A high density of small black spots of about 6 nm in diameter is revealed under TEM in 10.7 MeV proton irradiated MgO at 220°C to 3.8×10^{23} p/m^2(0.02 dpa, Fig.4.9). The black spots are believed to be interstitial loops. In $MgAl_2O_4$ irradiated at the same temperature to a dose of 1.14×10^{23} p/m^2(0.006 dpa, Fig.4.10), large loop-shaped defects of diameters up to 100 nm are alighned along grain boundaries. In the grain matrix almost no defects could be seen under TEM.

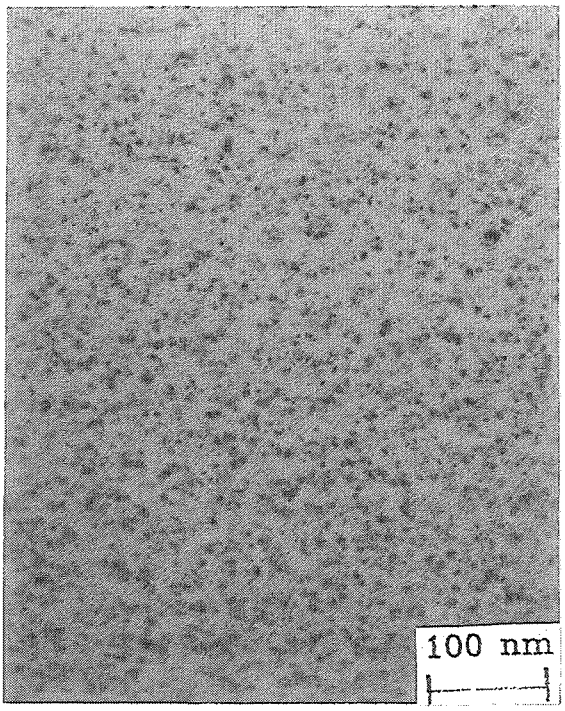

Figure 4.9: Microstructure of MgO after 10.7 MeV proton irradiation at 220°C to a dose of 3.8×10^{23} p/m^2 (0.02 dpa).

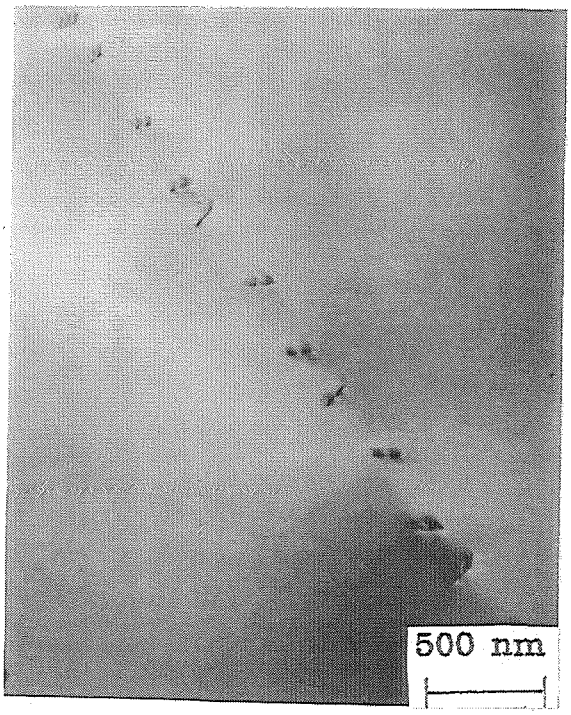

Figure 4.10: Microstructure of $MgAl_2O_4$ after 10.7 MeV proton irradiation at 225°C to a dose of 1.14×10^{23} p/m^2 (0.006 dpa).

4.2.2.2 Single crystalline Si

Fig.4.11 and Fig.4.12 show microstructures of Si specimens after irradiation with 9.2 MeV protons at 250°C and 630°C, respectively. Loops are the main defect structures for all the irradiations. Irradiation at 630°C to high dose induces in addition rod-like defects with dimensions up to 3 μm. Detailed analysis shows that the rod-like defects have loop structure. The loop density shows a strong temperature dependence but almost no dose dependence in the present dose range. At 250°C loop density is around 7×10^{21}/m^3 whereas at 630°C it is about 3×10^{19}/m^3. Loop size increases with dose at both temperatures. Irradiation at 250°C to 5.56×10^{22} p/m^2 (0.013 dpa) induces loops of about 8 nm in diameter whereas to 1.66×10^{23} p/m^2 (0.039 dpa) it is about 30 nm. High temperature irradiation at 630°C gives smaller loop density but larger loop size. At a dose of 1.06×10^{23} p/m^2 (0.025 dpa) the loop diameter is around 50 nm whereas at 3.13×10^{23} p/m^2 (0.073 dpa) it is about 180 nm.

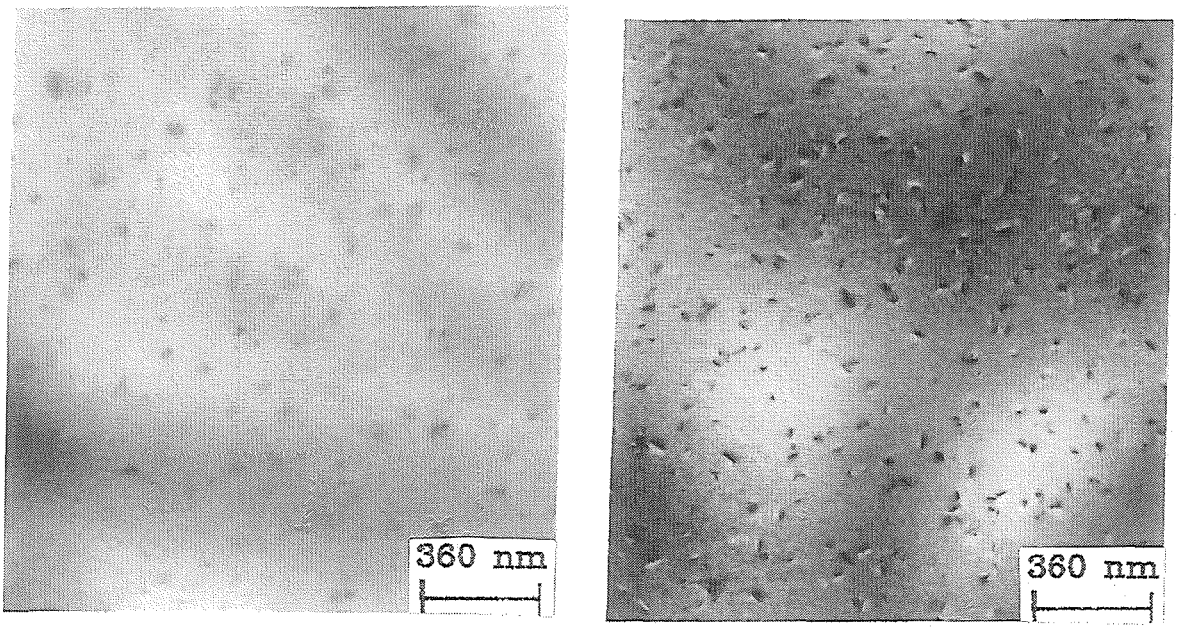

Figure 4.11: Microstructure evolution of Si specimen under 9.2 MeV proton irradiation at 250°C to doses of (1) 5.56×10^{22} p/m^2 (0.013 dpa) and (2) 1.66×10^{23} p/m^2 (0.039 dpa).

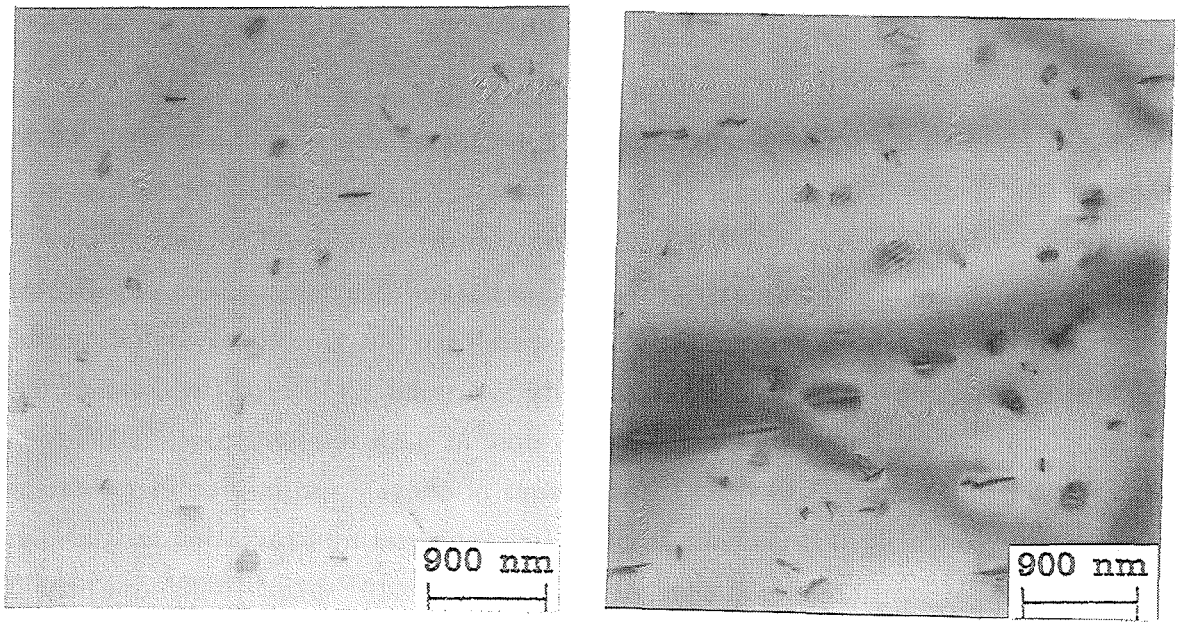

Figure 4.12: Microstructure evolution of Si specimen under 9.2 MeV proton irradiation at 630°C to doses of (1) 1.06×10^{23} p/m^2 (0.025 dpa) and (2) 3.13×10^{23} p/m^2 (0.073 dpa).

4.3 SiO_2 glass

4.3.1 Length measurements

SiO_2 glasses compacted initially under irradiation despite the applied tensile stress (Fig.4.13). Only after a certain dose the specimen began to elongate along the tensile direction with the

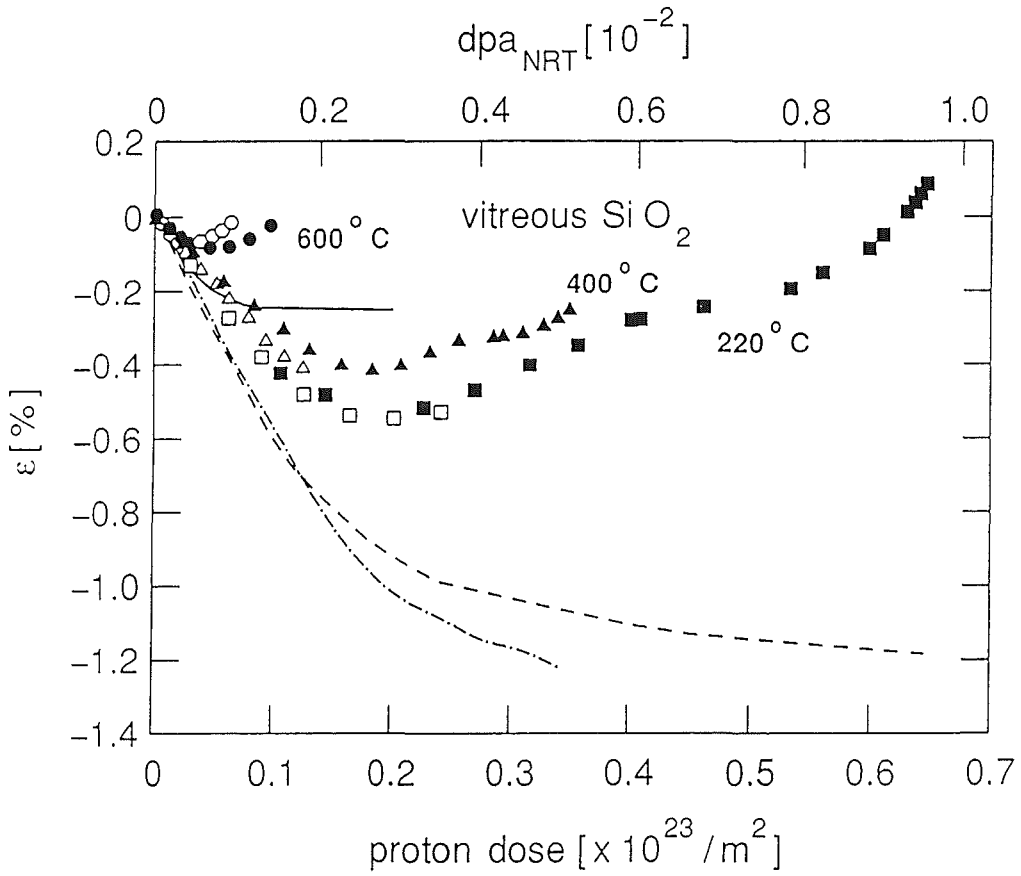

Figure 4.13: Straining of vitreous silica under 9.2 MeV proton irradiations at 220°C(□,■), 400°C(△, ▲) and 600°C(○,●) under initial stresses of ~10 MPa. Extrapolation of the dilatation period to zero allows the determination of the compaction as given for 220°C(- - - -), 400°C(– · – · –) and 600°C(——).

strain rate linearly depending on stress (Fig.4.14). During the whole irradiation the strain is linear in dose and shows little effect on temperature below about 400°C whereas at 600°C the compaction is significant smaller (Fig.4.13). Assuming that the measured strain is composed of contributions from contraction and creep, the "pure" compaction strain can be evaluated by subtracting the creep strain through the measured stress compliances (Fig.4.14). The so evaluated compaction strains are marked in Fig.4.13 with lines which show that below

about 400°C the saturation compaction strain is about 1.2% while at 600°C it is only ≈0.2%. Fig.4.15 shows the viscosity of SiO_2 glass under irradiation at a dose rate of 2.3×10^{-7} dpa/s as a function of reciprocal temperature together with the thermal viscosity data [71]. The viscosity under irradiation is evaluated by

$$\eta = \frac{\sigma}{3\dot{\epsilon}} \tag{4.1}$$

where $\dot{\epsilon}$ is the strain rate. As can be seen, the viscosity under irradiation at constant dose rate(2.3×10^{-7} dpa/s) is almost temperature independent from 220°C to 600°C with a value of about 1×10^{13} Pa·s which matches the thermal viscosity at about 1200°C.

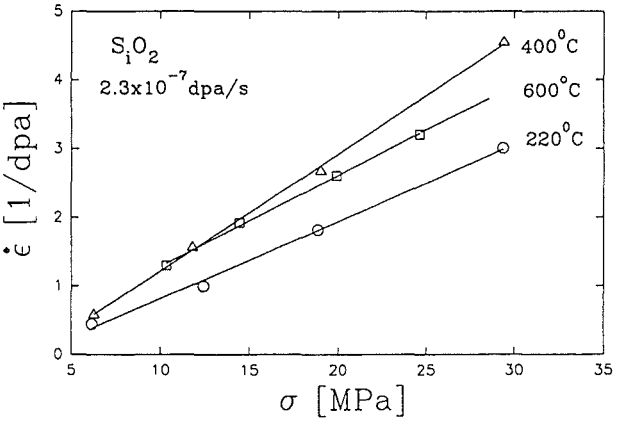

Figure 4.14: Normalized strain rates of vitreous SiO_2 at 220°C(o), 400°C (△) and 600°C(□).

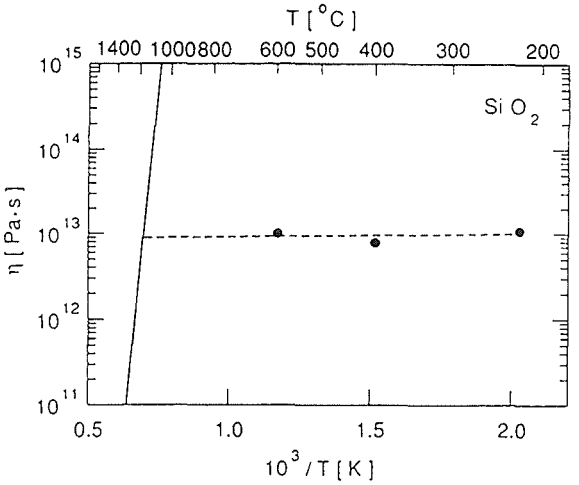

Figure 4.15: Viscosity of vitreous silica as a function of reciprocal temperature, normalized to a displacement dose rate of 2.3×10^{-7} dpa/s. The solid line gives thermal viscosity data [71].

4.3.2 Optical absorption measurements

Significant changes in optical absorption in the ultraviolet range are produced in vitreous SiO_2 by the 9.2 MeV proton irradiations. Fig.4.16 shows the absorption spectra induced by different temperature irradiations. As can be seen, the change in absorption coefficient shows a strong temperature dependence. Higher temperature irradiation gives smaller increase. No differences could be seen for specimens irradiated at the same temperature but to different doses ranging from about 1×10^{22} p/m^2 to 5×10^{22} p/m^2. Fig.4.17 to Fig.4.19 show the annealing behaviour of the radiation induced optical absorption. Significant annealing

happens only above about 400°C, even for specimens irradiated at 600°C. After annealing above 700°C the radiation induced absorption below 7 eV disappears completely whereas around 7.6 eV there is still significant absorptions which have almost the same absorption coefficient for different temperature irradiated specimens. In order to extract reasonable information from the measurements, fitting of the spectra is conducted by fixing some of the peaks known from other investigations(table 2.2) in position. It is found that the peak around 7.6 eV changes position in respect to temperatures. At temperatures below 400°C, the peak centers around 7.64 eV whereas at temperatures above 600°C it moves to 7.5 eV. The reason for this could be that the peak is composed of several peaks and the relative fractions of them change with temperature. This observation gives an explanation to the largely dispersed values reported earlier(Table 2.2). The second important feature of the present study is that between the E_1' centre(5.78 eV) and the E centre($\sim$7.6 eV) there must be peaks which are scarcely reported. These peaks are detected by comparing the radiation induced spectra of specimens irradiated at different temperatures(Fig.4.16). These spectra are best fitted by peaks centred around 6.9 eV and 6.3 eV, but with significant uncertainties due to limited resolution. Fig.4.20 gives the annealing of the E_1' centre(5.78 eV) for specimens irradiated at different temperatures. It can be seen that the centre shows strong annealing at about 500°C.

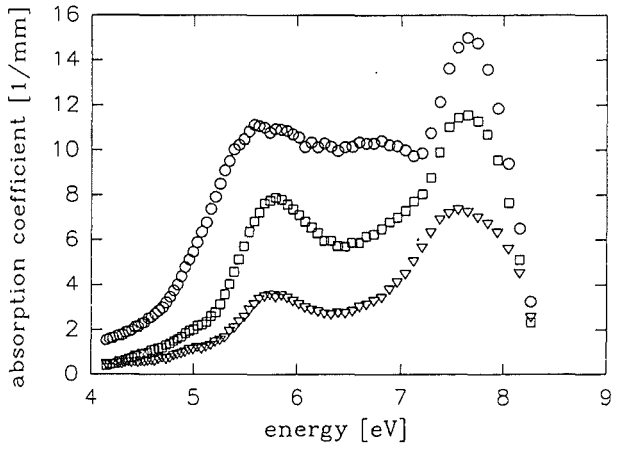

Figure 4.16: Optical absorption spectra of SiO_2 glasses due to 9.2 MeV proton irradiation at temperatures of 220°C(o), 400°C (□) and 600°C (∇), respectively (dose$\approx 10^{22}$ p/m^2).

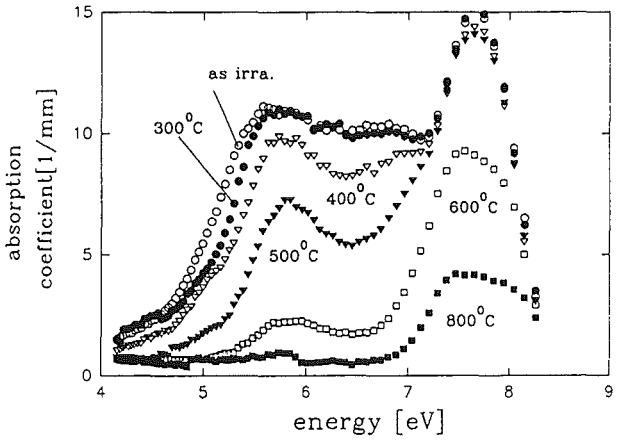

Figure 4.17: Absorption spectra of SiO_2 glass due to 9.2 MeV proton irradiation at 220°C, after successive annealings at the specified temperatures.(Annealing time 30 min.)

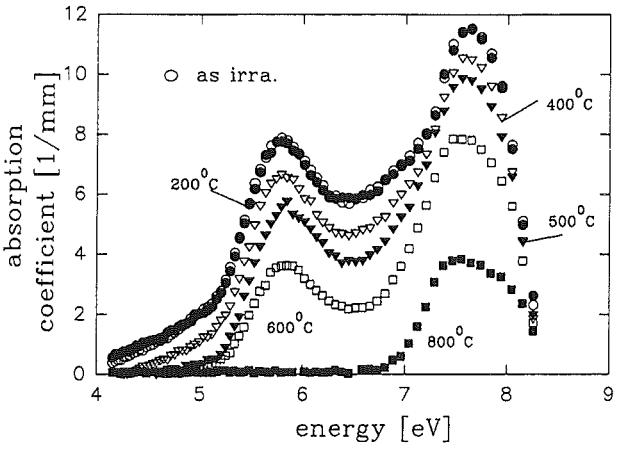

Figure 4.18: Absorption spectra of SiO_2 glass due to 9.2 MeV proton irradiation at 400°C, after successive annealings at the specified temperatures.(Annealing time 30 min.).

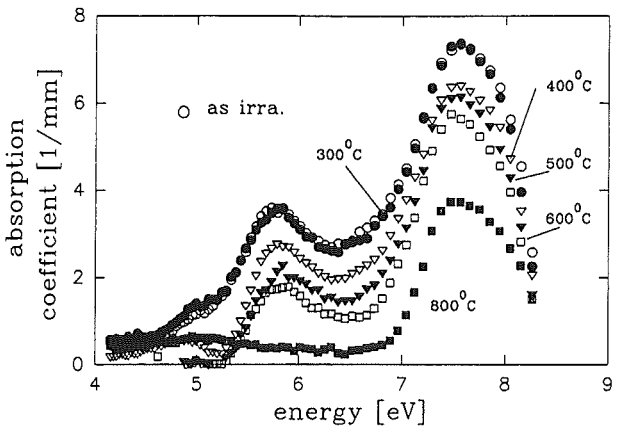

Figure 4.19: Absorption spectra of SiO_2 glass due to 9.2 MeV proton irradiation at 600°C, after successive annealings at the specified temperatures.(Annealing time 30 min.).

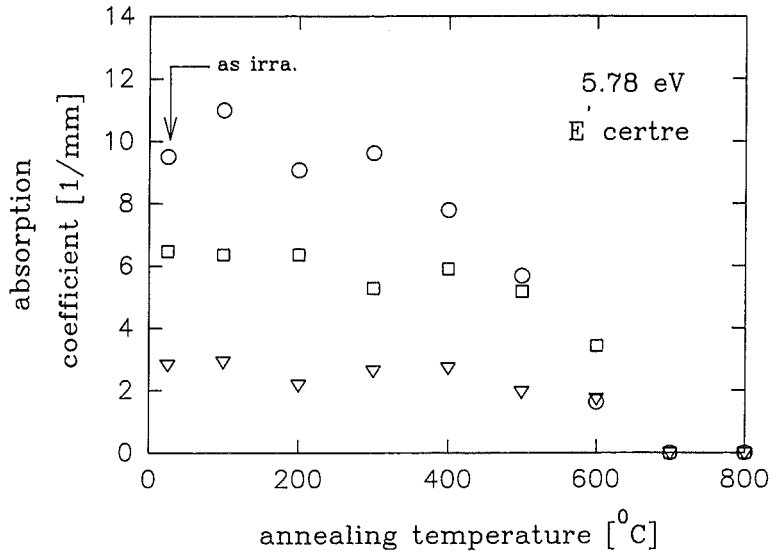

Figure 4.20: Annealing of E′ centre in SiO_2 glass irradiated with 9.2 MeV proton at temperatures of 220°C(o), 400°C(□) and 600°C(∇).

4.4 Polycrystalline tungsten

4.4.1 Length measurements

The straining of tungsten specimens at 160°C, 320°C and 520°C with and without irradiation is shown in Fig.4.21, Fig.4.22 and Fig.4.23, respectively. The strain without irradiation (open symbols) shows a sharp increase at the beginning in less than about 2 hours, which gives a transient strain with magnitude depending upon the temperature and stress. The measurement at 160°C under 330MPa gives a value around 0.004% (Fig.4.21) while at 520°C under the same stress it is around 0.08% (Fig.4.23). The transient strains measured at 320°C under 320MPa and 170MPa (Fig.4.22) are 0.0252% and 0.0134%, respectively, which possibly implies a linear dependence of transient strain on stress. After the transient period, the specimens continue elongation with a smaller strain rate which shows little change with time.

The strain under irradiation is several times higher than that of the unirradiated specimens and shows both stress and temperature dependence. After a sharp increase at the beginning, which is similar to the unirradiated case, the specimen length increases gradually with increasing dose and in most cases comes eventually to a saturation at doses which vary

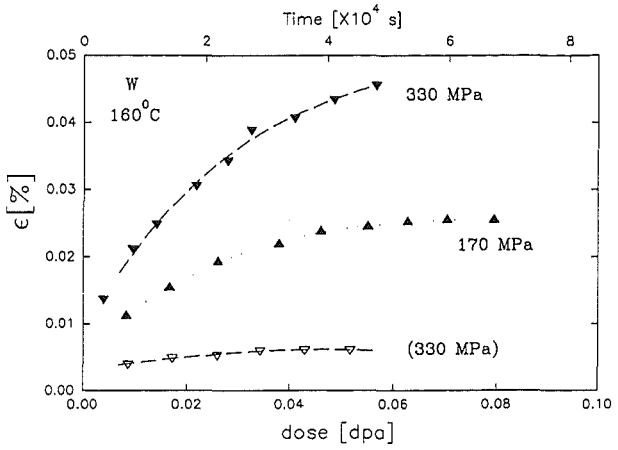

Figure 4.21: Uniaxial strain of 50 μm tungsten foils under 9.2 MeV proton irradiation at 160°C and stresses as indicated. The open symbols indicate measurements without irradiation. The time scale(upper abscissa) applies for both irradiation and annealing time.

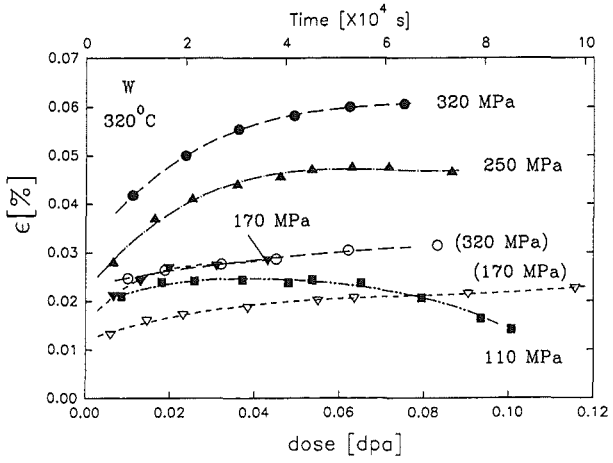

Figure 4.22: Uniaxial strain of 50 μm tungsten foils under 9.2 MeV proton irradiation at 320°C and stresses as indicated. The open symbols indicate measurements without irradiation.

with irradiation temperature and stress. A special feature shown by the specimen irradiated at 320°C under 110 MPa is a reduction in strain after about 0.05 dpa irradiation. Fig.4.24 gives the radiation induced strain, i.e. strain under irradiation minus strain without irradiation, as a function of dose. As can be seen, the irradiation at 520°C gives a rather sharp increase in strain which saturates around 0.03 dpa. The strains induced by the 160°C and 320°C irradiation under the same stress (330 MPa) increase gradually with dose and eventually approach approximately the saturation value found by the 520°C irradiation. While straining under 160°C irradiation shows no saturation in the present dose range, the radiation induced strain at 320°C saturates at doses and values which are stress dependent. At 320 MPa the strain saturates around 0.06 dpa at a value of about 0.03% while at 170 MPa it happens quite earlier (~0.02 dpa) with a saturation strain around 0.01%.

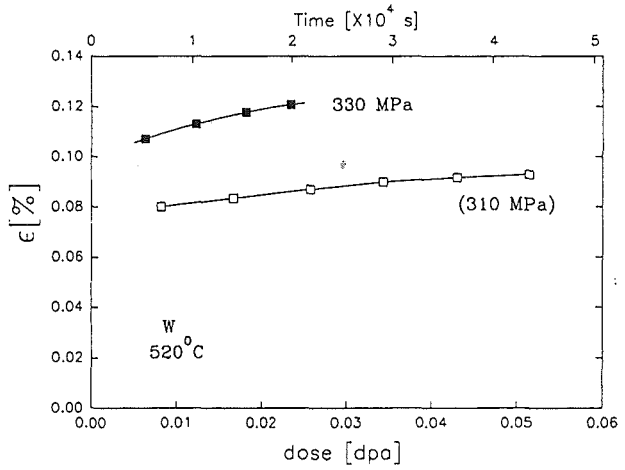

Figure 4.23: Uniaxial strain of 50 μm tungsten foils under 9.2 MeV proton irradiation at 520°C and stresses as indicated. The open symbols indicate measurements without irradiation.

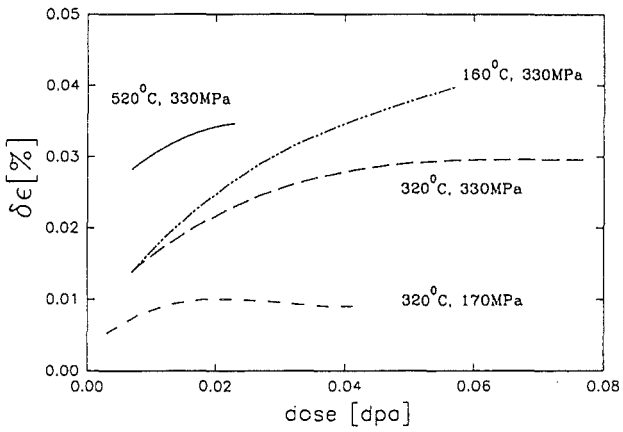

Figure 4.24: Radiation induced strain in 50 μm tungsten foils under 9.2 MeV proton irradiation at 160°C, 320°C and 520°C under stresses as indicated.

4.4.2 Resistivity measurements

The resistivity measurements with and without (open symboles) irradiation at different temperatures and stresses are shown in Fig.4.25. In all cases the resistivity changes show no stress dependence but a strong temperature dependence. Solely heating of the specimen (without irradiation) reduces the resistivity which comes to a constant value in less than about 2 hours. The measurement at 520°C gives the largest reduction in resistivity which

comes to about –9.2% of the original value. Smaller reductions are found by the 320°C and 160° C measurements with values around –4.2% and –0.84%, respectively.

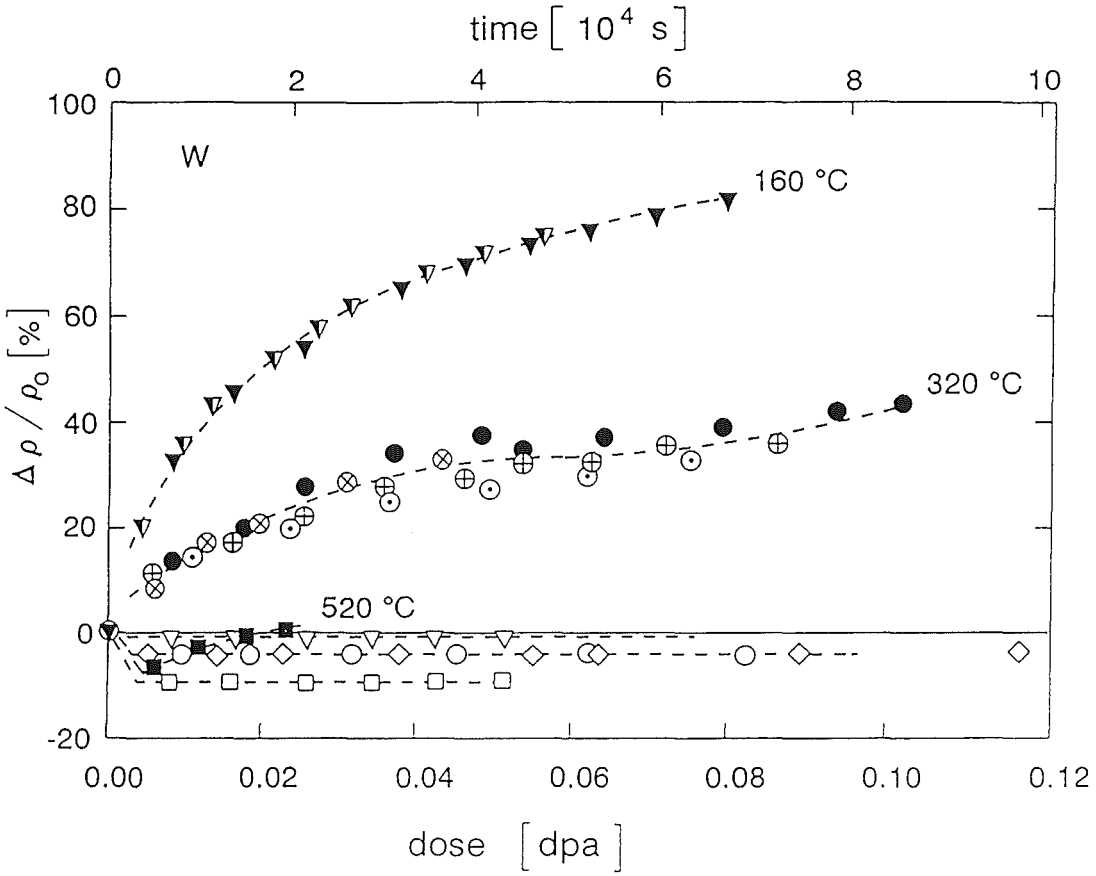

Figure 4.25: Relative resistivity change of 50 μm tungsten under 9.2 MeV proton irradiation at 160°C(∇), 320°C(o) and 520°C($\square$) as a function of dose or annealing time. The open symbols indicate measurements without irradiation. Differently filled symbols at a given temperature indicate different uniaxial stresses(c.f. Fig.4.21-4.23).

Despite the reduction in resistivity by the heating, the resistivity under irradiation shows an increase which is transient in nature. The irradiation at 160°C induces the largest increase which goes over 80% of the original value at a dose of 0.08 dpa. About 40% increase is produced by the 320°C irradiation at the same dose. The resistivity under 520°C irradiation shows an initial reduction and then increases with further irradiation which recovers the initial reduction at a dose of about 0.02 dpa. Fig.4.26 shows the radiation induced resistivity changes as a function of dose, which is evaluated by subtracting the heating contribution from the measurements under irradiation, together with the data from neutron irradiations

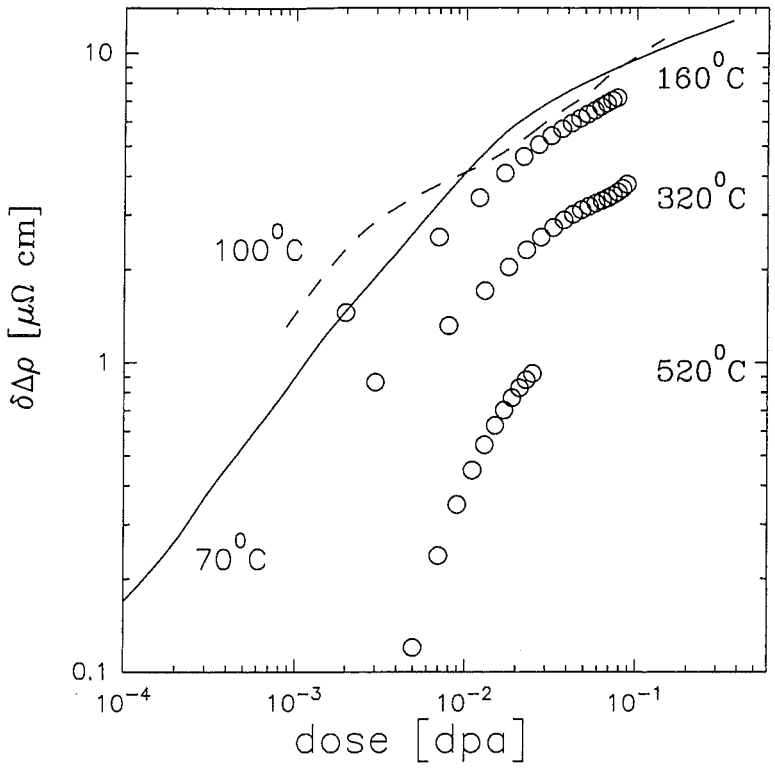

Figure 4.26: Irradiation induced resistivity change of tungsten as a function of dose at 160°C, 320°C and 520°C. Included are results from reactor irradiations(— ,measured at 77 K) and (- - -, assuming ρ_{RT}=7 $\mu\Omega$cm).

at 70°C [73] and 100°C [74]. As can be seen, the present proton data at 160°C agree very well with the two sets of neutron data on the basis of displacement dose. Fitting of the proton data at 160°C and 320°C in the low dose range (<0.04 dpa) with a power law gives an exponent of about 0.5 (Table 3.2).

4.4.3 TEM observation

The original tungsten specimens used in the present study contain dense dislocations and loops of about 20 nm in diameter(Fig.4.27). Heating of the specimen at different temperatures greatly reduced the density of loops and dislocations(Fig.4.27). Under irradiation the main feature of microstructure changes is the appearance of tiny loops of diameters around 4.4 nm(Fig.4.28 to Fig.4.30). The loop size shows almost no temperature dependence whereas the loop density decreases with temperature from $\sim 2\times10^{22}/m^3$ at 160°C to $\sim 1\times10^{22}/m^3$ at 320°C for a dose of about 1.5×10^{23} p/m^2 (0.081 dpa). Limited data seem to show that stress tends to inhibit loop nucleation.

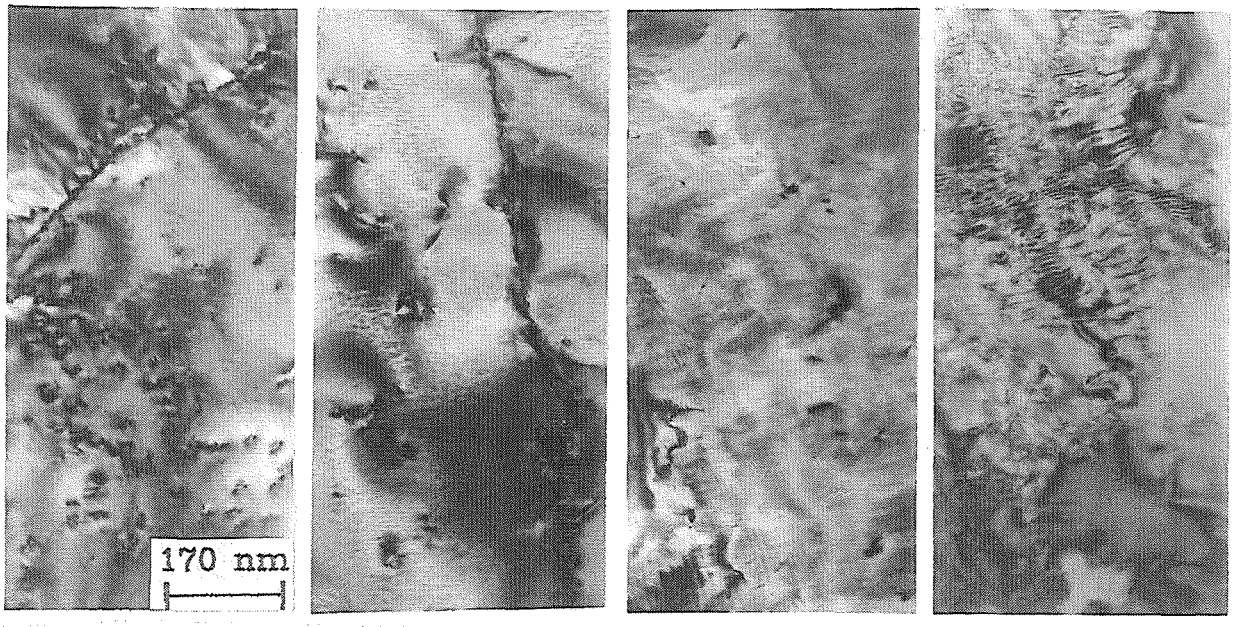

Figure 4.27: Microstructure evolution of tungsten specimen after heating at different temperatures for about 15 hours. From left to right: (1) original material, (2) 160°C, (3) 320°C and (4) 520°C.

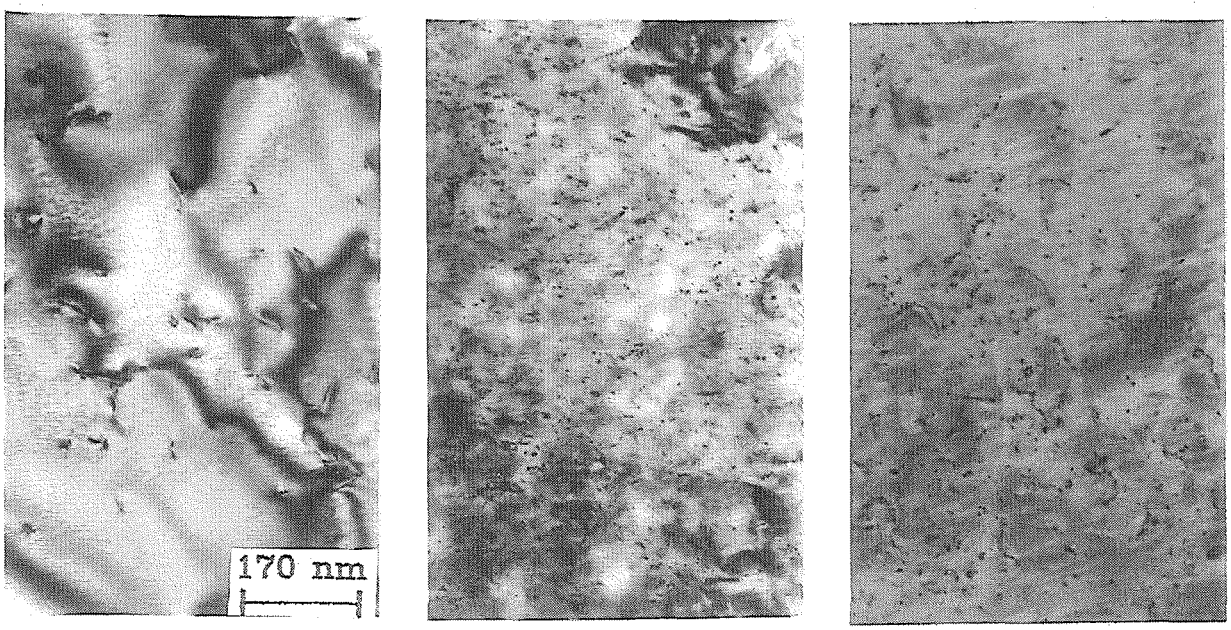

Figure 4.28: Microstructure evolution of tungsten specimen under 9.2 MeV proton irradiation at 160°C to doses of (1) 0, (2) 1.05×10^{23} p/m^2 (0.057 dpa) and (3) 1.47×10^{23} p/m^2 (0.079 dpa).

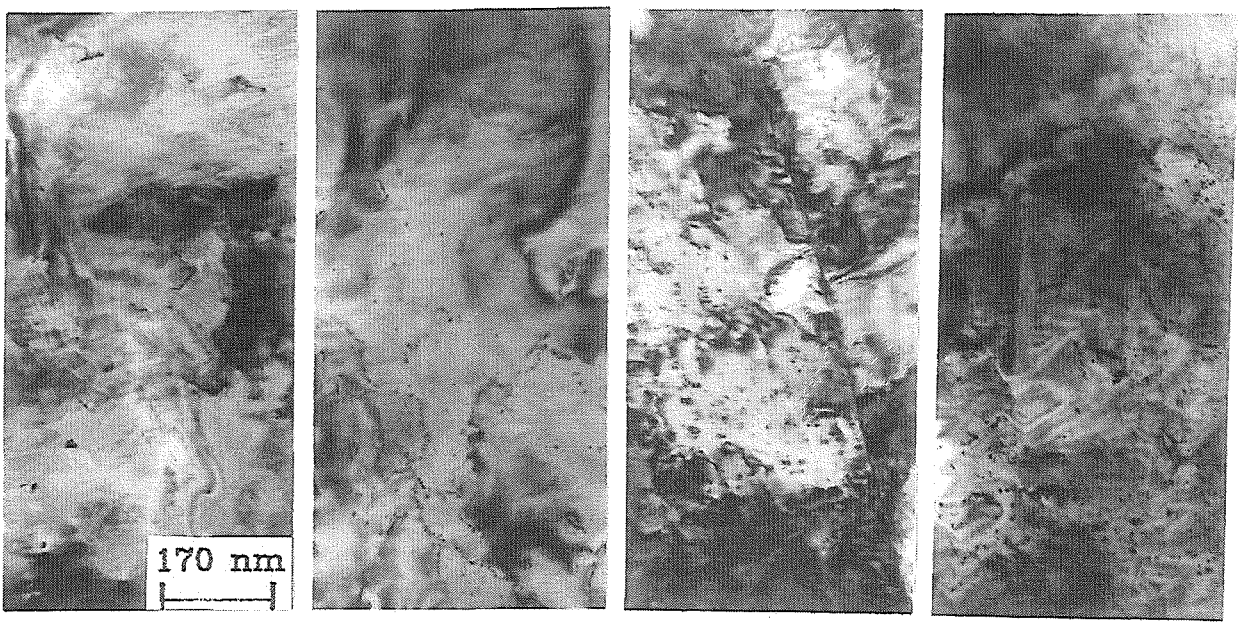

Figure 4.29: Microstructure evolution of tungsten specimen under 9.2 MeV proton irradiation at 320°C to doses of (1) 0, (2) 3.69×10^{22} p/m^2 (0.02 dpa), (3) 1.33×10^{23} p/m^2 (0.072 dpa) and (4) 1.57×10^{23} p/m^2 (0.085 dpa).

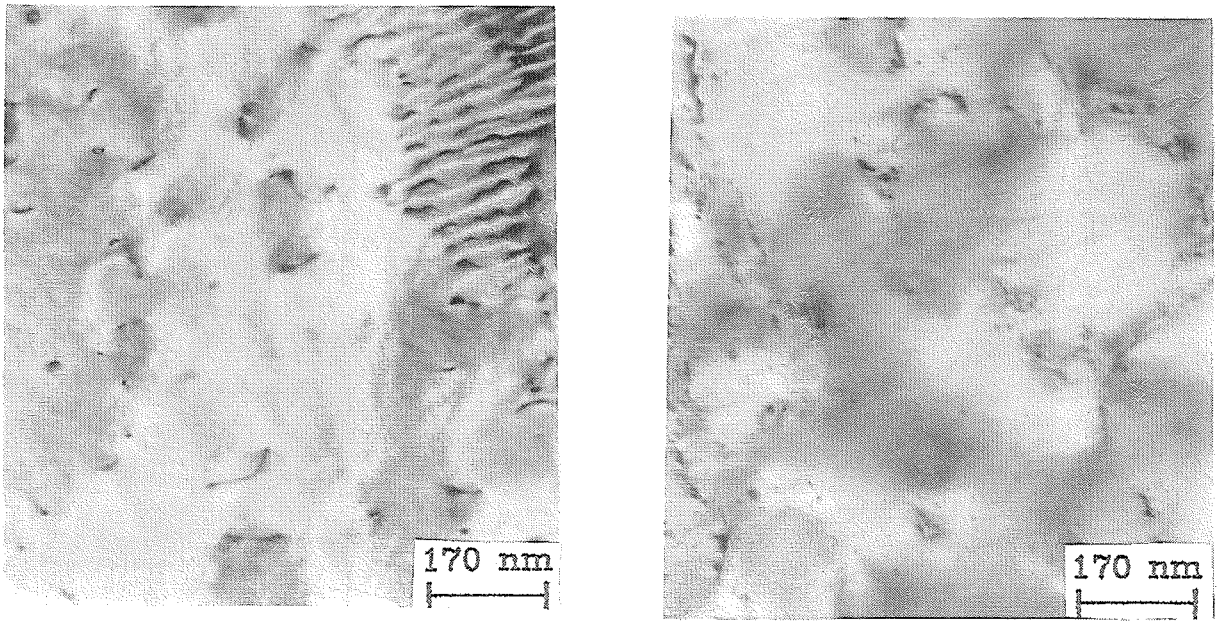

Figure 4.30: Microstructure evolution of tungsten specimen under 9.2 MeV proton irradiation at 520°C to doses of (1) 0, (2) 4.38×10^{22} p/m^2 (0.024 dpa).

Chapter 5

Theoretical Modelling

In this chapter it is attempted to adopt existing models to the conditions prevailing for the present experiments and obtain expressions which should describe the radiation induced strain in both crystalline and glassy materials. These expressions are fitted to the experimental observations and discussed analytically to uncover the underlying mechanisms.

5.1 Radiation induced deformation in crystalline materials

5.1.1 Model construction

As shown in Section 2.1, defect production in crystalline materials occurs mainly by atomic displacements which produce point defects. Under certain conditions the radiation induced point defects react with each other resulting in recombination or agglomeration or they are trapped by sinks. These processes can be described by rate equations which include a production term, a recombination term and a sink term. As has been discussed in Section 2.1.2.2 in the intermediate temperature range where one type of point defect (mostly the interstitial) is mobile, the earlier calculations do not predict the saturation behaviour of the radiation induced macroscopic changes [32, 33]. We believe that this is due to the neglect of the spontaneous recombination of point defects. Because of the immobility of vacancies in this temperature range the irradiated volume will be gradually filled by vacancies which continuously reduces the further production of point defects. This saturation behaviour is determined by the point defect recombination volume v_s of the material. Therefore the rate

equations should be written as follows:

$$\frac{dC_v}{dt} = K(1 - v_s C_i - v_s C_v) - q(D_i + D_v)C_i C_v - Z_v D_v (C_v - C_{v0})(\rho_d + \rho_l) \tag{5.1}$$

$$\frac{dC_i}{dt} = K(1 - v_s C_i - v_s C_v) - q(D_i + D_v)C_i C_v - Z_i D_i C_i (\rho_d + \rho_l) \tag{5.2}$$

$$\frac{dR_L}{dt} = \frac{1}{b}[Z_i D_i C_i - Z_v D_v (C_v - C_{v0})] \tag{5.3}$$

$$\rho_l = 2\pi R_L C_L \tag{5.4}$$

where symbols are the same as defined in Section 2.1.2 and D_i, D_v are given by $D_i = D_{i0}e^{-E_i^m/k_B T_{irr}}$ and $D_v = D_{v0}e^{-E_v^m/k_B T_{irr}}$, where E_i^m and E_v^m are the activation energies of diffusion for interstitial and vacancy, respectively. T_{irr} is the irradiation temperature. The spontaneous recombination between interstitial and vacancy is included by introducing $v_s C_i$ and $v_s C_v$ in the defect production term[see eq.(5.1) and eq.(5.2)], which are the probabilities that a defect meets its anti-partner. Even if both type of point defects are mobile, the above production term is still right. But in this case the point defect concentration is very small even when the defect production has reached steady state. If, on the other hand, the diffusion coefficients of both type of defects are set to zero, the rate equations change to the following form which describes the low temperature irradiation behaviour:

$$\frac{dC}{dt} = K(1 - 2v_s C) \tag{5.5}$$

where $C = C_i = C_v$. A more detailed description of the low temperature irradiation induced defect accumulation is given by [31]

$$\frac{dC}{dt} = K(1 - v_s C)^2 \tag{5.6}$$

which includes also the overlap of recombination volume.

5.1.2 Numerical calculation

For making numerical calculations we would like to concentrate on the intermediate temperature range where most of the present experiments are conducted. As interstitials are mobile, we can take $\frac{dC_i}{dt} = 0$, which is soon reached after beginning of irradiation. Then the calculation becomes much easier because there is only one differential equation left:

$$C_i = \frac{K(1 - v_s C_v)}{K v_s + q(D_i + D_v)C_v + Z_i D_i (\rho_d + \rho_l)} \tag{5.7}$$

$$\frac{dC_v}{dt} = K(1 - v_s C_i - v_s C_v) - q(D_i + D_v)C_i C_v - Z_v D_v (C_v - C_{v0})(\rho_d + \rho_l) \tag{5.8}$$

$$\frac{dR_L}{dt} = \frac{1}{b(\rho_d + \rho_l)} \frac{dC_v}{dt} \tag{5.9}$$

$$\rho_l = 2\pi R_L C_L \tag{5.10}$$

The numercial calculation is then carried out by the following steps:

- Set parameters
- Set initial values
- Solve differential equations (eq. 5.8, 5.9)
- Set time step Δt
- Calculate swelling after time(t+Δt) (eq. 2.14)

The time step is chosen such that on one hand the induced error is small while on the other hand the total calculation time is not too long. Table 5.1 lists the parameters used in calculation of radiation induced swelling of Al_2O_3 and MgO irradiated at 500 K. Because no detailed numerical values are known for ceramic materials, they have been chosen equal for both materials. Furthermore, the loop volume density C_L is taken as constant according to experiments (see Section 2.1.1.2). Other parameters are $Z_i = 1.1$, $Z_v = 1.0$, $D_{v0} = D_{i0} = 10^{-4}\ m^2/s$. The calculation results are given together with the experimental measurements in chapter 6. Fig.5.1 shows a typical result of the calculation.

Table 5.1: Parameters for numerical calculation

Materials	K $[dpa/s]$	C_{v0}	C_L $[1/m^3]$	q $[1/m^2]$	v_s $[\Omega]$	ρ_d $[1/m^2]$	E_i^m $[eV]$	E_v^m $[eV]$	R_L^{max} $[nm]$
Al_2O_3 and MgO	2×10^{-7}	0	5×10^{22}	2×10^{19}	30	10^{12}	0.2	2.0	27

5.1.3 Analytical discussion

In this section the results of the numerical calculation are discussed analytically to show the general features of the radiation induced deformation in crystalline materials.

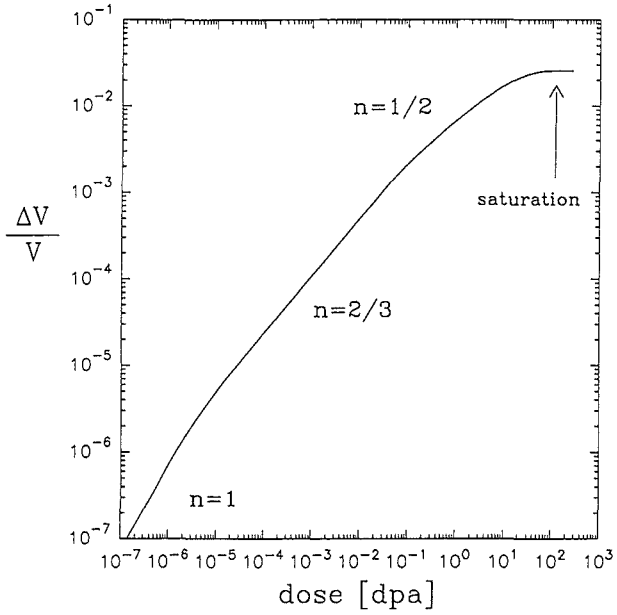

Figure 5.1: Typical numerical calculation result.

Assuming that after a short time of irradiation the interstitial reaches steady state, i.e.

$$\frac{dC_i}{dt} = 0 \tag{5.11}$$

then the interstitial concentration is given by eq.(5.7). Inserting eq.(5.7) into eq. (5.1) gives

$$\frac{dC_v}{dt} = K(1 - v_s C_v)\frac{Z_i D_i(\rho_d + \rho_l)}{Kv_s + q(D_i + D_v)C_v + Z_i D_i(\rho_d + \rho_l)} - Z_v D_v(C_v - C_{v0})(\rho_d + \rho_l) \tag{5.12}$$

If $D_v \approx 0$ then

$$\frac{dC_v}{dt} = \frac{K(1 - v_s C_v)}{1 + \frac{(Kv_s/qD_i)+C_v}{Z_i(\rho_d+\rho_l)/q}} \tag{5.13}$$

From the parameters listed in Table 5.1 it can be seen that

$$\frac{Kv_s}{qD_i} \ll \frac{Z_i(\rho_d + \rho_l)}{q} \ll \frac{1}{v_s} \tag{5.14}$$

Therefore eq.(5.13) becomes

$$\frac{dC_v}{dt} = \frac{K(1 - v_s C_v)}{1 + \frac{C_v}{Z_i(\rho_d+\rho_l)/q}} \tag{5.15}$$

(a) If $C_v \ll \frac{Z_i(\rho_d+\rho_l)}{q}$ then $\frac{dC_v}{dt} = K$ which gives $C_v = Kt$. This is the dose dependence at the beginning of irradiation especially in materials with high dislocation density (e.g. cold worked).

(b) For $C_v \approx \frac{Z_i(\rho_d+\rho_l)}{q}$ and therefore $C_v \ll \frac{1}{v_s}$ (see eq. (5.14)), one obtains:

$$\frac{dC_v}{dt} = \frac{K}{1 + \frac{C_v}{Z_i(\rho_d+\rho_l)/q}} \tag{5.16}$$

- If $\rho_d \gg \rho_l$, i.e. at small dose or in cold worked material, eq.(5.16) becomes

$$C_v + \frac{1}{2Z_i\rho_d/q}C_v^2 = Kt \tag{5.17}$$

It can be seen that for $C_v < \frac{2Z_i\rho_d}{q}, C_v = Kt$ while for $C_v > \frac{2Z_i\rho_d}{q}, C_v \propto (Kt)^{1/2}$, This is the case for materials with high dislocation density or low loop density.

- If $\rho_d \ll \rho_l$, then eq.(5.16) yields:

$$\frac{dC_v}{dt} = \frac{K}{1+\frac{C_v}{Z_i\rho_l/q}} \tag{5.18}$$

Assuming that all interstitials are accumulated in loops, then according to the law of conservation of matter one gets(c.f. eq.(2.22))

$$\rho_l = 2\sqrt{\frac{\pi C_L C_v}{b}} \tag{5.19}$$

Replacing ρ_l in eq.(5.18) by eq.(5.19) gives

$$\frac{dC_v}{dt} = \frac{K}{1+\frac{q}{2Z_i}\sqrt{\frac{b}{\pi C_L}}C_v^{1/2}} \tag{5.20}$$

which gives the following relation:

$$C_v + \frac{q}{3Z_i}\sqrt{\frac{b}{\pi C_L}}C_v^{3/2} = Kt \tag{5.21}$$

Eq.(5.21) shows that for $C_v < (\frac{3Z_i}{q})^2(\frac{\pi C_L}{b})$ one obtains $C_v \approx Kt$ and for $C_v > (\frac{3Z_i}{q})^2(\frac{\pi C_L}{b})$, $C_v \propto (Kt)^{2/3}$, i.e.

$$C_v \approx (\frac{9\pi Z_i^2 C_L}{bq^2})^{1/3}(Kt)^{2/3} \tag{5.22}$$

This is the case for low dislocation density or high loop density.

In many cases it is found that growing of loops results in the formation of dislocation networks. According to eq.(5.17) and eq.(5.21) this will change the dose dependence of radiation induced strain. In the loop dominating regime the strain follows a 2/3 power law dose dependence whereas when dislocation networks are formed it changes to a 1/2 power law dose dependence. This situation is included in the numerical calculation by assuming that networks are formed when loop radius reachs the value $R_L^{max} = (\frac{1}{C_L})^{\frac{1}{3}}$ which is assumed to be the maximum achievable loop radius of the material under the irradiation condition.

The calculation continues with a constant dislocation line density which includes the loop contributions(i.e. $\approx \rho_d + 2\pi R_L^{max} C_L$). The last column in Table 5.1 gives the maximum loop radius for the two materials.

At very high dose the defect production will saturate according to eq.(5.12) which shows that for $D_v = 0$

$$C_v^{\infty} = \frac{1}{v_s} \tag{5.23}$$

while for $D_v \neq 0$, but still $D_v \ll D_i$, one obtains

$$Z_v D_v q C_v^{\infty} [\frac{K v_s}{q D_i} + \frac{Z_i(\rho_d + \rho_l)}{q} + C_v^{\infty}] = K Z_i (1 - v_s C_v^{\infty}) \tag{5.24}$$

Together with eq.(5.14) one obtains:

$$Z_v D_v q (C_v^{\infty})^2 \approx K Z_i (1 - v_s C_v^{\infty}) \tag{5.25}$$

which shows that with increasing D_v (i.e. increasing temperature) the saturation concentration of vacancies falls gradually below $1/v_s$.

5.2 Radiation induced deformation and viscous flow in glassy materials

Soon after the observation of neutron irradiation induced compaction of v-SiO_2, it was realized [75] that displacement damage alone cannot explain the large density changes induced by one neutron event. It was therefore proposed that thermal spikes could be the source for producing the compaction. A more detailed explanation is that the atoms inside a thermal spike re-adjust themselves and form a more dense arrangement which is then frozen in when the thermal spike chills [53]. Later, the radiation induced viscous flow of v-SiO_2 was also attributed to the formation of thermal spikes as it was found that the stress relaxation is more pronounced near the end of the proton range [59]. At that time knowledge on radiation damage including ranges of ions etc was not well established, the thermal spike proposition was therefore a speculation rather than a convincing explanation.

Recently, Trinkaus [76] reconsidered the viscous behaviour of glassy materials under irradiation by using a more elaborate thermal spike concept. By detailed analysis of the characters of thermal spikes such as size, shape, temperature distribution, duration and relaxation, he derived an expression for the apparent viscosity η of amorphous materials under irradiation:

$$\eta = (\frac{\pi e^3}{6})^{1/2} \frac{(7 - 5\nu)}{15(1 - \nu)} \frac{\mu \rho C' (T^* - T_{irr})}{\phi (dE'/dx)} \tag{5.26}$$

where ν is Poisson's ratio, μ is the shear modulus, ρ is the density, C' the specific heat, ϕ the flux of incident particles, dE'/dx the part of the stopping power consumed in thermal spikes, T^* is the material flow temperature. The application of the model to the heavy ion irradiation of glassy materials shows reasonable agreement. To explain the viscous behaviour of the 9.2 MeV proton irradiated v-SiO_2, a stopping power of about 5×10^7 eV/m would be required. This value is about 6 times higher than the nuclear stopping power alone(Fig.2.2). If taking into account that the energy deposited in producing thermal spikes in the present case is about 20% of the total energy deposition through nuclear collisions(Fig.2.4, assuming that the energy for producing one thermal spike is about 5 keV), then the evaluated viscosity would be more than one order of magnitude higher than the measured one. It is therefore concluded that although thermal spikes may contribute to the radiation induced viscous flow, they cannot sufficiently explain the observed viscous behaviour. Electronic processes such as ionization etc must also contribute to the effect.

Actually the ionization induced compaction and viscous flow in v-SiO_2 have been realized as early as that induced by displacement processes. Electrons as well as X-ray [50] were found to induce compaction. Later a stress relaxation, which is believed to be due to the radiation induced viscous flow, was also observed in low energy electron irradiated v-SiO_2 [59]. Furthermore, the different dose dependence of the electron and neutron irradiation induced compaction in v-SiO_2 [51] may also indicate the different damage mechanisms. Whereas the damage mechanism based on displacement processes is attributed to thermal spikes, the damage mechanism for electronic processes may be attributed to the breaking of atomic bonds. Based on this idea a simple semi-empirical model is presented in the following to describe the radiation induced deformation and viscous flow in glasses irradiated above room temperature.

5.2.1 Model construction

The model is based mainly on the following two experimental observations:

(a) Under irradiation SiO_2 glass shows compaction which saturates at higher doses.

(b) The viscosity of the glassy materials (SiO_2 and B_2O_3) is greatly reduced during irradiation. At not too high temperatures the radiation induced viscosity shows an athermal behaviour and is inversely proportional to the dose rate. At high temperatures no radiation induced or enhanced viscous flow is observed and the viscous behaviour of the material is totally governed by thermally

activated processes.

It is assumed that the radiation induced compaction of the glassy material is due to the formation of new atomic bonds which result in a denser atomic arrangement. During irradiation the atoms can have either bondings of the original glass(g1-type bondings) or new type bondings(g2-type bondings). Transition between the two different types of bondings could occur through breaking of bonds. The atomic energy level of the atoms in g1-type bonding and g2-type bonding are taken as E_{g1} and E_{g2}, respectively, and that of the atoms with broken bonds as E_b. It is further assumed that under irradiation of a glass specimen with total number of N atoms and N bonds, N_{g1} atoms have g1-type bonds (or are in g1-type glass state) and N_{g2} atoms have g2-type bonds(or are in g2-type glass state) and N_b atoms have broken bonds(or are in broken state). Then, as shown in Fig.5.2, the following reaction equations are obtained:

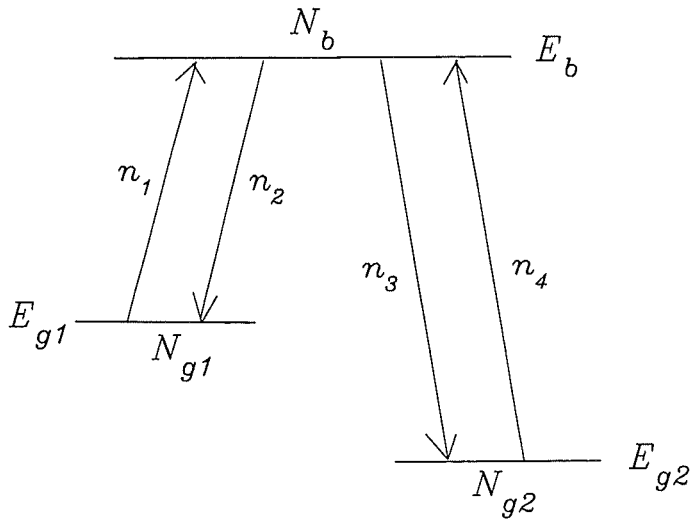

Figure 5.2: Idealized description of glassy materials under irradiation by three atomic energy levels.

$$\frac{dN_{g1}}{dt} = n_2 - n_1 \tag{5.27}$$

$$\frac{dN_{g2}}{dt} = n_3 - n_4 \tag{5.28}$$

where n_1, n_2, n_3 and n_4 are the transition rate of atoms between states. With

$$N_{g1} + N_{g2} + N_b = N \tag{5.29}$$

one obtains

$$\frac{dN_b}{dt} = -\frac{dN_{g1}}{dt} - \frac{dN_{g2}}{dt} = n_1 + n_4 - n_2 - n_3 \tag{5.30}$$

Assuming that the number of broken bonds decays with a time constant of λ', then

$$n_2 + n_3 = \lambda' N_b \tag{5.31}$$

therefore

$$\frac{dN_b}{dt} = -\lambda' N_b + n_1 + n_4 \tag{5.32}$$

In eq.(5.32) n_1 represents the number of atoms transformed from g1-type glass state to the broken state in unit time, and can be written as

$$n_1 = \nu_{g1} e^{-(E_b - E_{g1})/k_B T_{irr}} \cdot N_{g1} + K_{g1} \cdot N_{g1} \tag{5.33}$$

where the first term describes the thermally activated transition and the second term describes the radiation induced transition. Here ν_{g1} is the atom vibrating frequence of the original glass and K_{g1} is the transition rate induced by the irradiation. The value of K_{g1} could be evaluated by

$$K_{g1} = \frac{\beta \frac{\Delta E}{\Delta x} \Omega_{g1}}{\Delta E_{g1}} \phi \tag{5.34}$$

where ΔE_{g1} is the energy required to break a g1-type bond (here $\Delta E_{g1} = E_b - E_{g1}$). β is the efficiency that the energy deposition is consumed in breaking of bonds. $\frac{\Delta E}{\Delta x}$ represents the total energy deposited by one irradiation particle in the unit trajectory length through both ionization and nuclear collision, ϕ is the dose rate and Ω_{g1} is the atomic volume of the original glassy material.

Similarly, n_4, the number of atoms transformed from g2-type glass state to the broken state, could be written as

$$n_4 = \nu_{g2} e^{-(E_b - E_{g2})/k_B T_{irr}} \cdot N_{g2} + K_{g2} \cdot N_{g2} \tag{5.35}$$

with ν_{g2} the vibration frequence of atoms in the g2-type glass state and K_{g2} the transition rate induced by the irradiation.

Replacing n_1 and n_4 in eq.(5.32) by eq.(5.33) and eq.(5.35) and taking into account of eq.(5.29) one obtains:

$$\begin{aligned} \frac{dN_b}{dt} &= -(\lambda' + \nu_{g1} e^{-\Delta E_{g1}/k_B T_{irr}} + K_{g1}) N_b + (\nu_{g2} e^{-\Delta E_{g2}/k_B T_{irr}} + K_{g2} \\ &\quad - \nu_{g1} e^{-\Delta E_{g1}/k_B T_{irr}} - K_{g1}) N_{g2} + (\nu_{g1} e^{-\Delta E_{g1}/k_B T_{irr}} + K_{g1}) N \end{aligned} \tag{5.36}$$

here $\Delta E_{g2} = E_b - E_{g2}$.

As the radiation induced compaction shows saturation with prolonged irradiation, we make the assumption that the number of atoms which could have g2-type bondings has an upper limit(denominated as N_t) and propose that the time dependence of N_{g2} is given by the following equation:

$$\frac{dN_{g2}}{dt} = P_0 \frac{N_t - N_{g2}}{N} \lambda' N_b \tag{5.37}$$

where P_0 is a constant. Eq.(5.36) together with eq.(5.37) describes the radiation induced compaction as a function of dose. If the saturation compaction of the material is Σ_c in length ($\Sigma_c = \varepsilon_c^{sat}$), then the contribution to compaction by one atom existing in at the g2-type glass state is $\frac{\Sigma_c}{N_t}$. Therefore the compaction rate can be written as:

$$\frac{d\varepsilon_c}{dt} = \frac{\Sigma_c}{N_t} \frac{dN_{g2}}{dt} \tag{5.38}$$

where ε_c is the compaction strain at time t.

Based on the primary propositions of the present model we could further suppose that a glass will undergo viscous flow if the atoms located at the breaking state re-adjust themselves with respect to the stress direction during the time when they are becoming again bonded, i.e. when they are falling into g1-type glass state or g2-type glass state again. Therefore the creep rate $\frac{d\varepsilon}{dt}$, which is linear in stress σ, could be written as:

$$\frac{d\varepsilon}{dt} = Q_0 \sigma \frac{\lambda' N_b}{N} \tag{5.39}$$

where Q_0 is a constant and $Q_0\lambda'$ represents the probability that under unit stress the atoms, which undergo transition from breaking state to bonded state, adjust themselves with respect to the stress direction.

Macroscopically the creep rate of a glassy material is given by

$$\frac{d\varepsilon}{dt} = \frac{\sigma}{3\eta} \tag{5.40}$$

where η is the viscosity of the material. Combining eq.(5.39) and eq.(5.40) gives

$$\eta = \frac{N}{3Q_0\lambda'} \frac{1}{N_b} \tag{5.41}$$

which is a microscopical description of the viscosity. Eq.(5.41) together with eq.(5.36) and eq.(5.37) then describes the viscous behaviour of a glassy material.

5.2.2 Analytical discussion

5.2.2.1 Radiation induced compaction of glassy materials

Radiation induced compaction of glassy materal is described by eq.(5.38) with $\frac{dN_{g2}}{dt}$ determined by eq.(5.36) and eq.(5.37). Assuming that after some time of irradiation the number

of atoms located at broken state becomes constant, i.e. $\frac{dN_b}{dt} = 0$, then eq.(5.36) gives

$$N_b = \frac{(N - N_{g2})(K_{g1} + \nu_{g1} e^{-\Delta E_{g1}/k_B T_{irr}})}{\lambda' + K_{g1} + \nu_{g1} e^{-\Delta E_{g1}/k_B T_{irr}}} \tag{5.42}$$

where the g2-type glass state related part is ommited by assuming that g2-type bondings are stronger compared to a g1-type bondings, i.e. $\Delta E_{g2} \gg \Delta E_{g1}$ and $K_{g2} \ll K_{g1}$.

Eq.(5.42), eq.(5.37) and eq.(5.38) together give

$$\frac{d\varepsilon_c}{dt} = \lambda' P_0 \Sigma_c (1 - \frac{\varepsilon_c}{\Sigma_c})(1 - \frac{N_t}{N}\frac{\varepsilon_c}{\Sigma_c}) \frac{K_{g1} + \nu_{g1} e^{-\Delta E_{g1}/k_B T_{irr}}}{\lambda' + K_{g1} + \nu_{g1} e^{-\Delta E_{g1}/k_B T_{irr}}} \tag{5.43}$$

which can be integrated to yield

$$\varepsilon_c = \Sigma_c \frac{1 - e^{-Ut}}{1 - \frac{N_t}{N} e^{-Ut}} \tag{5.44}$$

where $U = \lambda' P_0 \frac{N - N_t}{N} \frac{K_{g1} + \nu_{g1} e^{-\Delta E_{g1}/k_B T_{irr}}}{\lambda' + K_{g1} + \nu_{g1} e^{-\Delta E_{g1}/k_B T_{irr}}}$. By fitting the experimental measured $\varepsilon_c \sim \phi t$ curve with eq.(5.44), the parameters P_0 and λ' could be determined.

The compaction rate just after beginning of the irradiation is given by

$$\frac{d\varepsilon_c}{dt}|_{t=0} = \lambda' P_0 \Sigma_c \frac{K_{g1} + \nu_{g1} e^{-\Delta E_{g1}/k_B T_{irr}}}{\lambda' + K_{g1} + \nu_{g1} e^{-\Delta E_{g1}/k_B T_{irr}}} \tag{5.45}$$

At low temperatures, i.e. $K_{g1} \gg \nu_{g1} e^{-\Delta E_{g1}/k_B T_{irr}}$, eq.(5.45) becomes

$$\frac{d\varepsilon_c}{dt}|_{t=0} = \lambda' P_0 \Sigma_c \frac{K_{g1}}{\lambda' + K_{g1}} \tag{5.46}$$

If $\lambda' \gg K_{g1}$ holds, then $\frac{d\varepsilon_c}{dt}|_{t=0} = P_0 \Sigma_c K_{g1}$ while if $\lambda' \ll K_{g1}$, then $\frac{d\varepsilon_c}{dt}|_{t=0} = P_0 \Sigma_c \lambda'$. The former implies that if different irradiation particles have the same $\beta \frac{\Delta E}{\Delta x} \phi$, then also $\frac{d\varepsilon_c}{dt}|_{t=0}$ would be the same. The latter shows that at very high values of $\beta \frac{\Delta E}{\Delta x} \phi$, the initial slope of the ε_c vs t curve reaches a maximum value which does not depend on dose rate.

In the case of high temperatures where $K_{g1} \ll \nu_{g1} e^{-\Delta E_{g1}/k_B T_{irr}}$ holds, eq.(5.45) gives

$$\frac{d\varepsilon_c}{dt}|_{t=0} = \lambda' P_0 \Sigma_c \frac{\nu_{g1} e^{-\Delta E_{g1}/k_B T_{irr}}}{\lambda' + \nu_{g1} e^{-\Delta E_{g1}/k_B T_{irr}}} \tag{5.47}$$

which describes the thermally induced compaction of glassy materials.

5.2.2.2 Radiation induced viscous flow in glassy materials

Consider the case that the material has saturated in compaction, i.e. $\frac{dN_{g2}}{dt} = 0$ or $N_{g2} = N_t$. Then inserting N_b from eq.(5.42) into eq.(5.41) gives:

$$\eta = \frac{1}{3 Q_0 \lambda'} \frac{N}{N - N_t} \frac{\lambda' + K_{g1} + \nu_{g1} e^{-\Delta E_{g1}/k_B T_{irr}}}{K_{g1} + \nu_{g1} e^{-\Delta E_{g1}/k_B T_{irr}}} \tag{5.48}$$

For the case of low temperature irradiation($K_{g1} \gg \nu_{g1} e^{-\Delta E_{g1}/k_B T_{irr}}$) and $\lambda' > K_{g1}$, eq.(5.48) becomes

$$\eta = \frac{1}{3Q_0} \frac{N}{N - N_t} \frac{1}{K_{g1}} = \frac{1}{3Q_0} \frac{N}{N - N_t} \frac{\Delta E_{g1}}{\beta \frac{\Delta E}{\Delta x} \Omega_{g1} \phi} \tag{5.49}$$

which shows that the viscosity is inversely proportional to dose rate and is independent of temperature (supposing N_t has only a weak temperature dependence). Furthermore, eq.(5.49) implies that if the energy consumed in breaking of the bonds inside the material per unit time and unit volume($\beta \frac{\Delta E}{\Delta x} \phi$) is the same for different irradiations, then the viscosity under irradiation would be the same.

In the case of high temperature irradiations, eq.(5.48) gives (assuming $\lambda' > \nu_{g1} e^{-\Delta E_{g1}/k_B T_{irr}}$):

$$\eta = \frac{1}{3Q_0} \frac{N}{N - N_t} \frac{1}{\nu_{g1} e^{-\Delta E_{g1}/k_B T_{irr}}} \tag{5.50}$$

which shows that at high irradiation temperatures the viscosity is totally governed by the thermally activated process with an activation energy of ΔE_{g1}.

If in eq.(5.48) $\lambda' \ll K_{g1} + \nu_{g1} e^{-\Delta E_{g1}/k_B T_{irr}}$ holds, then

$$\eta = \frac{1}{3Q_0 \lambda'} \frac{N}{N - N_t}. \tag{5.51}$$

This is the minimum achievable viscosity of the material through irradiation or heating(provided the glass is not melted).

Although the present model shows qualitative consistence with the observed radiation induced compaction and viscous flow in glassy materials(see section 6.2), its application is expected to be very limited because:

(a) Considering two distinct glassy states (reflected by two sharp bond energy levels E_{g1} and E_{g2}) is certainly an oversimplification of the real situation which is characterized by a broad spectrum of bond energies.

(b) Although the model is so simple, it involves many parameters which are not known. A full quantitative comparison with the present results is thus not possible.

Chapter 6

Discussion

6.1 Ceramic materials

6.1.1 Al_2O_3

Due to their independence of stress, the uniaxial strains ϵ of Al_2O_3 ceramics(Fig.4.1) are attributed to isotropic swelling. Therefore 3ϵ is compared in Fig.6.1 to previous experimental results on volume changes derived from macroscopic or lattice parameter (short dashed lines) measurements. As for most of the reactor data no specific displacement doses are given, the σ_d values for fast reactors from Table 4.1 are used. As shown in Fig.6.1, the present proton data at 235°C agree very well with the neutron data in the corresponding dose range where the 2/3 power law dose dependence is obeyed. As a whole, the data in Fig.6.1 could be divided into 4 parts which correspond to 4 damage periods. At very low dose($<5\times10^{-4}$ dpa) the volume change depends linearly upon the dose which indicates the accumulation of single point defects or small defect clusters. After loops are nucleated and become the dominating sinks, the dose dependence of the volume change follows a 2/3 power law as predicted(section 5.1). Further irradiation results in the intersection of loops and therefore the formation of dislocation networks. This is signalized by the lattice parameter measurements(short dashed lines) which give volume changes falling behind the macroscopic measurements at a dose of about 0.2 dpa. The reason for this is that the point defect absorption by network dislocations does not change the strain field in the matrix and thus cannot be detected by X-ray diffraction methods. Dislocations are thereafter the dominating sinks which give a 1/2 power law dose dependence of radiation induced strain. At very high dose the volume increase will stop as the vacancy concentration reaches the maximum value($1/v_s$). Extrapolation of the data in Fig.6.1 gives a saturation volume change around 3% and therefore a recombination

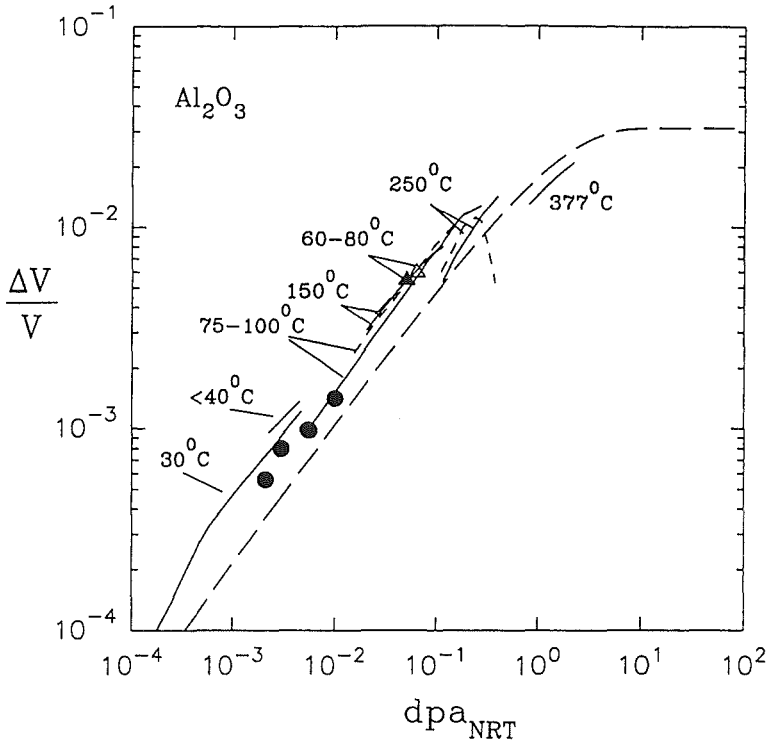

Figure 6.1: Swelling of Al_2O_3 ceramics derived from length change under 10.7 MeV proton irradiation at 235°C (•). Included are data from reactor irradiations at 30°C [77], ≤40°C [78], 75-100°C [79], 150°C [80], 60-80°C [81], 250°C [82] and 377°C [83]. The open symbol and short dashed lines give lattice parameter measurements. The long dashed line gives the result of numerical calculations using the procedure described in section 5.1.2.

volume(v_s) of about 30 atomic volumes.

Although the radiation damage evolution in Al_2O_3 in the intermediate temperature range could be very well described by the model given in section 5.1, no loops are detected by TEM at the present maximum proton dose. The reason for this could be that the loops are too small. Loops have been observed under electron irradiation at 327°C [25], Ar^+-irradiation at 260°C [84] and neutron irradiation at 157°C [85]. The vacancies are not mobile at the present lower temperature as it is found that oxygen vacancies anneal or agglomerate at temperatures above 327°C [86] while the aluminium vacancies begin to migrate at about 657°C [87]. Numerical calculations are performed to fit the data in Fig.6.1 by using ρ_d=$10^{12}/m^2$, v_s=30(Ω), volume dilatation V_F'=1 and loop density C_L=$5\times10^{22}/m^3$ [25]. The results of the calculations are compared to the data in Fig.6.1 (long dashed line) with good qualitative agreement. The horizontal shift between calculation and measurement is possibly due to a difference in

dpa calculations. Fitting of the data directly by appling the model described in section 5.1.1 gives a volume dilatation V_F' of about three atomic volumes and a interstitial loop density of about 100 times higher than observed.

Straining of the sapphire single crystal(Fig.4.4) is different from that of Al_2O_3 ceramics in that the linear dose dependence behaviour continues up to 7×10^{-3} dpa and the corresponding strain is lower. This could be explained by delayed loop nucleation in the single crystalline material. Above 0.02 dpa the strain of sapphire approaches that of the ceramics and follows the same dose dependence which is consistent with neutron observation that at high dose there is no significant difference in straining between single and polycrystals [85].

6.1.2 SiC

As the radiation induced straining in SiC (Fig.4.2) shows no stress dependence, the present proton data are attributed to swelling and compared to the neutron data in Fig.6.2 which shows reasonable agreements. Quantitatively the strain of SiC is different from that of Al_2O_3 in that it is almost one order of magnitude higher and shows stronger tendency to

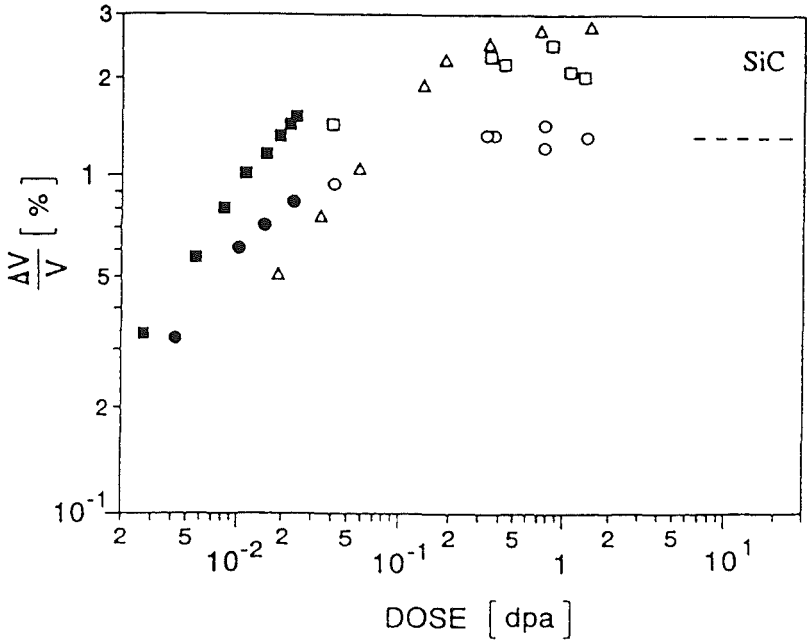

Figure 6.2: Dimensional changes of SiC specimens under 10.7 MeV proton irradiation at 265°C(■) and 505 °C(•), and of specimens under neutron irradiation at 200°C(△) [88], 250°C(□), 475°C(o) [89] and 500°C(- - -) [88].

saturation(see Fig.6.2). A compilation of saturation volume under neutron irradiation as a function of temperature is given in Fig.6.3 [90, 91]. It shows that with increasing temperature the saturation value of the volume change decreases gradually from room temperature up to ~800°C. This behaviour can not be described by an increase of vacancy mobility with temperature as stated in section 5.1.3 by eq.(5.25). Instead, the reason is probably an increase in recombination volume with temperature. This proposition is warranted by the fact that annealing of defects always happens above about the irradiation temperature as has been found in measurements of electrical resistivity [92], thermal conductivity, thermal diffusivity and strain [89] of specimens irradiated by neutrons at various temperatures. Void formation occurs only at very high temperatures(>1250°C) [93] while loops are observed only at very high dose [94, 95] which could be attributed to the collapse of high concentrations of point defects or to cascade damage. It is therefore concluded that point defects in SiC are not mobile even at temperatures as high as ~800°C. This is not surprising when the strong covalent structure of the material is considered. Recently a molecular dynamical calculation has shown that for this material the migration energy of interstitial(Si) could be as high as 6 eV [96].

The point defect accumulation of SiC under the present proton irradiation is therefore described by equation(2.11) [31] although the irradiation temperatures are far above room temperature. Integration of eq.(2.11) yields:

$$C = \frac{\sigma_d \phi t}{1 + v_s \sigma_d \phi t} \tag{6.1}$$

which is used together with eq.(2.9) to fit the length measurements. The fitting gives V_F=1.37 and v_s=48 at 265°C and V_F=0.95 and v_s=64 at 505°C, respectively, (dashed lines in Fig.4.2). The extrapolated saturation values

$$(\frac{\Delta V}{V})_\infty = \frac{V_F}{v_s} \tag{6.2}$$

are in good agreement with the results from neutron experiments compilied in Refs. [90, 91](Fig.6.3). Transforming saturation volume change into recombination volume by eq.(6.2) using V_F=1 gives the temperature dependence of recombination volume as shown in Fig.6.4. This figure could be used to explain the implantation induced amorphization of SiC. It is found that the material is amorphized by implantation of Cr^+ and N^+ to 0.2–0.3 dpa at room temperature but not by implantation at 450°C to 16 dpa [97]. According to the above temperature behaviour of recombination volume one could imagine that for amorphizing a material a maximum defect concentration should be reached which means that the recombination volume should be smaller than a critical value(v_a). This is schematically shown

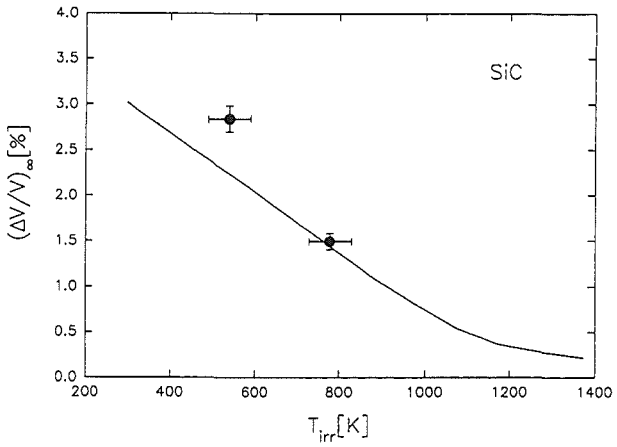

Figure 6.3: Saturation values of volume expansion of SiC as a function of temperature after proton irradiation(•). The straight line represents compilations of reactor data in Refs. [90, 91].

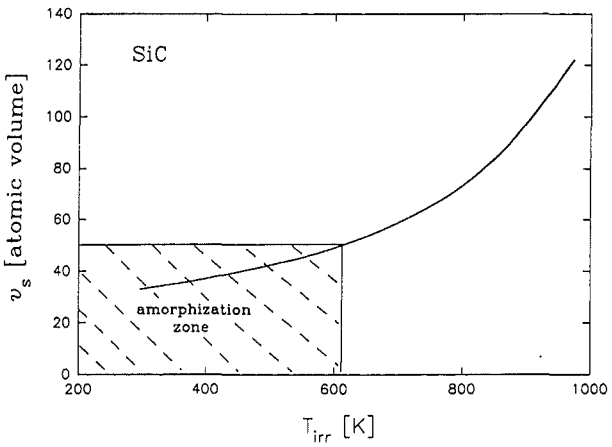

Figure 6.4: Recombination volume of SiC as a function of temperature derived from reactor data in Refs. [90, 91].

in Fig.6.4 by taking $v_a \approx$50 atomic volumes. Above the critical value, i.e., above a certain temperature, amorphization will never happen no matter how high the dose is. The small recombination volume($\sim$30 atomic volumes) at low temperature is consistent with the MD calculation [98] which shows that along certain lattice directions Frenkel pairs are already stable at distances of one lattice constant.

6.1.3 AlN and Si_3N_4

The present results for AlN are in reasonable agreement with neutron data [99–101] when compared for similar temperatures(Fig.6.5). For Si_3N_4 no neutron data are available at the present low irradiation temperature. Limited microstructural investigations show that interstitial loops are the only detectable defects under TEM in neutron irradiated AlN at 470°C [102]. The 2/3 power law dose dependence of strain of the proton irradiated materials indicates that loops are the dominating sinks even at the present low irradiation temperature. Due to the lack of detailed information on radiation induced microstructure, no numerical calculations are performed.

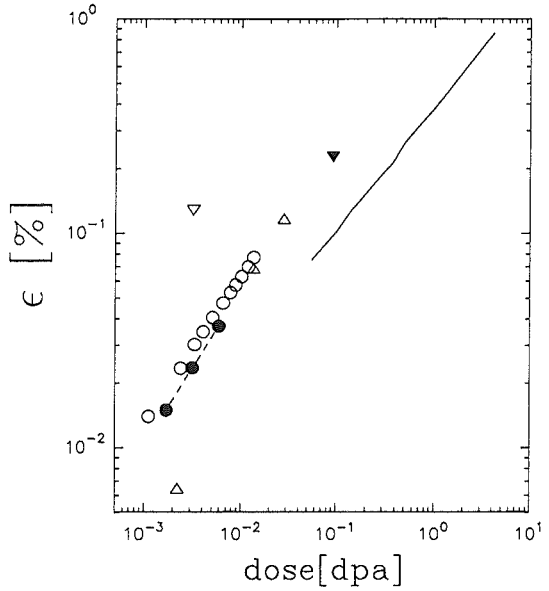

Figure 6.5: Macroscopical strains of AlN under proton irradiation at 230°C(o) and 420°C(•). Included are results from neutron irradiation at 100°C(▽), 470°C(▼) [100] and 400–550°C (—) [99]. The △ data are from lattice parameter measurements under neutron irradiation at <600°C([101]).

6.1.4 Single crystalline MgO

MgO under irradiation shows loops even at temperatures as low as room temperature [25] whereas the oxygen vacancy migration energy is around 2 eV [25]. Therefore the 2/3 power law dose dependence of strain under present proton irradiation is understandable. Similar to Al_2O_3, the stress independent strains of MgO for stresses below 40 MPa are in reasonable agreement with neutron data(Fig.6.6). The decrease of strain derived from lattice parameter measurement [104](dashed line) above about 0.04 dpa indicates that the defect accumulation with further irradiation is dislocation dominated. The strain of $\sim$ 1% after high dose irradiation [85] would mean that the recombination volume of the material is around 30 atomic volumes. Taking this information as well as the experimantal measured loop volume density of 5×10^{22} $(1/m^3)$ into account, the numerical calculation (assuming $V_F' \approx 1$) is applied to the data in Fig.6.6. Like for Al_2O_3 the fit(solid line) shows qualitative agreements.

The stress effect on radiation induced strain in MgO(Fig.4.5) starts to be significant at stresses above 40 MPa. As considering the 2/3 power law dose dependence of strain with and without stress enhancement, the damage process is believed to be the accumulation of single vacancies and the formation of interstitial loops. It is at present not clear whether

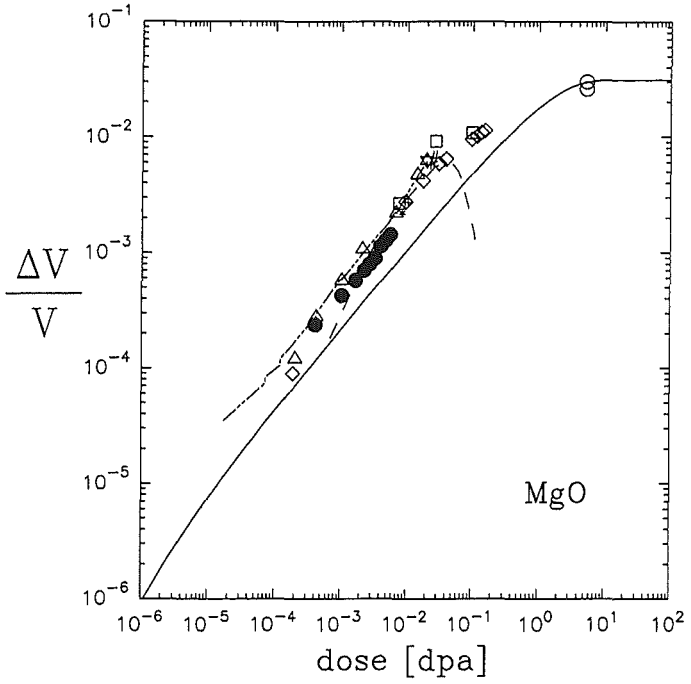

Figure 6.6: Strain of MgO under proton irradiation at 220°C (•). Included are results from neutron irradiaton at ~40°C(△,–···–···–) [103], ≤80°C(▽, ♯) [81], 75–100°(◇, – –) [104], <150°C(□) [105], 157°C(○) [85], <200°C(+) [106], and (∗) cited in [104]. The symbols +, ∗, ♯ and various dashed lines give lattice parameter measurements. The solid line gives results of numerical calculations.

stress only influences loop morphology, i.e. loop size, loop density and loop orientation, or whether it causes other processes like climb and glide of dislocation. Further work is required to determine the underlying mechanisms.

6.1.5 Polycrystalline $MgAl_2O_4$

The radiation induced microstructure in spinel shows a complex behaviour. It is found that 1 MeV electron irradiation [25] can not produce loops whereas heavy ion irradiation can induce loops even at room temperature with loop size and density varying very little with temperature from 25°C to 650°C [107]. Irradiation by heavy ions and subsequently electrons shows that the loops produced by heavy ions diminish gradually with electron dose [25]. This process is very efficient at lower electron energies. The phenomenon is attributed to the enhanced migration of structural vacancies under electron irradiation which mainly produces ionization. It is therefore concluded that for producing loops in spinel the ratio of ionizing to displacive damage should be below a certain value. Quantitative studies show

that the amount of radiation induced interstitials retained in loops is very small(around 10^{-4}) compared to other materials [107, 108]. This is consistent with the smaller changes in dimension and thermal diffusivity induced by irradiation [107, 108]. The significant smaller changes under irradiation compared to other materials is believed to be due to the high structural vacancy concentration and/or the lower probability of introducing stable defect clusters into the material [109].

In Fig.6.7 the present proton data are compared to neutron [85] and heavy ion [110] data. Swelling under Ar^+-irradiation seems to start only above 1 dpa while only one neutron data is avaiable at about 5 dpa. The Ar^+ and neutron data reach strains of 0.25% which mean that the concentration of vacancy reaches 0.8% by the high dose irradiation. This value is much high than that induced by the present proton irradiation which shows clear saturation in strain around 0.035%. It is at present not clear whether it is a stress effect or due to differences in material and/or irradiation particles. One possibility would be that the high dose irradiation changes the atomic arrangement of the material greatly which makes further production of point defects possible whereas the present low dose proton irradiation can only reach the maximum attainable defect concentration determined by the available material microstructure.

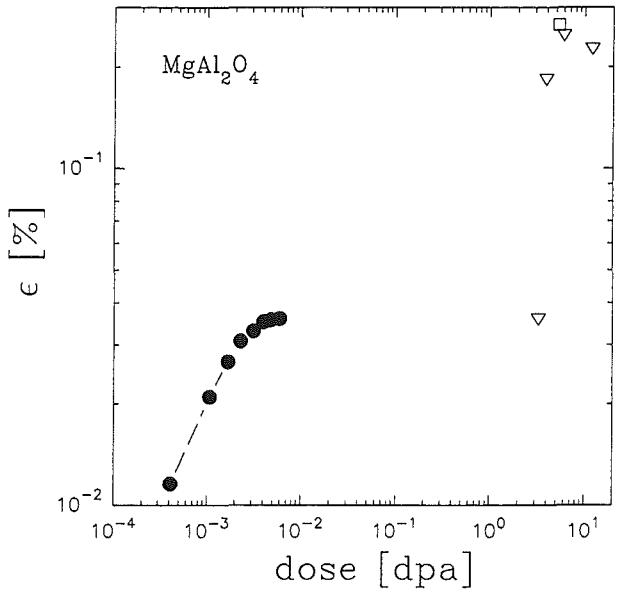

Figure 6.7: Strain of $MgAl_2O_4$ under proton irradiation at 220°C (•) at 40 MPa. Included are results from Ar^+ irradiation at 262°C (▽) [110] and neutron irradiation at 157°C (□) [85].

6.1.6 Single crystalline Si

The point defects (interstitials and vacancies) in Si are expected to be mobile at the lowest irradiation temperature used. The measured creep rates ($\sim 5\times10^{-11}$dpa^{-1}Pa^{-1}, see Figs.4.6 and 4.7) are similar to that of proton irradiated austenitic stainless steels at temperatures around 300°C [111]. A phenomenon where irradiation induced plastic deformation of silicon may play a role is the formation of blisters which for example is observed during room temperature implantation of monoenergetic Ne^+ or Ar^+ ions [112] to doses of about 100 dpa. The blisters have diameters up to 36μm and the covers are bulging by up to 5μm without fracturing, which indicates plastic deformation in the order of 5%.

6.2 Crystalline and vitreous SiO_2

The basic building block of both crystalline [113] and vitreous [114] SiO_2 is the slightly distorted SiO_4 tetrahedra which shares each of its corners with other tetrahedra(Fig.6.8). The bonding distance between an oxygen and a silicon atom is around 1.61Å and the O–Si–O angle ψ is about 109.5°. Whereas in crystalline SiO_2 the Si–O–Si angle θ is fixed at 143.65°, the Si–O–Si angle in vitreous SiO_2 shows a spread from 120° to 180°, but still the most probable angle is around 144° as determined from X-ray scattering(see [115] and the Refs. therein). As stated by Zachariasen in 1932 [116], just this broad statistical distribution of Si–O–Si angles is the primary source of noncrystallinity of the material. It is still not clear whether vitreous SiO_2 can be considered as consisting of randomly oriented microcrystals, as proposed 74 years ago [117]. Under irradiation oxygen vacancies are produced in both crystalline and vitreous SiO_2. This is demonstrated through various techniques such as ESR and optical absorption as the oxygen vacancy is a precursor or a constitutent of various centres(see Table 2.1). In crystalline SiO_2 it is found that the threshold energy for producing an oxygen vacancy decreases gradually with increasing irradiation dose from 24.7 eV to 1 eV because of amorphization [118]. This is consistent with the observation that in vitreous SiO_2 both ionization and nuclear displacement can induce defects(see section 2.2.1). Dimensional measurements show that under irradiation crystalline SiO_2 expands whereas vitreous SiO_2 contracts (Fig.6.9), but the assymptotic density of both heavily irradiated materials is similar. For crystalline SiO_2 it is found that the expansion proceeds in three stages [53, 55]. Below 4×10^{23}n/m^2 the material deforms very slowly whereas above this dose it expands rapidly, until around $\sim1.2\times10^{24}$n/m^2 swelling slows down and eventually reaches the final state. Annealing of the radiation induced expansion after irradiation to different doses is

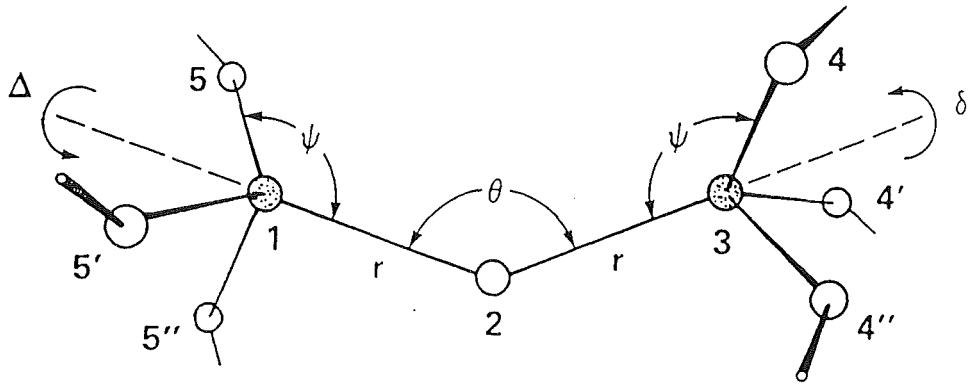

Figure 6.8: The relative orientation of two corner sharing tetrahedra in SiO_2. The Si atom(dark) are surrounded tetrahedrally at distance r by four O atoms(open circle) and each O atom bridges between two Si atoms with an angle θ. The O–Si–O angle is marked as ψ.

also different [52]. For SiO_2 glass, the density of oxygen vacancy induced by ionization alone follows roughly a 2/3 power law dose dependence [114] which is exactly the same as that of ionization induced compaction [50]. Nevertheless compaction cannot be ascribed to vacancy formation, as the radiation induced concentration of oxygen vacancies saturates much earlier than the radiation induced densification. Furthermore the amount of oxygen vacancies after saturation cannot explain the measured saturation density change of ~3% [114].

Concerning the ambiguities stated above, the model described in section 5.2 could give some reasonable explanations. As shown in Fig.5.2 the production of oxygen vacancies(here corresponding to the breaking of bonds) is the prerequsite for the formation of g2-type bonds which is responsible for the radiation induced compaction. Therefore saturation of the production of oxygen vacancies does not mean saturation in compaction. The new atomic bonds formed are not necessarily the same as that in crystalline material, but certainly give a denser atomic arrangement than the original glass. Although the optical absorption measurements(Fig.4.16–4.20) give abundant information about the various radiation induced centres, especially E_1' centre(Fig.4.20), it is however at present not possible to connect quantitatively the radiation induced centres with radiation induced compaction. The radiation induced viscosity is inversely proportional to the number of broken bonds as stated in

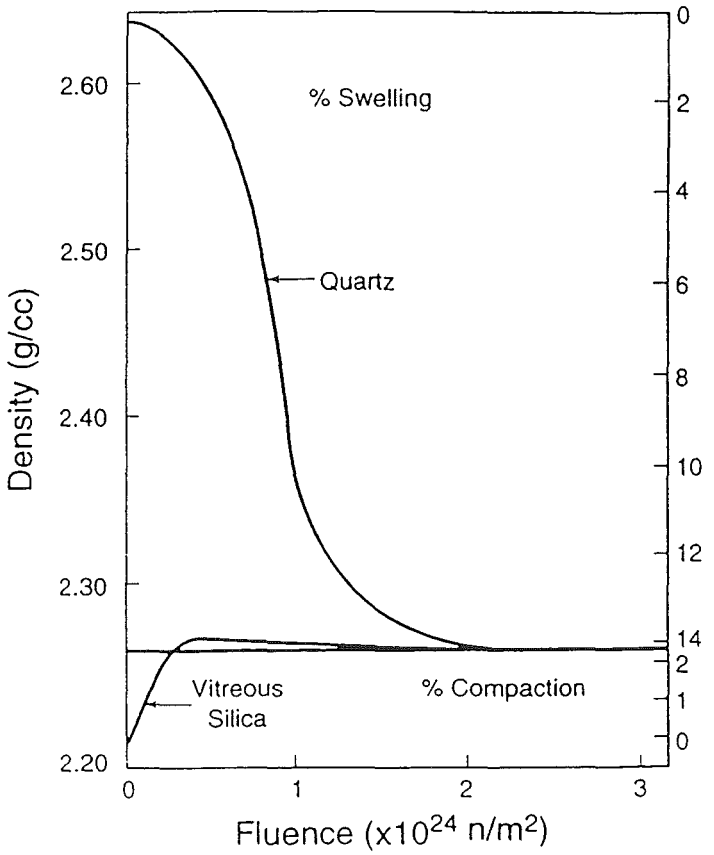

Figure 6.9: Density change of quartz and vitreous silica under neutron irradiation(from Lell et al, [46]).

eq.(5.41), but as the amount of E_1' centres does not represent the total number of oxygen vacancies and as the number of oxygen vacancies is not just the total number of broken bonds, a quantitative discussion is not possible.

Radiation damage in crystalline SiO_2 follows just the opposite process of that in SiO_2 glass described by the model in section 5.2.1. At the beginning mainly point defects and small defect clusters are formed which cause the material to expand just like the other crystalline materials. When there are enough defects accumulated, i.e. when there are enough broken bonds available, rearrangement of bonds becomes possible. This situation corresponds to the formation of small zones which have glass structure. Large deformation will happen during this time as the material undergoes structural transformation. Finally the system will reach a stationary state (i.e. totally glassy) and the expansion ceases. It is understandable that due to the difference in radiation induced microstructure the annealing of macroscopic

properties such as density etc differs with dose. Experimental observations [118–120] support the above explanations. It is found that electron irradiation of quartz crystals [119] at room temperature initially induces black spots which increase in size and density with dose until they become dislocation loops. Additional irradiation results in amorphization. In ion-implanted quartz crystals [118] three characteristic stages of defect formation are found in dependence on deposited energy G_n through nuclear processes: (I) at $G_n \leq 10^{20}$keV/cm^3 point defects are produced, (II)at $G_n \approx 2.5 \times 10^{20}$keV/cm^3 amorphous microregions are generated and (III) at higher energy deposition drastic structural and physical property changes occur. In the same work it is noticed that disorder formation due to electronic processes is possible, but only in predamaged quartz and only with low efficiency. This emphasizes that for the formation of glassy zones inside the crystalline SiO_2 enough broken bonds must be available. The present proton irradiation of crystalline SiO_2 is in the low dose range and the defect production is mainly through nuclear displacement. Therefore the deformation observed(Fig.4.8) is mainly from point defect accumulation. Stress has no influence on the radiation induced deformation which is consistent with the damage mechanism. As long as the material is crystalline in structure, the breaking of bonds as well as re-bonding (corresponding to the production of interstitial and vacancy pairs and the recombination of interstitial and vacancy, respectively) is very difficult. According to the model this means that N_b is too small and therefore no viscous flow is observed. But if there are enough glassy zones formed which make the breaking and re-bonding of bonds easier, viscous flow under irradiation will happen just like in a glassy material.

6.3 Polycrystalline tungsten

Scarce information from the supplier indicates that the tungsten foils used in present study are "hot worked". Therefore some point defects as well as defect clusters may be present from production. As shown in Fig.4.27 large clusters around 20 nm in diameter are observable under TEM. Some of the clusters anneal during heating of the specimens(Fig.4.27) when point defects become mobile at high temperatures. The diminishing of point defects and defect clusters is therefore the reason of a small reduction in resistivity(Fig.4.25). Furthermore, mobile point defects may interact with dislocations which allows the high strain energy induced by "hot working" to be released. This process accompanies a deformation of the material, which is certainly stress dependent(Fig.4.21 to Fig.4.23). Under irradiation the radiation induced defects cause extra changes in strain and resistivity. Swelling and creep are expected to contribute to the measured strain under irradiation, but their magnitude is

not large enough to explain the measured strain. Fig.4.21 to Fig.4.24 show that the strains under irradiation show saturation at very low dose values and one measurement at 320°C under low stress shows even contraction after a short time irradiation(Fig.4.22). It is therefore believed that other processes such as precipitation also occur which lead to negative strains.

The resistivity changes induced by proton irradiation at 160°C and neutron irradiations at 70°C and 100°C [73, 74] agree very well on the basis of displacement dose(Fig.4.26). These irradiation temperatures are below the so called stage III which is the temperature range where monovacancies become mobile. Therefore the irradiations are in the intermediate temperature range where interstitials form loops or are absorbed by dislocations while vacancies accumulate as point defects. If the resistivity contribution per unit concentration of vacancies(point defect) and interstitials(trapped in loops or in dislocations) is known(denominated as ρ_F), the radiation induced resistivity change $\Delta\rho$ can be evaluated by the way similar to that used in calculation of radiation induced swelling(c.f. section 2.1.2) which gives an approximate expression as follows:

$$\Delta\rho = (C_v - C_{v0}) \cdot \rho_F. \tag{6.3}$$

Here again the change in resistivity is simply related to the concentration of radiation induced vacancies. As the materials used in neutron irradiations are well annealed, the interstitials are mainly retained in loops. This gives a resistivity change of $\sim$0.7 power law dose dependence(see eq.5.21). The present proton irradiated material has high dislocation density and therefore the resistivity change follows the $\sim$0.5 power law dose dependence(see eq.(5.17)).

Chapter 7

Summary

Ceramic materials including Al_2O_3, SiC, AlN, Si_3N_4, MgO, $MgAl_2O_4$, Si and SiO_2 as well as refractory tungsten are irradiated with protons in the 10 MeV range at temperatures from 75°C to 630°C under uniaxial tensile stresses from 6 to 330 MPa to dose levels up to about 0.1 dpa. Changes in length and resistivity are monitored after each irradiation or during beam-off periods. TEM or optical absorption technique is applied to extract information of the radiation induced microstructure changes. For materials with crystalline structure modified rate equations are used to discuss the measurements whereas for SiO_2 glass a two–type bond model is developed to describe the radiation induced deformation and viscous flow. Following is a list of the main experimental results:

- Straining of Al_2O_3 shows a less than linear dose dependence, a slight decrease with increasing temperature and negligible stress dependence up to about 100 MPa. Specimens show no detectable features under TEM at the maximum dose.

- SiC deforms significantly under proton irradiation with strain showing strong tendence to saturation. No stress effects are observed up to the maximum applied stress($\sim$100MPa). Microscopical changes can not be revealed by TEM.

- AlN and Si_3N_4 deform under irradiation with strain following roughly a 2/3 power law dose dependence. An increase in temperature reduces slightly the radiation induced strain in AlN.

- Radiation induced strain in single crystalline MgO is strongly enhanced at stresses above about 50 MPa, but the strain still follows a 2/3 power law dose dependence just like that without stress enhancement. Large amount of loops are formed under the irradiation.

- Straining in polycrystalline spinel shows saturation around 10^{-2} dpa at a very small value. Loops are mainly seen along grain boundaries.

- Irradiation of silicon single crystals below 600°C shows creep in the order of $\sim 5 \times 10^{-11} \mathrm{dpa}^{-1} \mathrm{Pa}^{-1}$, similar to that of proton irradiated austenitic stainless steels at temperatures around 300°C.

- Strain in crystalline SiO_2 shows less than linear dose dependence, a slight decrease with increasing temperature and negligible stress dependence for stresses up to ~40 MPa.

- SiO_2 glass under proton irradiation compacts initially and then elongates along the stress direction. The strain rate is linear in stress and dose rate, but shows no temperature dependence in the temperature range from 220–600°C.

- Radiation induced strains in tungsten show both temperature and stress dependence whereas the corresponding resistivity changes show only temperature dependence. At low doses the resistivity change induced by irradiation below stage III follows a 1/2 power law dose dependence. Loops and dislocations are induced by the irradiation.

The experimental results are compared to previous measurements under neutron irradiation and fitted to theoretical models to uncover the underlying mechanisms. The following conclusions can be extracted from the analysis:

- Crystalline materials irradiated in the intermediate temperature range (i.e. where interstitials migrate and vacancies are immobile) deform in four different stages. At very low dose where mainly point defects or small defect clusters are formed, the strain is linear in dose. After loops finishing nucleation and becoming the dominating sinks, the strain follows a 2/3 power law dose dependence. The growth and intersection of loops results in the formation of dislocation networks which changes strain to a 1/2 dose dependence. Finally saturation in strain occurs at very high doses where the vacancy concentration is high enough so that the spontaneous recombination becomes dominating.

- Large amount of evidence shows that at temperatures below about 800°C point defects(interstitials and vacancies) in SiC are not mobile. Therefore radiation induced strain is due to the accumulation of point defects. From the temperature dependence of the saturation volume change it is concluded that the recombination volume of defects in SiC increases with increasing temperature.

- Although thermal spike effects may contribute to the radiation induced viscous flow, they are not sufficient to explain the viscous behaviour of v-SiO_2 during 9.2 MeV proton irradiation. Electronic processes are thus expected to supply the main contribution to the enhanced viscous flow. This could be described by processes of breaking of bonds and re-bonding during irradiation. New bond formation results in compaction while the rearrangements of atoms with respect to the direction of external stress during re-bonding causes viscous flow.

As a by–product of the present measurements it could be shown that the radiation induced electrical degradation of Al_2O_3 (the so-called RIED effect) is probably not a bulk phenomenon but caused by leakage currents flowing in surface layers whose deposition under irradiation is enhanced by an electric field (see Appendix).

Zusammenfassung

Die keramischen Werkstoffe Al_2O_3, SiC, AlN, Si_3N_4, MgO, $MgAl_2O_4$, Silizium, SiO_2(im kristallinen und glasigem Zustand) und das hochschmelzende Metall Wolfram wurden mit Protonen im 10 MeV Energiebereich bei verschiedenen Temperaturen (75 bis 630°C) und Zugspannungen (6 bis 330 MPa) zu Dosen bis zu 0.1 dpa bestrahlt. Änderungen in der Länge und im elektrischen Widerstand der Proben wurden nach jeder Bestrahlung oder in Bestrahlungspausen gemessen. Änderungen der Mikrostruktur wurden durch TEM oder optische Absorptionsspektroskopie verfolgt. Die experimentellen Resultate lassen sich wie folgt zusammenfassen:

- Die bestrahlungsinduzierte Dehnung in Al_2O_3 zeigt eine schwächer als lineare Dosisabhängigheit, verringert sich leicht mit zunehmender Temperatur und die Spannungsabhängigkeit bis 100 MPa ist vernachlässigbar klein. Im TEM konnten keine mikrostrukturellen Änderungen aufgelöst werden.

- SiC verformt sich stark unter Bestrahlung, die Dehnung sättigt aber bald. Auch hier konnten keine Spannungsabhängigkeit bis zur maximal angelegten Spannung von 100 MPa und keine Mikrostrukturänderung im TEM nachgewiesen werden.

- Die Dehnungen in AlN und Si_3N_4 nehmen nach einem 2/3–Potenzgesetz mit der Dosis zu und nehmen in AlN mit zunehmender Temperatur leicht ab.

- In einkristallinem MgO nimmt die Dehnung ebenfalls mit der 2/3–Potenz der Dosis zu. Spannungen von 50 MPa erhöhen die Dehnungsrate stark, die Dosisabhängigkeit bleibt aber erhalten. Hier wurde eine hohe Dichte von bestrahlungsinduzierten Versetzungsringen im TEM festgestellt.

- Polykristalliner Spinell zeigt nur geringe Verformung unter Bestrahlung, und die Dehnung sättigt schon ab Dosen von 10^{-2} dpa bei sehr kleinen Werten. Hier wurden Versetzungsringe hauptsächlich entlang der Korngrenzen beobachtet.

- Bestrahlung von Si–Einkristallen unter Zugspannung zeigt schon unter 600°C Bestrahlungskriechen mit einer Komplianz von ca. $5\times10^{-11}\mathrm{dpa}^{-1}\mathrm{Pa}^{-1}$, ein Wert, wie er auch in austenitischen Edelstählen gemessen wurde.

- Die Dehnung in kristallinem SiO_2 zeigt eine schwächer als lineare Dosisabhängigkeit, verringert sich leicht mit zunehmender Bestrahlungstemperatur und die Spannungsabhängigkeit bis 40 MPa ist vernachlässigbar klein.

- SiO_2–Glas verdichtet sich bei Beginn der Bestrahlung und dehnt sich bei höheren Dosen in der Spannungsrichtung. Die Dehnungsrate ist proportional zur Spannung und zur Dosisrate und zeigt keine Temperaturabhängigkeit im Bereich von 220–600°C.

- Die bestrahlungsinduzierten Dehnungen in Wolfram sind sowohl temperatur–, als auch spannungsabhängig. Die entsprechenden Änderungen im elektrischen Widerstand sind nur temperaturabhängig. Unterhalb der Erholungsstufe III ist die Widerstandsänderung bei kleinen Dosen der Wurzel aus der Dosis proportional. Die Bestrahlung induziert Versetzungsringe und Veränderung im Versetzungsnetzwerk.

Die experimentellen Resultate der vorliegenden Protonenbestrahlungen wurden mit früheren Daten (wo vorhanden) von Neutronenbestrahlungen verglichen und mit theoretischen Modellen verglichen, um die zugrundelliegenden Mechanismen aufzudecken. Die wichtigsten Schlüsse aus dieser Analyse sind:

- Die Verformung von kristallinen Materialien, die im mittleren Temperaturbereich bestrahlt werden (d.h. wo Zwischengitteratome beweglich, Leerstellen aber unbeweglich sind) kann in 4 Dosisbereiche unterteilt werden: Bei sehr geringen Dosen, wo hauptsächlich einzelne Punktdefekte und kleine Defektcluster entstehen, nimmt die Dehnung linear mit der Dosis zu. Nach Beendigung der Keimbildung von Versetzungsringen werden diese die dominierenden Senken und die Dehnung folgt einem 2/3–Potenzgesetz mit der Dosis. Das Wachstum und die Durchdringung der Ringe führt zum Aufbau eines Versetzungsnetzwerkes und die Dosisabhängigkeit geht in ein 1/2–Potenzgesetz über. Schließlich sättigt die Dehnung bei hohen Dosen, wo die Leerstellenkonzentration so groß geworden ist, daß spontane Rekombinationen dominieren.

- Es gibt viele Hinweise, daß beide Arten von Punktdefekten (Leerstellen und Zwischengitteratome) in SiC bis zu Temperaturen von 800°C unbeweglich sind, d.h. die bestrahlungsinduzierte Dehnung wird durch die Ansammlung von einzelnen Punktedefekten verursacht. Die Sättigungsdehnung, bzw. –volumenzunahme nimmt mit zunehmender

Temperatur ab, woraus auf eine Zunahme des Rekombinationsvolumens der Defekte in SiC geschlossen werden kann.

- Obwohl thermische Spike–Effekte zum bestrahlungsinduzierten Fließen von SiO_2 Glas beitragen können, reicht ihre Größe nicht aus, um die stark verringerte Viskosität unter Bestrahlung zu erklären. Elektronische Prozesse müssen also den Hauptbeitrag liefern. Dies könnte durch das Aufbrechen und Wiederherstellen von Atombindungen erfolgen. Die Bildung neuer (engerer) Bindungen resultiert in der beobachteten Verdichtung des Glases unter Bestrahlung, während eine Ausrichtung der Atome in bezug auf die Richtung der angelegten Spannung ein erhöhtes viskoses Fließen bewirkt.

Als Nebenprodukt der durchgeführten elektrischen Leitfähigkeitsmessungen ergab sich, daß die bestrahlungsinduzierte permanente Erhöhung der Leitfähigkeit von Al_2O_3 (der sog. RIED–Effekt) wahrscheinlich kein Volumeneffekt ist, sondern durch Leckströme vorgetäuscht wird, die über Oberflächenschichten fließen und deren Deposition unter Bestrahlung durch ein elektrische Feld verstärkt wird (siehe Anhang).

Appendix

Electrical conductivity measurement of Al_2O_3 ceramics

The radiation induced electrical degradation(RIED) in ceramics materials was first reported in 1989 by E. R. Hodgson [121], who found that in e^--irradiated single crystalline Al_2O_3 with the coexistence of electrical field across the specimen thickness, the electrical conductivity of the material showed a permanent strong increase after some time of irradiation. This discovery stimulates great interest among scientists and, in not a long time the effect was repeated by some laboratories using different particles [122, 123]. As a response to this new discovery, we irradiated an Al_2O_3 ceramic specimen with 10.7 MeV protons at a temperature of about 800 K and a dose rate of about 8×10^{-8} dpa/s where the RIED effect was supposed to be maximal. During the irradiation an electrical field of about 320 kV/m is applied across the specimen thickness through the sputtered Pt films(cf. section 3.1). The application of a guard ring between the two electrodes, which is the normal way to cancel the contributions from the surface conductance, is not possible here due to the experimental constraints. Fig.A.1 shows the results of the conductance measurements under irradiation with and without the electrical field. It can be seen that with the coexistence of electrical field, the conductivity of the material is greatly increased after a dose of about 10^{-3} dpa. As no guard ring is used in the measurements, cleaning of the specimen edge sides, where the two electrodes are separated, would be necessary to make sure that the increase in conductivity is really a bulk effect. However, after cleaning the edges by scratching the conductance of the irradiated specimen recovered totally to the original value. This means that what we observed here is merely due to the contamination of the specimen surface, a result which is not so surprising to us. What is really surprising is that the group in England [122] observed the RIED effect under almost the same experimental conditions as we have, except that

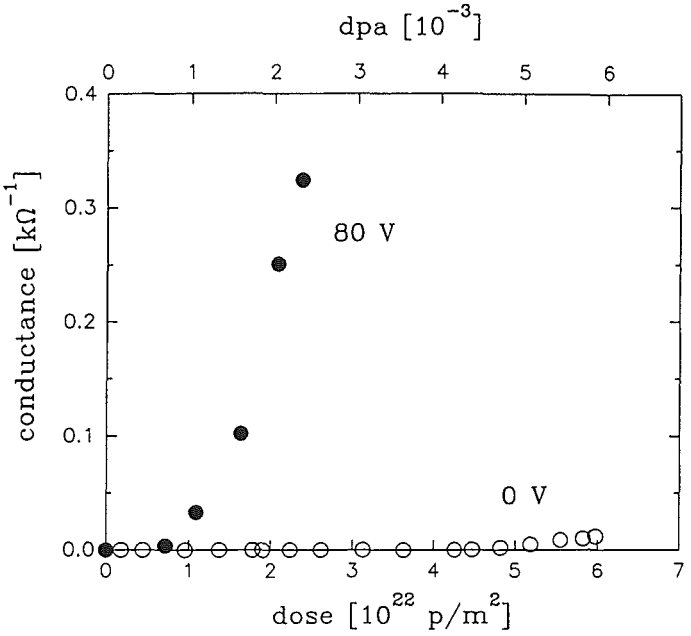

Figure A.1: Increase of electrical conductance of Al_2O_3 during irradiation with 10.7 MeV protons at 800 K with(•) and without(o) an electrical field of 320 kV/m.

they used a guard ring in the measurements. We therefore analyse the setup used in their resistance measurements.

Fig.A.2 shows a typical setup that uses a guard ring in measuring the resistivity of ceramic materials. If taking R_s as the specimen bulk resistance and R_a, R_b as the surface resistances while R as the resistance of the lead to guard ring including contacts(the other lead resistances are not included as it is found that they have no influence to the calculation), then the corresponding wiring diagram of the arrangement is sketched in Fig.A.3 from which the following equation for the apparent resistance $\frac{U}{I} = R_m$ can be derived:

$$\frac{1}{R_m} = \frac{1}{R_s} + \frac{1}{(R_a + R_b)(1 + \frac{R_a R_b}{R_a + R_b}\frac{1}{R})} \tag{A.1}$$

This equation implies that if the resistance of the lead to the guard ring (R) is zero, the measured apparent resistance would equal the specimen resistance. But actually this situation can not be reached in experiments, therefore the second term in eq.(A.1) will contribute to the apparent resistance. Fig.A.4 shows the apparent resistance $\frac{U}{I}$ as a function of surface resistance(here taking R_a=R_b and R=1 or 100 Ω) for various values of the bulk specimen resistance. As can be seen the measured apparent resistance will fall down if the surface

resistance becomes too low although there is no change in the bulk specimen resistance. It is therefore speculated that the RIED effect is very probabily due to contamination of specimen surfaces which is a process enhanced by the applied electrical field. The enhancement of surface contamination is demonstrated by thermal evaporation experiments of carbon onto sapphire [123] which show that the evaporation process is increased by an electrical field. F. Scheuermann and W. Kesternich [124] measured the conductivity changes of Al_2O_3 during 28 MeV α irradiation by using a guard ring arrangement. By changing the surface resistance R_a and/or R_b intentionally they found that the apparent resistance $R_m = \frac{U}{I}$ changes correspondingly. This demonstrates then directly that the RIED effect is due to surface contamination.

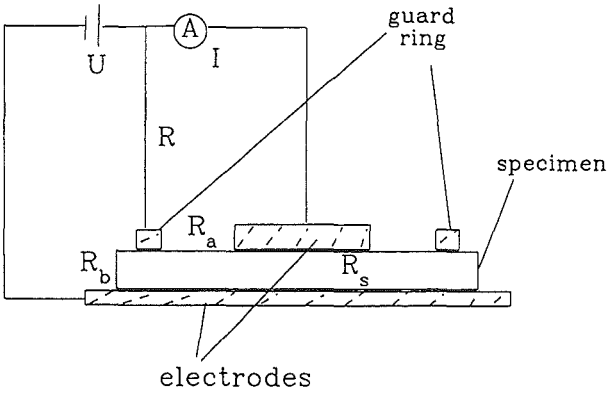

Figure A.2: Cross section of a typical setup of guard ring device for resistance measurements of insulate materials.

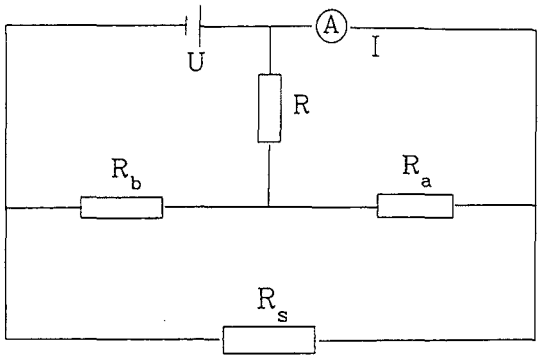

Figure A.3: Wiring diagram of the guard ring device for resistance measurements of insulate materials.

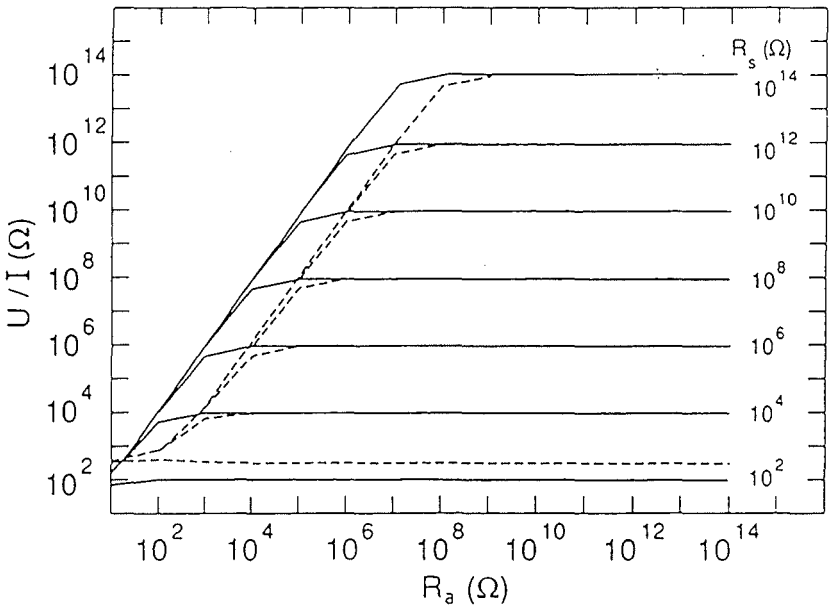

Figure A.4: Calculated apparent resistance U/I as a function of surface resistance R_a for various bulk specimen resistances R_s. Solid and dashed lines indicate calculations for resistances R of the lead to guard ring of 1 and 100 Ω, respectively.

References

[1] M. Kiritani, J. Nucl. Mater. **216** (1994) 220

[2] M.T. Robinson, J. Nucl. Mater. **216** (1994) 1

[3] W. Schilling and H. Ullmaier, in: Nuclear Materials, Vol. 10 B of Materials Science and Technology (B.R.T. Frost,ed.), Verlag Chemie VCH, Weinheim(1993)

[4] G.E. Lucas, J. Nucl. Mater. **216** (1994) 322

[5] L.K. Mansur, J. Nucl. Mater. **216** (1994) 97

[6] H. Ullmaier, Trans. Ind. Soc. Metals, **34** (1981) 324

[7] L.W. Hobbs, F.W. Clinard,Jr., S.J. Zinkle and R.C. Ewing, J. Nucl. Mater. **216** (1994) 291

[8] TRIM89, see: J.P. Biersack and L.G. Haggmark, Nucl. Instr. and Meth. **174** (1980) 93

[9] M.H. Norget, M.T. Robinson and I. Torrens, Nucl. Eng. Design. **33** (1975) 50

[10] R.S. Averback, R. Benedek and K.L. Merkle, Phys. Rev. **B 18** (1978) 4156

[11] J.H. Kinney, M.W. Guinan and Z.A. Munir, J. Nucl. Mater. **122/123** (1984) 1028

[12] A.J.E. Foreman, W.J. Phythian and C.A. English, Phil. Mag. **A 66** (1992) 671

[13] T. Diaz de la Rubia and M.W. Guinan, UCRL–JC–107488

[14] ITER Joint central team, J. Nucl. Mater. **212-215** (1994) 3

[15] Z. Zhu, K. Chen, J. Chen, R. Xu and Z. Wang, Nucl. Instr. and Meth. **B 61** (1991) 72

[16] P. Jung, in: Atomic defects in metals (collection of all relevant defect data), in Landolt-Börnstein, vol. III/25, (Springer, Berlin 1991), H. Ullmaier, Ed., p.1

[17] T. Shikama and G.P. Pells, Phil. Mag. **A47** (1983) 369

[18] G.P. Pells and T. Shikama, Phil. Mag. **A48** (1983) 779

[19] R.S. Wilks, J. Nucl. Mater. **26** (1968) 137

[20] D.G. Howitt and T.E. Mitchell, Phi. Mag. **A44** (1981) 229

[21] A.Y. Stathopoulos and G.P. Pells, Phi. Mag. **A47** (1983) 381

[22] W.E. Lee, G.P. Pells and M.L. Jenkins, J. Nucl. Mater. **122-123** (1984) 1393

[23] Y. Katano, H. Ohno and H. Katsuta, J. Nucl. Mater. **155-157** (1988) 366

[24] A. Kohyama, K. Asano, Y. Katoh and Y. Kohno, Proc. 15th Int. Symp. on Effects of Radiation on Materials, ASTM-STP 1125(ASTM, Philadelphia, 1992), p.1051

[25] Y. Satoh, C. Kinoshita and K. Nakai, J. Nucl. Mater. **179-181** (1991) 399

[26] R. Nakai, C. Kinoshita, Y. Muroo and S. Kitajama, Phil. Mag. **A48** (1984) 215

[27] G.P. Pells, J. Nucl. Mater. **122-123** (1984) 1338

[28] B.S. Hickman and D.G Walker, J. Nucl. Mater. **18** (1966) 197

[29] J.L. Routbort and A.A. Solomon, Irradiation Effects in Creep of Oxide Fuels, in Reactor Development Program Progress Report, USAEC Report ANL-7758, p-78, Argonne National Lab.,1970

[30] M.L. Grossbeck and L.K. Mansur, J. Nucl. Mater. **179-181** (1991) 130

[31] K. Dettmann, G. Leibfried and K. Schroeder, Phys. Status Solidi **22** (1967) 423, 433

[32] J.L. Brimhall, E.P. Simonen and H.E. Kissinger, J. Nucl. Mater. **48** (1973) 339

[33] V.A. Borodin, A.I. Ryazanov and D.G. Sherstennikov, J. Nucl. Mater. **202** (1993) 169

[34] E.R. Gilbert, React. Tech. **14** (1971) 258

[35] R. Bullough and M.H. Wood, J. Nucl. Mater. **90** (1980) 1

[36] F.A. Nichols, J. Nucl. Mater. **90** (1980) 29

[37] L.K. Mansur and T.C. Reiley, J. Nucl. Mater. **90** (1980) 60

[38] E.R. Gilbert, J. Nucl. Mater. **90** (1980) 68

[39] C.M. Nelson and J.H. Crawford,Jr. J. Phys. Chem. Solids **13** (1960) 296

[40] P.W. Levy, J. Phys. Chem. Solids **13** (1960) 287

[41] G.N. Greaves, Phil. Mag. **B37** (1978) 447

[42] E.W.J Mitchell and C.M. Nelson, Phil. Mag. **1** (1956) 1085

[43] D.L. Griscom, Mat. Res. Soc. Symp. Proc. vol.61, 1986, p.213

[44] R.A. Weeks and C.M. Nelson, J. Am. Ceram. Soc., **43** (1960) 396

[45] M. Antonini, P. Camagni, P.N. Gibson and A. Manara, Rad. Eff. **65** (1982) 41,49

[46] E. Lell, N.J. Kreidl and J.R. Hensler, in: Prog. in Ceram. Sci. Vol.4, 1966, J.E. Burke ed., p.1

[47] E.J. Friebele, P.L. Higby and T.E. Tsai, Diffusion and Defect Data **53-54** (1987) 203

[48] M. Guzzi, M. Martini, A. Paleari, F.Pio, A. Vedda and C. B. Azzoni, J. Phys.: Condens. Matter, **5** (1993) 8105

[49] W. Primak, L.H. Fuchs and P. Day, J. Am. Ceram. Soc., **38** (1955) 135

[50] W. Primak and E. Edwards, Phys. Rew. **128** (1962) 2580

[51] W. Primak and R. Kampwirth, J. Appl. Phys. **39** (1968) 5651

[52] E.P. EerNisse, J. Appl. Phys. **45** (1974) 167

[53] W. Primak, Phys. Rew. **110** (1958) 1240

[54] M. Wittels and F.A. Sherrill, Phys. Rew. **93** (1954) 1117

[55] I.K. Abdukadyrova and A.A. Fotchenkov, Sov. At. Energy **52** (1982) 183

[56] G.W. Arnold, Rad. Eff. **98** (1986) 55

[57] T. Tanaka, T. Eshita, T. Tanimura and N. Itoh, Cryst. Latt. Def. and Amorphous Mat. **11** (1985) 221

[58] S. Klaumünzer, C. Li, S. Loffler, M. Rammensee, G. Schumacher, Nucl. Instr. and Meth. **B39** (1989) 665

[59] W. Primak, J. Appl. Phys. **35** (1964) 1342

[60] T. Jensen, B.R. Lawn, R.L. Dalglish and J.C. Kelly, Rad. Eff. **28** (1976) 245

[61] I. Biron and A. Barbu, Appl. Phys. Lett. **48** (1986) 1645

[62] G. Mayer and M. Leconte, J. Phys. Radium. **21** (1960) 846

[63] I.V. Maxim and D. Apostol, J. Nucl. Mater. **42** (1972) 49

[64] C.H.de Novion and A. Barbu, Solid State Phenom. **30-31** (1993) 277

[65] Z. Zhu and P. Jung, Miniaturized specimens for testing of irradiated materials, P. Jung, H. Ullmaier eds., Jülich, 1995, p. 212

[66] P. Jung, A. Schwarz and H.K. Sahu, Nucl. Instr. and Meth. **A 234** (1985) 331

[67] C.E. Klabunde and R.R. Coltman, J. Nucl. Mater. **108-109** (1982) 183

[68] Z. Zhu and P. Jung, J. Nucl. Mater. **212-215** (1994) 1081

[69] Z. Zhu and P. Jung, Nucl. Instr. and Meth. **B 91** (1994) 269

[70] Z. Zhu and P. Jung, Rad. Eff., tbp

[71] J.P. Poirier, Creep of Crystals (Cambridge University Press, 1985) p.100

[72] R. Brückner, J. Non-cryst. Solids **5** (1970) 177

[73] L.K. Keys, J.P. Smith and J. Moteff, Phys. Rev. **176** (1968) 851

[74] A.N. Ivanov, L.A. Elesin and N.F. Plavjuk, IAEA-SM-120/C-6, p.289

[75] W. Primak, Phys. Rev., **103** (1956) 1681

[76] H. Trinkaus, J. Nucl. Mater., **223** (1995) 196

[77] D.G. Martin, J. Phys. Chem. Soc. **10** (1958) 64

[78] J.J. Antal and A.N. Goland, Phys. Rew. **112** (1958) 105

[79] B.S. Hickman and D.G. Walker, Proc. Brit. Ceram. Soc., **7** (1967) 381

[80] R.S. Wilks, J.A. Desport and R. Bradley, Proc. Brit. Ceram. Soc., **7** (1967) 403

[81] M. Stevanovic and J. Elston, Proc. Brit. Ceram. Soc., **7** (1967) 423

[82] R.P. Thorne and V.C. Howard, Proc. Brit. Ceram. Soc., **7** (1967) 439

[83] F.W. Clinard, J.M. Bunch and W.A. Ranken, in: Rad. Eff. and Trium Technology for Fusion Reactors, USERDA CONF-750989, vol. II(1976) p.498

[84] R. Yamada, S.J. Zinkle and G.P. Pells, J. Nucl. Mater. **209** (1994) 191

[85] F.W. Clinard, G.F. Hurley and L.W. Hobbs, J. Nucl. Mater. **108/109** (1982) 655

[86] H.-E. Schaefer and M. Forster, Mater. Sci. Eng. **A109** (1989) 161

[87] K. Atobe, N. Nishimoto and M. Nakagawa, Phys. Status Solidi **A89** (1985) 155

[88] W. Dienst, J. Nucl. Mater. **211** (1994) 186

[89] R.P. Thorne, V.C. Howard and B. Hope, Proc. Brit. Ceram. Soc., **7** (1967) 449

[90] R.J. Price, J. Nucl. Mater. **33** (1969) 17

[91] R. Blackstone and E.H. Voice, J. Nucl. Mater. **39** (1971) 319

[92] R.A. Matheny, J.C. Corelli and G.G. Trantina, J. Nucl. Mater. **83** (1979) 313

[93] R.J. Price, J. Nucl. Mater. **48** (1973) 47

[94] K. Hojou and K. Izui, J. Nucl. Mater. **133/134** (1985) 709

[95] K. Nakata, S. Kasahara, S. Shimanuki, Y. Katano, H. Ohno and J. Kuniya, J. Nucl. Mater. **179-181** (1991) 403

[96] H. Huang and N. Ghoniem, J. Nucl. Mater. **212-215** (1994) 148

[97] C.W. White, C.J. Mchargue, P.S. Sklad and L.A. Boatner, Mater. Sci. Rep. **4** (1989) 41

[98] J. Wong, T. Diaz de la Rubia, M.W. Guinan, M. Tobin, J. Nucl. Mater. **212-215** (1994) 143

[99] W. Dienst, J. Nucl. Mater. **191-194** (1992) 555

[100] T. Yano, M. Tezuka, H. Miyazaki and T. Iseki, J. Nucl. Mater. **1991-1994** (1992) 635

[101] M. Billy, J.-C. Labbe, Y.-M. Lee and G. Roult, Rev. Int. Haut. Temper. Rerract. Fr. **21** (1984) 19

[102] T. Yano and T. Iseki, J. Nucl. Mater. **179-181** (1991) 387

[103] B. Hendernson and D.H. Bowen, J. Phys. C: Sol. State Phys. **4** (1971) 1487

[104] B.S. Hickman and D.G. Walker, Phil. Mag. **11** (1965) 1101

[105] J.A. Desport and J.A.G. Smith, J. Nucl. Mater. **14** (1964) 135

[106] G.W. Groves and A. Kelly, Phil. Mag. **8** (1963) 1437

[107] S.J. Zinkle, J. Am. Ceram. Soc., **72** (1989) 1343

[108] F.W. Clinard, Jr. Cry. Latt. Def. and Amorph. Mater. **14** (1987) 241

[109] C. Kinoshita, J. Nucl. Mater. **191-194** (1992) 67

[110] G.P.Pells and M.J. Murphy, J. Nucl. Mater. **183** (1991) 137

[111] P. Jung, J. Nucl. Mater. **113** (1983) 133

[112] F. Pászti, Mater. Sci. Eng. **A115** (1989) 57

[113] L.E. Halliburton, Cry. Latt. Def. and Amorph. Mater. **12** (1985) 163

[114] F.L. Galeener, Diff. and Defect data **53-54** (1987) 305

[115] R.A.B. Devine, Nucl. Instr. and Meth. **B 91** (1994) 378

[116] W.H. Zachariasen, J. Am. Ceram. Soc., **54** (1932) 3841

[117] N. Lebedev, Proc. State opt. Inst. Leningr. **2** (1921) 10

[118] H. Fischer, G. Gotz and H. Karge, Phys. Stat. Solidi.(a) **76** (1983) 249

[119] G. Das and T.E. Mitchell, Rad. Eff. **23** (1974) 49

[120] R.G. Macaulay-Newcombe and D.A. Thompson, Nucl. Instr. and Meth. **B 1** (1984) 176

[121] E.R Hodgson, Crys. Latt. Def. Amorph. Mater. **18** (1989) 169

[122] G.P. Pells, J. Nucl. Mater. **184** (1991) 177

[123] T. Shikama, M. Narui, Y. Endo, T. Sagawa and H. Kayano, J. Nucl. Mater. **191-194** (1992) 575

[124] P. Jung, Z. Zhu and H. Klein, J. Nucl. Mater. **206** (1993) 72

[125] F. Scheuermann and W. Kesternich, Proceedings of the 4th International Conference on Electroceramics and applications, R. Waser et al eds., Aachen, 1994, Vol. II, p. 1119

List of Tables

Abbildungsverzeichnis

Tabellenverzeichnis

List of Symbols

a	lattice parameter
b	Burger's vector
c	velocity of light
C'	specific heat
C	defect concentration
C_i	interstitial concentration
C_v	vacancy concentration
C_{v0}	thermal vacancy concentration
C_v^{∞}	saturation vacancy concentration
C_{iL}	concentration of interstitials trapped in loops
C_{vL}	concentration of vacancies trapped in loops
C_{iC}	concentration of interstitials trapped in clusters
C_{vC}	concentration of vacancies trapped in clusters
C_{iD}	concentration of interstitials trapped by dislocations
C_{vD}	concentration of vacancies trapped by dislocations
C_L	concentration of interstitial loops
C_0	standard capacitance
C_s	specimen capacitance
D_{i0}	prefactor of interstitial diffusion coefficient
D_{v0}	prefactor of vacancy diffusion coefficient
D_i	interstitial diffusivity
D_v	vacancy diffusivity
e_i	dilatation of free interstitials
e_v	dilatation of free vacancies
e_{iL}	dilatation of interstitials trapped in loops
e_{vL}	dilatation of vacancies trapped in loops
e_{iC}	dilatation of interstitials trapped in clusters
e_{vC}	dilatation of vacancies trapped in clusters
e_{iD}	dilatation of interstitials trapped by dislocations
e_{vD}	dilatation of vacancies trapped by dislocations
dE'/dx	stopping power consumed in thermal spikes
ΔE	total energy deposition inside specimens
E	energy of irradiating particle
E_p	energy of irradiation protons

E_{max}	maximum energy of the irradiation particles
E_{min}	minimum energy of the irradiation particles
E_i^m	migration energy of interstitials
E_v^m	migration energy of vacancies
E_b	atomic energy level of atoms with broken bonds
E_{g1}	atomic energy level of atoms in g1-type glass states
E_{g2}	atomic energy level of atoms in g2-type glass states
ΔE_{g1}	$= E_b - E_{g1}$
ΔE_{g2}	$= E_b - E_{g2}$
I	electrical current
$I_0(\lambda)$	incident light intensity
$I_t(\lambda)$	transmitting light intensity
$I_s(\lambda)$	transmitting light intensity of the irradiated specimens
$I_b(\lambda)$	transmitting light intensity of the unirradiated specimens
k_B	Boltzmann constant
K	displacement rate, defect production rate
K_{g1}	irradiation induced transition rate of atoms between g1-type glass state and breaking state
K_{g2}	irradiation induced transition rate of atoms between g2-type glass state and breaking state
M	mass of target atoms
m	mass of irradiation particle
m_e	electron mass
N	total number of target atoms
N_b	number of atoms located in breaking state
N_{g1}	number of atoms located in g1-type glass state
N_{g2}	number of atoms located in g2-type glass state
N_t	saturation number of atoms located in g2-type glass state
$N_d(T)$	calculated number of "displacements"
P_0	a constant
q_0	a numerical factor
q	the recombination coefficient
Q	energy going into electronic losses
Q_0	a constant

R_a	specimen surface resistance
R_b	specimen surface resistance
R_s	specimen bulk resistance
R_m	apparent resistance
R	resistance of lead to guard ring
R_L	interstitial loop radius
R_L^{max}	maximum interstitial loop radius
S_t	total volume change
T	recoil energy
T_{irr}	irradiation temperature
t	time
T_{dam}	damage energy
$T_{1/2}$	median recoil energy where $W(T_{1/2}) = 0.5$
T_d	threshold energy for displacement
$T_{d,min}$	minimum threshold energy for displacement
T_m	melting temperature
T_{max}	maximum transferable recoil energy
T^*	material flow temperature
Δt	time increase step
U	driving potential
V_{sp}	size of thermal spikes
v_s	spontaneous recombination volume
v_a	critical recombination volume for amorphization
V_F	volume dilatation of a Frenkel pair
V_F'	volume dilatation of a free vacancy and an interstitial trapped in loops
V_1, V_2	driving voltages
$\frac{\Delta V}{V}$	relative volume change
$(\frac{\Delta V}{V})_\infty$	saturation volume change
$W(T')$	fraction of damage energy with recoil events $T' < T$
x	specimen thickness
x_s	irradiated specimen thickness
x_b	unirradiated specimen thickness
Z_i	dislocation bias factor for interstitial
Z_v	dislocation bias factor for vacancy

α	absorption coefficient
α_{irr}	radiation induced absorption coefficient
β	efficiency of energy deposition through breaking of bonds
η	apparent viscosity
λ	wavelength
λ'	decay constant
μ	shear modulus
ν	Posson's ratio
ν_{g1}, ν_{g2}	atom vibrating frequences
Ω	atomic volume
Ω_{g1}	atomic volumes of glassy materials
ϕ	flux of irradiation particles
$d\Phi(E)$	flux of irradiating particles with energies between E and E+dE
ψ	the O–Si–O angle in SiO_2
θ	the Si–O–Si angle in SiO_2
ξ^0	damage efficiency
$d\sigma(T,E)$	differential cross section
σ	mechanical stress
σ_d	displacement cross section
$\Sigma_c, \varepsilon_c^{sat}$	saturation compaction strain
ρ	mass density
ρ_d	dislocation line density
ρ_l	interstitial loop line density
ρ_F	resistivity contribution per unit concentration of vacancies(point defects) and interstitials(trapped in loops or in dislocations)
$\Delta\rho$	radiation induced resistivity change
$\dot{\epsilon}$	deformation rate
ε_c	compaction strain
$\frac{d\varepsilon}{dt}$	creep rate

Danksagung

Diese Arbeit wurde in der Sondergruppe "'Mechanische Werkstoffeigenschaften"' des Instituts für Festkörperforschung des Forschungszentrums Jülich durchgeführt.

Herrn Prof. Dr. H. Ullmaier danke ich für die Möglichkeit zur Durchführung dieser Arbeit in seiner Gruppe sowie für sein förderndes Interesse und wertvolle Diskussionen.

Mein besonderer Dank gilt meinem Betreuer, Herrn Dr. P. Jung, für die Anregung zu dieser Arbeit, die Unterstützung bei der Durchführung der Experimente und für viele hilfreiche und klärende Diskussionen.

Herrn Dr. H. Trinkaus danke ich für die wertvollen theoretischen Diskussionen.

Herrn H. Klein danke ich für die Arbeiten am TEM sowie für die Hilfe bei der Durchführung der Experimente. Herrn W. Schmitz danke ich für die Arbeiten am REM.

Herrn Dr. V. Zell, Herrn Dipl.-Phys. R. Merkes und Herrn Dr. F. Carsughi danke ich für ihre technische Hilfe beim Schreiben dieser Arbeit.

Den anderen Mitgliedern der Gruppe, Dr. W. Kesternich, Herrn J. Deutz, Herrn Dipl.-Phys. F. Scheuermann, Frau Dipl.-Ing. S. Hirsch sowie Frau M. Garcia bin ich für ihre freundliche Hilfsbereitschaft zu Dank verpflichtet.

Bei der Bedienungsmannschaft des Zyklotrons bedanke ich mich für die Hilfsbereitschaft und die gute Zusammenarbeit.

Für die optischen Absorptionsmessungen im INC bedanke ich mich bei Herrn Dr. E. Langenscheidt für seine Hilfsbereitschaft.

Bedanken möchte ich mich noch bei Herrn F. Römer, Frau Ro. Fischer, Herrn H. Scheiba, Herrn Bischof und Herrn H. J. Bierfeld für die Probenpräparation und -analyse.

Meiner Mutter Xiuying Zhu danke ich für Ihr Verständnis und Ihre Unterstützung.

Zhiyong Zhu

Jül-3109
September 1995
ISSN 0944-2952